Orphan source detection in mobile gamma-ray spectrometry - Improved techniques for background assessment

Kock, Peder

2012

Orphan source detection in mobile gamma-ray spectrometry

Improved techniques for background assessment

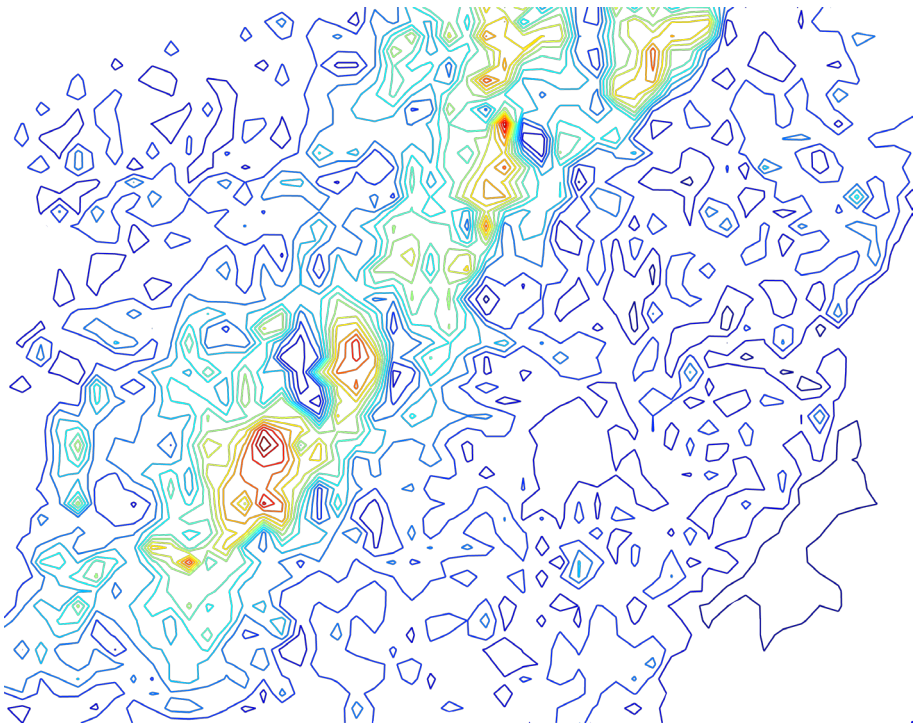

Peder Kock

Department of Medical Radiation Physics
Lund University, Sweden

Orphan source detection in mobile gamma-ray spectrometry

Improved techniques for background assessment

Peder Kock

LUND UNIVERSITY

Doctoral Thesis
2012

Department of Medical Radiation Physics
Lund University, Sweden

ISBN 978-91-7473-385-3

The public defense of this thesis for the degree Doctor of Philosophy in Physics will, with due permission from the Faculty of Science at Lund University, take place in Room 2005-2007, Inga Marie Nilssons gata 49, Skåne University Hospital, Malmö, on Friday, 12 October 2012, at 09.00.

Cover:
Thorium radiation levels measured by airborne gamma-ray spectrometry.

peder.kock@gmail.com

Department of Medical Radiation Physics
Faculty of Science
Lund University
SUS Malmö
SE-205 02 Malmö, Sweden

ISBN 978-91-7473-385-3
Typeset using LaTeX and the template lumedthesis.cls ver 1.2,
available through erik.hedstrom@gmail.com
Printed by: Media-Tryck, Lund

It's a heavy metal universe
—Kai Hansen, Gamma Ray

Contents

List of publications

This thesis is based on the following publications, which will be referred to in the text by their Roman numerals:

I. Kock, P., Finck, R.R., Nilsson, J.M.C., Östlund, K. and Samuelsson, C. (2010), A deviation display method for visualising data in mobile gamma-ray spectrometry. *Appl. Radiat. Isotopes*, 68(9); pp. 1832–1838

II. Kock, P., Lanke, J. and Samuelsson, C. (2012), A real-time statistical alarm method for mobile gamma spectrometry – Combining counts of pulses with spectral distribution of pulses. *Nucl. Instrum. Meth. A*, 681; pp. 55–60

III. Kock, P. and Samuelsson, C. (2011), Comparison of airborne and terrestrial gamma spectrometry measurements – evaluation of three areas in southern Sweden. *J. Environ. Radioactiv.*, 102(6); pp. 605–613

IV. Kock, P., Rääf, C.L. and Samuelsson, C. On background radiation gradients – The use of airborne surveys when searching for orphan sources using mobile gamma-ray spectrometry. *Manuscript*

V. Kock, P. (2010), Investigating microphonic noise in mobile gamma-spectrometric HPGe measurements using accelerometers. In: *Proceedings of Third European IRPA Congress, Helsinki, Finland.*; pp. 1681-1690.

Abstract

Hazardous radioactive sources out of regulatory control are referred to as orphan sources. Focussing on gamma-emitting orphan sources, this thesis describes methods that can be used in mobile gamma-ray spectrometry to perform real-time discrimination between an actual source signal and the signal due to the natural radiation background.

Two categories of methods for orphan source detection are presented: visualisation and statistical hypothesis testing. Visualisation leaves the interpretation to the operator, whereas the hypothesis testing aims at answering the question: is there a signal or not? The methods are shown to work well for purely stochastic background data. The visualisation method gives a homogeneous representation of large data sets, which enhances the capability to discern significant positive deviations. The hypothesis testing method is shown to exhibit false alarms at the expected rate. Furthermore, by taking into account the spectral distribution in a hypothesis test, the power of the test was increased when compared with reference methods from the literature.

Systematic background radiation variations can be disclosed by using data from airborne gamma-ray spectrometry (AGS) surveys. Validation of AGS data at the ground level by the use of terrestrial surveys yielded a strong positive correlation between the two data sets for background activity of uranium and thorium. By deriving a step function from AGS data, the systematic background variations were successfully modelled at the ground level. This approach was shown to reduce the number of excess false positives in an area with strong background gradients.

In addition to random and systematic background radiation fluctuations, germanium spectrometers can have problems with microphonic noise due to the vibrations that inevitably will occur in mobile gamma-ray spectrometry. The additional noise can be expected to degrade the resolution of the detector. The level of resolution degradation was found to be 0-19 %, depending on the speed of the vehicle.

Summary in Swedish

Bortglömda, stulna eller på andra sätt borttappade radioaktiva strålkällor som kan anses vara farliga för allmänheten kallas herrelösa strålkällor. Denna avhandling handlar om metoder för att hitta herrelösa strålkällor som emitterar s.k. γ-strålning (gammastrålning), bestående av ljuspartiklar med mycket hög energi. γ-strålning har god förmåga att penetrera materia och kan därför i många fall detekteras på långa avstånd. Genom att använda stora detektorer med hög densitet ökar sannolikheten för att γ-partiklarna absorberas i detektorn; detta ger ett sorts fingeravtryck (puls) med vilket det radioaktiva grundämnet kan identifieras.

Det stora problemet vid sökning av herrelösa strålkällor är den naturliga bakgrundsstrålningen som främst härrör från radioaktiva grundämnen i berggrunden och jorden. Denna γ-strålning interfererar med γ-strålningen från strålkällan, vilket gör att statistiska metoder måste användas för att avgöra huruvida de detekterade pulserna är inom slumpmarginalen. Genom att med färgkodning visualisera pulserna från γ-strålningen över en tid längs en färdväg kan bedömningen underlättas. Den i arbetet framtagna visualiseringsmetoden undertrycker bakgrundsbruset så att signaler som höjer sig däröver framhävs, vilket underlättar sökandet. Vidare presenteras ett statistiskt test som bygger på s.k. hypotesprövning. Genom att ta hänsyn till såväl partiklarnas energi som antal visar vi att detta test är mer känsligt än jämförbara test.

Jämförelser mellan mark- och flymätningar visar att data från flygmätningar kan användas på marknivån för att lokalisera kraftiga förändringar i bakgrundsstrålningen. Utifrån detta samband används sedan flygdata för att reducera antalet falska indikationer på marknivån för ett område med kraftiga variationer i γ-strålningen.

Slutligen visas att brus orsakat av mekaniska vibrationer kan vara ett problem då germaniumdetektorer används utanför laboratoriemiljön. Bruset påverkar systemets upplösningsförmåga negativt, vilket kan försämra identifieringsegenskaperna hos systemet.

Abbreviations

Technical terms

ACF	Autocorrelation function
AGS	Airborne Gamma Spectrometry
CGS	Car-borne Gamma Spectrometry
eU	Equivalent Uranium
eTh	Equivalent Thorium
FEPE	Full Energy Peak Efficiency
FET	Field-Effect Transistor
FFT	Fast Fourier Transform
FOV	Field of View
FWHM	Full Width at Half Maximum
HPGe	High-Purity Germanium
$LaBr_3$:Ce	Lanthanum Bromide doped with Cerium
MA	Moving Average
MA^w	Weighted Moving Average
ML	Maximum Likelihood
MLE	Maximum Likelihood Estimator
NaI(Tl)	Sodium Iodide doped with Thallium
NORM	Naturally Occurring Radioactive Materials
S&D	Sumerling & Darby

Organisations

IAEA	International Atomic Energy Agency
ICRU	International Commission on Radiation Units & Measurements
SGU	Geological Survey of Sweden
SSM	Swedish Radiation Safety Authority
UNSCEAR	United Nations Scientific Committee of the Effects of Atomic Radiation

List of symbols

Primary fluence formalism

ϕ_p	Primary photon fluence rate	$\mathrm{m}^{-2}\ \mathrm{s}^{-1}$
A	Activity per unit volume	$\mathrm{Bq}\ \mathrm{m}^{-3}$
μ_x	Linear attenuation coefficient in medium x	m^{-1}
n_γ	Photon emission probability	
$\mathrm{E_n}$	Exponential integral of nth order	
ϕ_f	Primary fluence fraction	

Statistical inference

H_0	Null hypothesis
H_1	Research hypothesis
α	Level of significance or false positive rate
α'	Actual false positive rate
β	False negative rate
μ	Poisson mean of sample
λ	Poisson mean of background
q	Sample to total Poisson ratio
x	Sample counts
y	Background counts
z	Total counts
$\mathcal{L}$	Likelihood function
Λ	Likelihood ratio

Chapter 1

Introduction

1.1 Background

The International Atomic Energy Agency (IAEA) reports on radiological accidents where radioactive sources used in radiotherapy, industrial radiography, medical applications or at industrial irradiation facilities have been improperly handled, lost or stolen (IAEA, 1993, 1996, 1998, 2000a,b, 2002a,b, 2004). These lost sources are referred to as "orphan sources", defined by the IAEA (2003) as:

> "A source which poses sufficient radiological hazard to warrant regulatory control, but is not under regulatory control because it has never been so, or because it has been abandoned, lost, misplaced, stolen or otherwise transferred without proper authorization."

Thus, if the location of the source is unknown, and it poses a sufficient radiological hazard, a search operation using portable gamma spectrometry instruments may be launched. The techniques used can vary, but in general mobile gamma spectrometry measurements are conducted using repeated short-term measurements with meters, maps, graphs or displays aiding the search crew in locating the radioactive source. Large areas are preferably searched using airborne gamma spectrometry (AGS), whereas car-borne gamma spectrometry (CGS) or searches using portable equipment (backpack) can be alternatives when spatial resolution is a priority.

Hjerpe (2004) and the IAEA (2003) list examples of potential orphan sources originating from medical and industrial applications; they

include:

- **Teletherapy**, mainly ^{60}Co or ^{137}Cs sources used for external radiation treatment. Activity range is typically in the order of tens to hundreds of TBq.
- **Irradiators**, mainly ^{60}Co or ^{137}Cs sources used in medical blood irradiation equipment or at industrial sterilisation facilities. Activity typically ranges from tens of TBq (medical) to hundreds of PBq (sterilisation).
- **Radioiodine**, mainly unsealed solutions of ^{131}I and to some lesser extent ^{125}I and ^{123}I, used in nuclear medicine. Activity is typically up to a few GBq.
- **Generators**, mainly ^{99}Mo $\rightarrow$ ^{99m}Tc, the latter is used in nuclear medicine for imaging. Activity ranges from a few to 100 GBq.
- **Radiography**, mainly ^{192}Ir, ^{60}Co or ^{75}Se sources used in industry to examine welded joints or by customs services to scan cargo. Activity is typically a few TBq.
- **Thermoelectric generators**, radioisotope thermoelectric generators typically containing a few PBq of ^{90}Sr (navigation beacons) or ^{238}Pu (spacecrafts).
- **Industrial devices**, e.g. smoke detectors, gauges and well logging devices containing a few to hundreds of GBq of ^{241}Am, ^{137}Cs and ^{241}Am/Be respectively.

Although the context of this thesis is orphan source detection using CGS, the reversed scenario, where the source is moving past a stationary detector, is also a situation where many of the methods described in this work can be applied. Such scenarios can be found in radioactive monitoring of e.g.: scrap metals (Campi and Porta, 2005; Takoudis et al., 2010); border crossings (Duftschmid, 2002; Geelhood et al., 2004; Pujol et al., 2011) and major public events (Quayle et al., 2010).

Exercises have been arranged in Europe, on the international as well as national level, focussing on: the first response and the aftermath of a nuclear or radiological accident (Finck et al., 2008); malevolent use of radioactive material (Östlund et al., 2010); orphan source detection (Dowdall et al., 2012; Finck and Ulvsand, 2003; Ulvsand et al., 2002); the analysis of gamma spectra (Dowdall et al., 2010a,b) and ground to air

comparisons (Hovgaard et al., 1997; Sanderson et al., 2003). The accident reports published by the IAEA and the lessons learned from the Chernobyl accident have been important inputs for the scenarios of the exercises.

The radiological and nuclear emergency preparedness in Sweden, maintained and coordinated by the Swedish Radiation Safety Authority (SSM), has long been dominated by the threat from nuclear accidents, foreign or domestic. However, in Sweden as well as in other countries, the awareness of potentially malevolent use of radiological or nuclear materials has increased post 9/11. Different scenarios, including the orphan source, the radiological dispersal device or simply 'dirty bomb', nuclear fallout and transport accidents involving radioactive material have been discussed and exercised within the national emergency preparedness in Sweden since 2001, cf. Fig. 1.1 (Finck et al., 2008).

Figure 1.1: Radiological dispersal device scenario in the DEMOEX exercise 2006. A radiological response team (left) approaches the 'hot zone' around the bus wreck (right). *Image courtesy of Robert Finck, SSM.*

This thesis is the result of one of the research projects funded by the SSM to build and uphold the radiological emergency preparedness in Sweden. The orphan source scenario described above has been the research context of Papers I, II and IV, where different approaches to the problem of separating an actual signal from the background noise are studied. Paper III focusses on the potential use of airborne data as background estimate at the ground level whereas Paper V investigates the problem of microphonic noise when using High-Purity Germanium (HPGe) spectrometers in mobile gamma-ray spectrometry.

1.2 Aims of this work

The general aim of this work was to develop, evaluate and improve methods to account for the natural background gamma radiation when searching for orphan sources using mobile gamma-ray spectrometry.

The specific aims were to:

- develop and implement improved methods for real-time spectrometry data evaluation by searching for statistically significant deviations, either through visualisation (Paper I) or statistical hypothesis testing (Paper II)
- increase our understanding of the correlation between airborne and terrestrial natural background radiation data (Paper III) and to investigate the applicability of airborne data in reducing both false positives and false negatives in a strongly varying background radiation environment (Paper IV)
- investigate the impact of vechicle speed and detector mounting configuration as regards the occurrance of microphonic noise in a mobile high-resolution spectrometry system (Paper V)

Chapter 2

Theoretical background

2.1 Primary fluence formalism

Uniform model

The primary photon fluence rate at a point, D, h metres above ground from a uniform volume source, V, in the ground (cf. Fig. 2.1) is

$$\phi_p = A \cdot n_\gamma \iiint_V \frac{1}{4\pi r^2} \exp(-\mu_s(r - h\sec\theta) - \mu_a h \sec\theta)\,\mathrm{d}V \qquad (2.1)$$

where μ_s, μ_a are the linear attenuation coefficients in soil and air respectively, n_γ the γ-emission probability and A the activity per unit volume (ICRU, 1994). In spherical coordinates the volume element is:

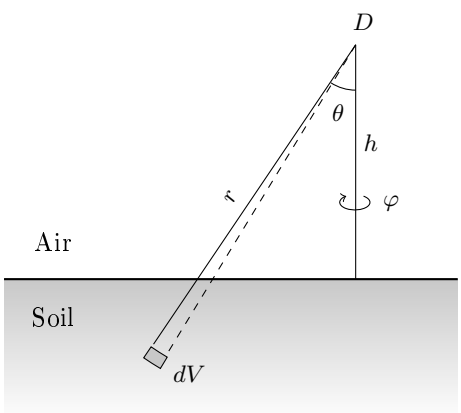

Figure 2.1: Geometry of *in-situ* primary photon fluence rate derivation. A primary photon originating from dV, and detected at D, must pass through the soil and air media along r. As $\theta \to \pi/2$ and thus $r \to +\infty$, the probability of the photon arriving at D becomes infinitely small. Rotational symmetry is assumed so that the primary fluence at D is independent of φ.

$$\mathrm{d}V = r^2 \sin\theta \,\mathrm{d}r \,\mathrm{d}\theta \,\mathrm{d}\varphi \tag{2.2}$$

Covering the whole soil half space, the limits of integration defining V in Eq. 2.1 then become:

$$\begin{aligned} h\sec\theta \leq r &\leq \infty \\ 0 \leq \theta &\leq \frac{\pi}{2} \\ 0 \leq \varphi &\leq 2\pi \end{aligned}$$

Integration over the azimuthal angle φ contributes with a factor 2π, owing to rotational symmetry; thus

$$\phi_p = \frac{A \cdot n_\gamma}{2} \int_{h\sec\theta}^{\infty} \int_{0}^{\pi/2} \sin\theta \exp(-\mu_s(r - h\sec\theta) - \mu_a h \sec\theta) \,\mathrm{d}r \,\mathrm{d}\theta \tag{2.3}$$

while integrating with respect to the radius, r, gives

$$\int_{h\sec\theta}^{\infty} \exp(-\mu_s(r - h\sec\theta)) \,\mathrm{d}r \;\; = (-\frac{1}{\mu_s})[0 - 1] = \frac{1}{\mu_s} \tag{2.4}$$

Using the substitution $t = \mu_a h \sec\theta$, the polar angle integral is

$$\begin{aligned} \phi_p &= \frac{A \cdot n_\gamma}{2\mu_s} \int_0^{\pi/2} \sin\theta \exp(-\mu_a h \sec\theta) \,\mathrm{d}\theta \\ &= \frac{A \cdot n_\gamma}{2\mu_s} \mu_a h \int_{\mu_a h}^{\infty} t^{-2} \exp(-t) \,\mathrm{d}t \\ &= \frac{A \cdot n_\gamma}{2\mu_s} \mathrm{E}_2(\mu_a h) \end{aligned} \tag{2.5}$$

where E_2 is the exponential integral of second order, defined as

$$\mathrm{E}_\mathrm{n}(x) = x^{n-1} \int_x^{\infty} t^{-n} \exp(-t) \,\mathrm{d}t \tag{2.6}$$

This generalised form can be written as a special case of the unnormalized incomplete gamma function (Abramowitz and Stegun, 1972)

$$\mathrm{E}_\mathrm{n}(x) = x^{n-1} \,\Gamma(1 - n, x) \tag{2.7}$$

which can be calculated numerically, cf. e.g. GSL (2011). The assumptions required to derive the analytical solution given in Eq. 2.5 are: (i) an

uniform activity distribution, A; (ii) a homogeneous soil content (moisture, density etc.) and (iii) a flat soil surface. The unit of the primary photon fluence rate given in Eq. 2.5 is $\mathrm{m}^{-2}\ \mathrm{s}^{-1}$.

In *in-situ* measurements the natural radionuclides are often assumed to be uniformly distributed in the ground (Beck et al., 1972; ICRU, 1994, 2006), and measurements of soil cores have confirmed this assumption for the top 20 cm of the ground (Finck, 1992). Working under the assumption of homogeneity, Eq. 2.5 is a convenient and reasonable solution when the primary photon fluence rate from natural radionuclides in the ground is of interest.

Other models

The primary photon fluence rate at D from an infinite disc on the soil surface, i.e. restricting the radius of Eq. 2.1 to $r = h \sec\theta$, can be shown to be

$$\phi_p = \frac{A \cdot n_\gamma}{2} \mathrm{E}_1(\mu_a h) \tag{2.8}$$

where E_1 is the exponential integral defined in Eq. 2.6, of first order (Finck, 1992). A is now the activity per unit area, Bq m^{-2}. In practice, Eq. 2.8 will always underestimate the activity deposition, since only attenuation in the air is accounted for. The radionuclide may penetrate into the ground or be shielded by surface roughness, effectively attenuating the primary photons.

Models consisting of a number of uniform slabs have been suggested. Kocher and Sjoreen (1985) and Finck (1992) described a one-slab model in the top soil layer to model fresh fallout. Boson et al. (2006) extended this to a three-slab model, that is able to model any kind of depth distribution. Creating a slab of the top soil layer is easily done using the difference between two uniform volume sources, one starting at zero depth and the other at a depth z. Too see this, change the integration interval of Eq. 2.4 from $[h \sec\theta, \infty]$ to $[(h+z)\sec\theta, \infty]$ and solve the integrals. The primary photon fluence rate at D from a slab with thickness z is then

$$\phi_p = \frac{A \cdot n_\gamma}{2\mu_s}\big(\mathrm{E}_2(\mu_a h) - \mathrm{E}_2(\mu_s z + \mu_a h)\big) \tag{2.9}$$

To avoid the underestimation of activity deposition associated with the surface model when modelling fresh fallout, a surface slab can be used instead. Assuming that the deposited activity is located in this slab the humus and top soil layer can be modelled through the density,

i.e. through the attenuation coefficient, μ_s. For example, the model used by the Swedish defence research agency assumes a 2 cm thick slab with a density of 500 kg m^{-3} (Lidström and Nylén, 1998).

Angular distribution

Most detectors have an angular dependence, that is, their efficiency, ϵ, is a function of not only the energy, but also the polar angle: $\epsilon = \epsilon(E, \theta)$. It can therefore be interesting to study the primary photon fluence rate, differentiated with respect to the polar angle. An expression for $\frac{\mathrm{d}\phi_p}{\mathrm{d}\theta}$ in the case of a uniform volume source can be obtained by dividing each side of Eq. 2.3 with $\mathrm{d}\theta$

$$\frac{\mathrm{d}\phi_p}{\mathrm{d}\theta} = \frac{A \cdot n_\gamma}{2} \int_{h \sec\theta}^{\infty} \sin\theta \exp(-\mu_s(r - h\sec\theta) - \mu_a h \sec\theta)\,\mathrm{d}r \quad (2.10)$$

carrying out the integration, as shown above, gives the primary photon fluence rate at D for a uniform volume source differentiated with respect to the polar angle:

$$\frac{\mathrm{d}\phi_p}{\mathrm{d}\theta} = \frac{A \cdot n_\gamma}{2\mu_s} \sin\theta \exp(-\mu_a h \sec\theta) \quad (2.11)$$

Put in relation to the total primary fluence rate, an expression for the primary fluence fraction, ϕ_f, can be obtained

$$\begin{aligned} \phi_f(\theta') &= \frac{\frac{A\cdot n_\gamma}{2\mu_s} \int_0^{\theta'} \sin\theta \exp(-\mu_a h \sec\theta)\,\mathrm{d}\theta}{\frac{A\cdot n_\gamma}{2\mu_s} \int_0^{\pi/2} \sin\theta \exp(-\mu_a h \sec\theta)\,\mathrm{d}\theta} \\ &= \frac{1}{\mathrm{E}_2(\mu_a h)} \int_0^{\theta'} \sin\theta \exp(-\mu_a h \sec\theta)\,\mathrm{d}\theta \end{aligned} \quad (2.12)$$

where

$$\begin{aligned} &0 \le \theta' \le \frac{\pi}{2}, \quad \text{and thus} \\ &0 \le \phi_f \le 1 \end{aligned}$$

Equation 2.12 was used in Paper III to limit the area that should be considered when comparing airborne and terrestrial measurements. It is interesting to note that the primary fluence fraction, ϕ_f, does not depend on the soil attenuation coefficient, so that a semi-infinite volume source gives the same fluence fraction for all soil types.

2.2 Natural background radiation

All half-lives, γ-energies, emission probabilities and abundances presented in this thesis are from Table of Radioactive Isotopes (Chu et al., 1999).

Ambient background

Everywhere on the surface of Earth the ambient ionizing background radiation is present, since all matter is radioactive to some extent. Gamma radiation can be detected deep inside the Earth's crust or out on the open oceans (UNSCEAR, 2000). This chapter discusses the most important gamma-emitters from a mobile gamma-ray spectrometry point of view, that is, the radioactive nuclides which dominate the natural radiation background below 3 MeV.

Historical perspective

Henri Becquerel discovered radioactivity in 1896 while working with uranium ore. Two years later Marie Curie and C.G. Schmidt independently showed that also thorium was radioactive. As Ernest Rutherford began to study the "Becquerel rays's" passage through layers of aluminium foil in 1899, he soon discovered two different components which he named alpha (α) and beta (β). A year later Paul Villard discovered a third type of radiation, even more penetrating, it was subsequently named gamma (γ) after the third letter in the Greek alphabet. In the years 1901-1903 Rutherford, now working with Frederick Soddy, established the concept of radioactive half-life through observations of the thorium decay chain.

During the first decade of the 20th century, the number of scientists working with the penetrating rays which seemed to originate from within the (so far) impermeable atoms increased. McLennan performed measurements on a lake and proved that the major part of the background radiation came from radionuclides in the ground. Scientists began to realise that the radiation came not only from the ground but also from space. In 1911 and 1912, Hess made a number of balloon ascents up to 5300 m and observed an unexpected increase in the radiation levels at altitudes over about 1000 m due to cosmic radiation. Excellent reviews of these historical events can be found in Franklin (2002); Gerward (1999); Simmons (1996) and the Nobel lectures (Nobelstiftelsen, 1965).

Background components

Today we know that Naturally Occurring Radioactive Materials, or NORM, as the name suggests, exist naturally everywhere on Earth, albeit at different concentration levels. There are four components that comprise the radiation background (UNSCEAR, 2000):

Terrestrial sources
: Primordial radionuclides occurring as decay series: ^{235}U, ^{238}U and ^{232}Th or as singles, e.g. ^{40}K and ^{87}Rb

Cosmic radiation
: Subatomic particles: atomic nuclei, protons or electrons

Cosmogenic sources
: Nuclides produced by cosmic radiation, e.g. ^{14}C, ^{7}Be and ^{3}H

Man-made sources
: Nuclear fission products e.g. ^{137}Cs, ^{90}Sr and ^{131}I or industrial or medical sources e.g. ^{60}Co, ^{192}Ir and ^{90}Y

of which the first, terrestrial sources (NORM), dominate the ambient gamma radiation background at the ground level. In some areas man-made nuclides also comprise a significant amount of the total background radiation, e.g. the Gävle region in Sweden (Mellander, 1988); the Bryansk region in Russia (Bernhardsson et al., 2011) and the Fukushima prefecture in Japan (Yoshida and Kanda, 2012).

Decay chains

The three decay chains that today exist in nature all decay to different lead isotopes through α or β disintegrations. In an α-decay, the mass number (A) is reduced by 4, while β-decay only changes the atomic number (Z). Since almost all loss in mass is due to α-decays, the three decay series are unambiguously distinct by the mass number. They are therefore sometimes referred to by their mass number modulo four, so that for example ^{238}U belongs to the "4n+2"-series because $238 \equiv 2 \pmod 4$.

Uranium series

The series of the 4n+2 chain, starting with ^{238}U ($t_{1/2} = 4.47 \times 10^9$ y) is known as the "uranium series" but can sometimes also be referred to

as the "radium series". The latter name is due to the presence of ^{226}Ra, which is the fifth daughter counting from ^{238}U, cf. Table 2.1. ^{226}Ra is also the parent of ^{222}Rn (radon), a noble gas whose progenies cause the majority of the radiation dose received by the general public from natural sources (UNSCEAR, 2000). Radon is also the primary cause of lung cancer among non-smokers (WHO, 2009).

Conventionally, ^{238}U-concentrations are inferred through the radon daughter ^{214}Bi under assumption of secular equilibrium and uniform activity distribution. The term equivalent uranium (eU) implies these assumptions (ICRU, 1994). ^{214}Bi has several γ-lines, e.g. 609.3 keV (46.1 %) and 1764.5 keV (15.4 %), the latter being the centre of the standard U-window (IAEA, 1991). Estimation of ^{238}U activity assuming equilibrium is problematic due to chemical dissimilarities between uranium and some of its daughters and the gaseous nature of ^{222}Rn (radon loss). The rate of radon diffusion from the ground depends on such factors as air pressure, soil moisture, ground cover, wind and temperature (IAEA, 1991).

Thorium series

Natural thorium comprises ^{232}Th ($t_{1/2} = 1.41 \times 10^{10}$ y), the mother of the 4n chain, to all but trace amounts. Five nuclides: ^{228}Ac, ^{224}Ra, ^{212}Pb, ^{212}Bi and ^{208}Tl can be detected by gamma spectrometry, c.f. Table 2.1. The series is branched after ^{212}Bi due to its 35.9 % probability of undergoing alpha decay. Since the daughter of this branch, ^{208}Tl, has a 99 % line at 2614.5 keV, ^{232}Th activity is usually inferred through ^{208}Tl (IAEA, 1991) and reported as eTh (ICRU, 1994). Radon loss is less of a problem in the thorium series. Due to the relatively short half-life of ^{220}Rn, equilibrium will be re-established within minutes even if the gas "escapes" (Gilmore, 2008).

Actinium and Neptunium series

The last two decay series are not as important as the U and Th-series from a mobile gamma spectrometry point of view. In the case of the neptunium series, which is the 4n+1 decay chain from ^{237}Np, the reason is simply that primordial ^{237}Np no longer exists on Earth because of its geologically short half-life ($t_{1/2} = 2.14 \times 10^{6}$ y). The 4n+3 actinium series still exists, but gives a relatively small contribution to the ambient gamma background. Only about 0.72 % of all natural uranium is ^{235}U ($t_{1/2} = 7.04 \times 10^{8}$ y), the head of the actinium series (Chu et al., 1999).

	Isotope	Half-life	Isotope	Half-life
(1)	^{238}U	4.47×10^{9} y	^{232}Th	1.41×10^{10} y
	$\downarrow \alpha$		$\downarrow \alpha$	
(2)	^{234}Th*	2.08×10^{6} s	^{228}Ra	5.75×10^{0} y
	$\downarrow \beta^-$		$\downarrow \beta^-$	
(3)	^{234m}Pa*	7.02×10^{1} s	^{228}Ac*	2.21×10^{4} s
	$\downarrow \beta^-$		$\downarrow \beta^-$	
(4)	^{234}U	2.46×10^{5} y	^{228}Th	1.91×10^{0} y
	$\downarrow \alpha$		$\downarrow \alpha$	
(5)	^{230}Th	7.54×10^{4} y	^{224}Ra*	3.16×10^{5} s
	$\downarrow \alpha$		$\downarrow \alpha$	
(6)	^{226}Ra*	1.60×10^{3} y	^{220}Rn	5.56×10^{1} s
	$\downarrow \alpha$		$\downarrow \alpha$	
(7)	^{222}Rn	3.30×10^{5} s	^{216}Po	1.45×10^{-3} s
	$\downarrow \alpha$		$\downarrow \alpha$	
(8)	^{218}Po	1.86×10^{2} s	^{212}Pb*	3.83×10^{4} s
	$\downarrow \alpha$		$\downarrow \beta^-$	
(9)	^{214}Pb*	1.61×10^{3} s	^{212}Bi*	3.64×10^{3} s
	$\downarrow \beta^-$		$\downarrow \alpha$ (35.9 %)	
(10)	^{214}Bi*	1.19×10^{3} s	^{208}Tl*	1.84×10^{2} s
	$\downarrow \beta^-$		$\downarrow \beta^-$	
(11)	^{214}Po	1.62×10^{-4} s	^{208}Pb	stable
	$\downarrow \alpha$			
(12)	^{210}Pb*	2.23×10^{1} y		
	$\downarrow \beta^-$			
(13)	^{210}Bi	4.33×10^{5} s		
	$\downarrow \beta^-$			
(14)	^{210}Po	1.20×10^{7} s		
	$\downarrow \alpha$			
(15)	^{206}Pb	stable		

Table 2.1: The uranium (left columns) and thorium (right columns) decay series. Daughters marked with an asterisk (*) can be measured by gamma spectrometry. Some of the less relevant branchings are omitted from the table. Throughout this work ^{214}Bi and ^{208}Tl was used for eU and eTh estimation, respectively.

Other isotopes of interest

There are other primordial nuclei with Z $<$ 82 (Pb), for instance: ^{40}K, ^{87}Rb, ^{138}La, ^{147}Sm and ^{176}Lu. However, most sub-lead primordials do not contribute much to the ambient gamma radiation background. The exception is ^{40}K with a half-life of 1.277×10^9 y which normally dominate the natural gamma background. ^{40}K constitutes about 0.0117 % of all potassium, which is a soft metal found in most soil types and plants (UNSCEAR, 2000).

^{40}K decays through β^- (89.3 %) to ^{40}Ca or through electron capture (10.7 %) to ^{40}Ar. The latter decay is accompanied by a single subsequent gamma emission at 1460.8 keV by which ^{40}K is measured. Many scientists ignore the interfering 1459.1 keV (0.8 %) line of ^{228}Ac, which could lead to overestimation of ^{40}K activity, especially in samples where ^{232}Th concentrations are high (Lavi et al., 2004).

Potassium is also a necessary nutrient for humans; about 0.18 % of the body content is potassium. Thus a 70 kg adult contains about 125 g of potassium. For a given mass m of an isotope with atomic mass m_a and half-life $t_{1/2}$ s, the activity in Bq is

$$A = N_A \frac{m}{m_a} \cdot \frac{\ln(2)}{t_{1/2}} \tag{2.13}$$

which corresponds to an activity of about 3.8 kBq from ^{40}K in a 70 kg adult (N_A being the Avogadro constant). The body content of ^{40}K will thus introduce a systematic uncertainty to the measurements when carrying a portable spectrometer close to the body.

The global mean soil concentration of ^{40}K is estimated to be 400 Bq kg^{-1} and in Sweden even higher, 780 Bq kg^{-1} (UNSCEAR, 2000). Assuming typical air and soil densities and attenuation coefficients (cf. Table 2.2) and the Swedish mean value for ^{40}K activity per unit mass, the primary fluence rate at the height of the portable spectrometer, say 1.5 m above ground, is given by Eq. 2.5 in Section 2.1

$$\phi^K_{p,ground} \approx \frac{780 n_\gamma 1.5 \cdot 10^3}{2\mu_s} \mathrm{E}_2(1.5\mu_a) = 7.4 \cdot 10^3 \,\mathrm{s}^{-1}\mathrm{m}^{-2} \tag{2.14}$$

ignoring attenuation in the person carrying the detector.

To estimate the primary fluence rate at the same point from ^{40}K in the body, a simple Monte Carlo simulation[1] using a $0.3 \times 0.2 \times 2$ m^3

[1] Using the Monte Carlo N-Particle transport code (MCNP5), Los Alamos National Laboratory, USA.

Table 2.2: Attenuation coefficients, μ, for air, soil and tissue at 1.46 MeV (^{40}K).

	μ (m^{-1})	Assumed ρ (kg m^{-3})	Reference
Air	$\mu_a = 6.5 \cdot 10^{-3}$	1.2	Boson et al. (2006)
Soil	$\mu_s = 8.3$	$1.5 \cdot 10^3$	Boson et al. (2006)
Water	$\mu_w = 5.7$	$1.0 \cdot 10^3$	Hubbell and Seltzer (2004)

water phantom with ^{40}K activity evenly distributed in the body gave a primary photon fluence of ~ 0.05 m^{-2} (per emitted γ) at a point located 5 cm outside the centre of the phantom. Assuming a whole-body content of 3.8 kBq, cf. Eq. 2.13, the primary fluence rate from ^{40}K in the body is approximately

$$\phi^K_{p,body} \approx 3.8 \cdot 10^3 n_\gamma \cdot 0.05 = 2.0 \cdot 10^1 \, \mathrm{s}^{-1}\mathrm{m}^{-2} \tag{2.15}$$

In this simplified scenario, ^{40}K from the ground is expected to give two orders of magnitude more photons to the full energy peak than ^{40}K from the person carrying the equipment. In reality, the systematic uncertainty caused by internal ^{40}K activity is negligible, which also was the approach in Paper III.

2.3 Mobile measurements

Aerial surveys

Minty (1997) and Tyler (2008) address the fundamentals of airborne gamma-ray spectrometry, from the basic properties of radioactive decay to the more complex features of an airborne spectrum. A typical AGS system consists of a helicopter or fixed-wing aircraft carrying one or more large NaI(Tl) detectors, sometimes accompanied by an HPGe detector for identification purposes. The aircraft is flown in straight lines over the area to be mapped. Altitude correction due to attenuation in air is used and for geological mapping purposes one or two extra NaI(Tl) detectors are added to account for radon daughters in the air.

Presently, most developed countries have developed AGS platforms; a comprehensive review of the capabilities in Europe can be found in Sanderson and Ferguson (1997). Sanderson et al. (2001) have also composed a useful bibliography of the AGS research in Europe. In many countries AGS systems where developed for geophysical applications, e.g. mineral exploration and geological mapping (Bristow, 1983;

Grasty, 1995; Martin et al., 2006; Zhang et al., 1998; Åkerblom, 1995). IAEA (1991, 1995) reports on the use of AGS to create dose rate and radon potential maps; monitoring of nuclear power plants and nuclear fuel cycle facilities; and its potential use in emergency response.

In Sweden, the Geological Survey of Sweden (*sv.* Sveriges Geologiska Undersökning, SGU) have conducted AGS surveys since the late 1960's. At first, the purpose of the measurements was to identify and locate ^{238}U deposits suitable for mining, but later also ^{232}Th and ^{40}K concentrations became of interest. The radionuclide concentration database currently covers about 80 % of Sweden's area, flown at 30-60 m altitude with 200-800 m interspacing between flight lines (Mellander, 1988).

AGS data from the southernmost part of Sweden, Scania (*sv.* Skåne), showing K, eU and eTh concentrations are given in Figs. 2.2-2.4. These maps were composed from about 2.6×10^6 measurements interpolated onto a grid with 300×300 cells. The concentrations given in the figures were derived by the SGU assuming a semi-infinite uniform volume source, as described in Section 2.1. Excerpts of the AGS data sets were used for ground-to-air comparisons (Paper III) and for background estimation at the ground level (Paper IV). An overview of the survey sites of the different papers is given in Fig. 2.5.

Car-borne surveys

Much alike AGS, car-borne gamma-ray spectrometry (CGS) generally employs large NaI(Tl) systems, with an additional HPGe primarily used for nuclide identification, cf. e.g. Hovgaard et al. (1997) and Sanderson et al. (2003). As pointed out by Tyler (2008), in case of mapping of nuclear fallout an HPGe may suffice due to the higher dose rates and many exotic peaks of a fresh fallout spectrum. But generally, and especially in environmental monitoring applications and in orphan source searches, high efficiency is an advantage. Thus, NaI(Tl) is still the workhorse in CGS as well as in AGS, due to the large size crystals available at a relatively low cost.

Although four wheel drive vehicles is an option, a car is still largely confined to roads. This will reduce the potential of CGS in applications like contamination mapping, especially when large areas are to be surveyed; AGS is then the best option. Confinement to roads may also lead to bias, due to the shielding of the ground and different radionuclide compositions of the road and the ground (Sanderson et al., 2003). The best use of CGS is when flexibility, good spatial resolution and cost-effectiveness are priorities.

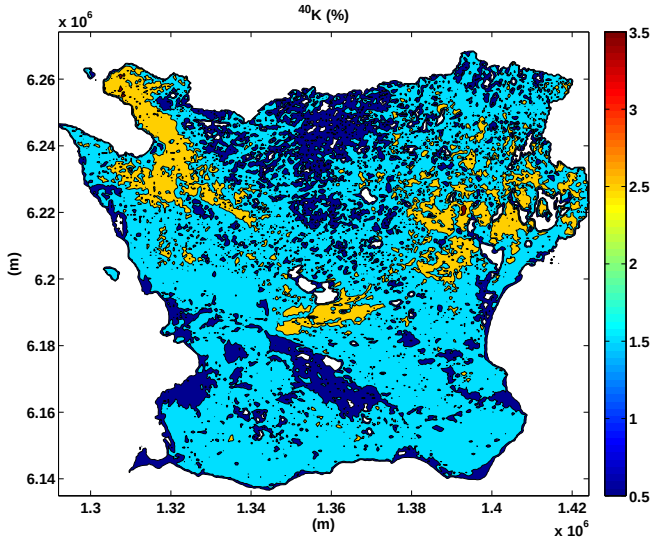

Figure 2.2: ^{40}K concentrations for Scania from the SGU.

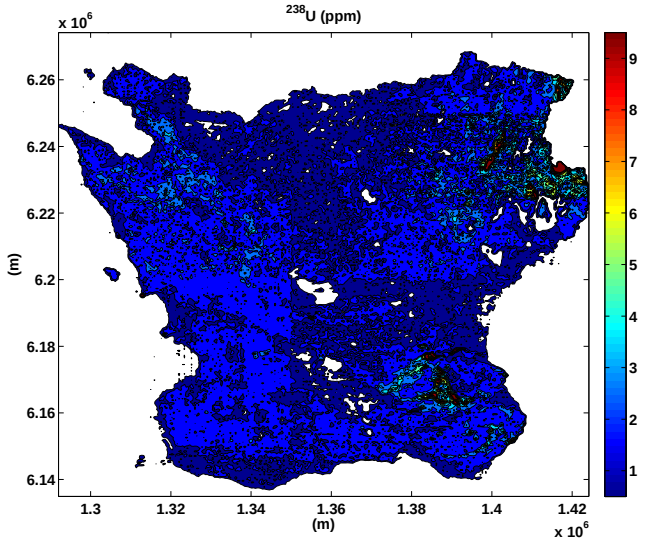

Figure 2.3: eU concentrations for Scania from the SGU.

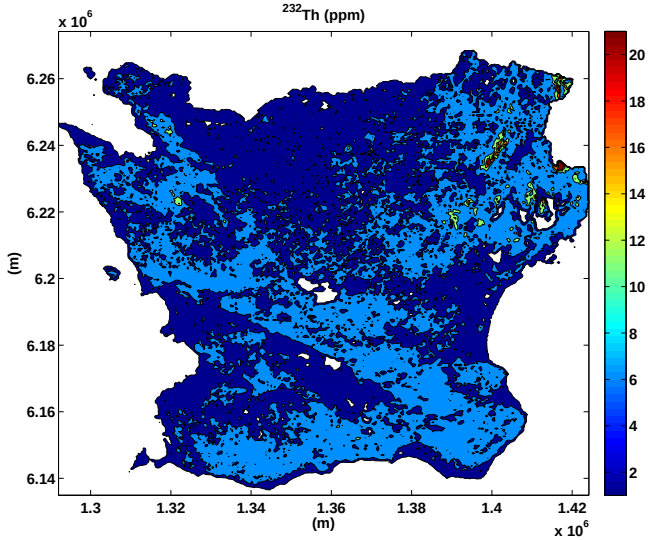

Figure 2.4: eTh concentrations for Scania from the SGU.

In Papers I and IV we use CGS as a means for orphan source search, whereas Paper V investigates the impact of vibrations on an HPGe system mounted in a vehicle.

Time series

Non-random data

A sequence of data points, measured at a fixed time interval is called a time series. The description fits the properties of mobile gamma-ray spectrometry, where a new spectrum (or data points) is sampled at an uniform time interval, t. Typical measurement times range from less than a second (AGS) to a couple of seconds (CGS). A problem with this kind of sampling is that the data points may not be independent, since the field of view of consecutive measurements will overlap and the background levels may change. One way to test for randomness, or independence, is to calculate the autocorrelation. The lag k autocorrelation of a sample, X_i, measured at time i to the sample measured at time $i+k$

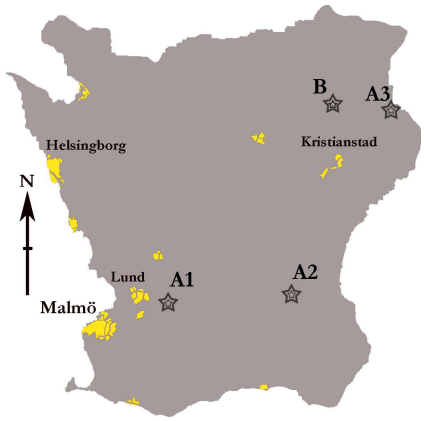

Figure 2.5: Map of Scania with the survey sites of Paper III (A1-A3) and Paper IV (B) marked. Revingehed (A1) was also the site of the experiments of Paper I and Paper V. The map was adapted from Paper III.

is

$$r_k = \frac{\sum_{i=1}^{n-k}(X_i - \bar{X})(X_{i+k} - \bar{X})}{\sum_{i=1}^{n}(X_i - \bar{X})^2} \tag{2.16}$$

where $\bar{X}$ is the mean and n the sample size (Box and Jenkins, 1976). Eq. 2.16 evaluates to unity if perfect (positive) correlation exist between the variable, X, at times i and $i + k$. A sample in mobile gamma-ray spectrometry would be an integrated count rate, typically from a part of the spectrum, and collected for a given time. All papers except Paper II evaluate data in the form of time series, but the concept is explored mainly in Paper IV.

Random data

When working with random data sequences, i.e. data for which r_k is close to zero, the situation is less complex. A set of mobile measurements can then be used in the same way as a set of stationary measurements would have been used. Probability tails and critical values found in tables can be directly applied to infer radioactivity using e.g. a set of previous samples as an independent background estimate to the current sample.

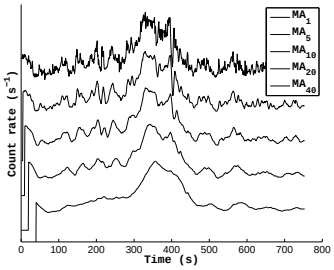

Figure 2.6: The effect of different sample sizes (background lengths), n, of the moving average MA_n. As n is increased the level of smoothing is also increased but the position of the peak around $t = 325$ s is also shifted due to lag. Adapted from Paper IV.

Moving average

Successive measurements can, despite of autocorrelation, still be used as an estimate of the background. The moving average (MA), also referred to as a rolling average, of the n latest measurements is:

$$\mathrm{MA}_n = \frac{1}{n} \sum_{k=t-n}^{t-1} C_k \tag{2.17}$$

where C_t are the counts in the region of interest at time t. Longer averaging times, n, results in more smoothing and less uncertainty in MA_n. While this generally is favourable, it can also lead to lag when the background levels change. Both these effects can be seen in Fig. 2.6.

2.4 Hypothesis testing

Statistical hypothesis testing can be used to test whether a hypothesis is true (or false). To be absolutely certain when making the decision, one would have to examine the entire population concerned, which is impractical and often impossible. Instead we use samples drawn from the population; consequently decisions concerning the hypothesis have to be based upon the information contained in the samples (Dixon and Massey, 1957).

To infer if a signal from a radioactive source is present in a sample (measurement) one can construct a null hypothesis, H_0, that the Poisson means of the (independent) background counts, λ, and the current sample counts, μ, are the same:

$$H_0 : \mu = \lambda \tag{2.18}$$

consequently, the research hypothesis, H_1, is

$$H_1 : \mu \neq \lambda \tag{2.19}$$

Table 2.3: Relations between the null hypothesis, H_0, and the outcomes of a statistical test.

Outcome	H_0 true	H_0 false
Reject H_0	False positive (α)	True positive
Fail to reject H_0	True negative	False negative (β)

Ideally, a statistical test rejects H_0 at a level of significance α with probability α of falsely rejecting the null when it is in fact true, also called a false positive or Type I error. Analogously, a false negative (β) or Type II error is a failure to reject the null when it is in fact true, cf. Table 2.3 (Barlow, 1989).

When working with discrete data, like those in a radioactive counting experiment, some methods fail to reject H_0 100α % of the time, under H_0. For instance, the cumulative binomial method, commonly referred to by the health physics community as the Sumerling and Darby (1981) (S&D) method, is actually very conservative. That is, the actual false positive rate of the method is $\alpha' < \alpha$ (Strom and MacLellan, 2001). The problem is well known and is ultimately due to the discreteness of the data (Agresti and Gottard, 2005, 2007; Berry and Armitage, 1995; Cousins et al., 2008, 2010; Lancaster, 1961). The general theory of tests of hypotheses described above is used mainly in the theoretical Paper II, but also in Papers I and IV-V.

2.5 Microphonic noise

Mechanical movements and vibrations affect the electronic components, inducing microphonic noise in any system. In a HPGe system, the vibrations can cause small movements of the detector mounting components, which may alter the capacitance between the field-effect transistor (FET) gate and the bias supply (Gilmore, 2008). Figure 2.7 shows the basic components of an HPGe system. The change in capacitance mentioned by Gilmore would then take place along the line between the FET and bias supply blocks in Fig. 2.7.

Mobile measurements in the field will inevitably cause some mechanically induced vibrations, primarily due the movement of the vehicle. Paper V investigates the spectrum perturbations from microphonic noise due to vibrations in a mobile system. Additional sources of concern are acoustic noise and events connected to the liquid nitrogen such as boiling

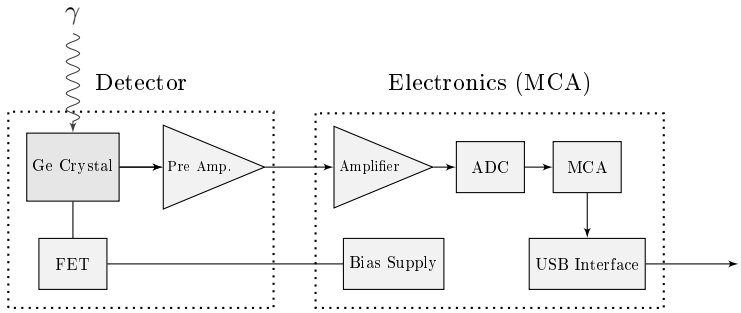

Figure 2.7: Block diagram of HPGe electronics. The arrows indicate the direction of a signal due to creation of an electron-hole pair in the germanium crystal. The analogue signal is collected and shaped in the pre-amplifier, amplified and digitized in the amplifier and analogue-to-digital converter (ADC) and sent over the USB interface via the multichannel analyzer (MCA). Based on Fig. 2.4 in ICRU (1994).

or turbulence in the Dewar (Morales et al., 1992). Apart from economical and practical reasons with less maintenance, the microphonic noise induced by the liquid nitrogen is perhaps the most important reason to continue the development of electrically cooled HPGe-detectors.

The microphonic noise manifests as low-energy pulses in the spectrum. Even a very small change in capacitance of 10^{-7} pF can induce a signal equivalent to a few keV (Gilmore, 2008). The microphonic noise is added to the other sources of noise (electronics, electron-hole pair statistics etc.), and can be expected to affect the full width of a peak at half its maximum height (FWHM) in a negative way, i.e. the additional noise will deteriorate the resolution of the system. Since the efficiencies of semi-conductor systems still are inferior to those found in large scintillation systems, the HPGe is primarily used for identification. The negative effect that microphonic noise can have on the FWHM is therefore a matter of great concern.

Chapter 3

Materials and methods

3.1 Spectrometry systems

The CGS and backpack spectrometer systems used in Papers I and III-V are summarised in Table 3.1. Here follows a short description of the spectrometry systems used in this thesis. For a more detailed description, the reader is referred to Papers I and III-V.

Airborne platform

The spectrometry system used by the Geological Survey of Sweden (SGU) is a 16.7 L NaI(Tl) mounted in a fixed-wing aircraft. The system was calibrated according to the procedure described in IAEA (1991), using three concrete pads with known concentrations of ^{40}K, ^{238}U and ^{232}Th, respectively and a fourth null pad for background correction. Stripping ratios and unit spectra (cf. Section 3.2) were then calculated and used to estimate K, eU and eTh concentrations in the ground, assuming uniform depth distributions. At the time when the area in Paper IV and one of the areas in Paper III were surveyed, SGU used a 6 L NaI(Tl), calibrated by the same method. Currently, SGU uses a 4 L NaI(Tl) to account for radon daughters in the air.

Car-borne platform

The Swedish Radiation Safety Authority (SSM) has three pickup vans equipped for conducting CGS surveys, cf. Fig. 3.1. Each van holds 2×4 L NaI(Tl) crystals (Detector system 3), mounted on a rail system which is suspended in the roof of the rear compartment of the van. The

Figure 3.1: The mobile gamma-ray spectrometry vehicle of the SSM, used in Paper IV. The blue boxes suspended in the roof are the two NaI(Tl)-detectors, whereas the HPGe (beige-coloured cryostat) can be seen in the centre of the rear compartment. *Image courtesy of Bosse Alenius, SSM.*

rail system offers positional flexibility. In Paper IV, the detectors were fixed at positions as far away from each other as possible; one at the left side and the other at the right side of the van. The detector signals of the two systems can be merged, online or in the post processing, so that the effective detector volume is 8 L. In the centre of the rear compartment of the van there is also a slot for an HPGe (Detector system 1). In Paper IV, a $LaBr_3$:Ce (Detector system 4) was placed in the slot instead. This choice eliminated the need for liquid nitrogen without compromising with the ability to identify all gamma lines of interest.

For the mobile measurements conducted in Paper I and Paper V, a GMC van was used instead. The detector was held in place by ratchet tie downs on a layer of $\sim$10 cm polyester foam. The positions of the detector varied, but are described in detail in Paper I and Paper V. For Paper V a dampener was constructed. The cryostat of the HPGe was put in the centre of a PVC plastic tube and isolated at all sides with $\sim$10 cm thick polyester foam. Two wooden lids held the detector and isolation in place. Holes were drilled in the lids; in the back lid for nitrogen steam and in the front lid to allow the crystal to extend out from the dampener.

Table 3.1: Detector characteristics according to manufacturer's specifications. DigiDART and DigiBASE are electronics devices manufactured by ORTEC. Both have integrated bias supplies, analog-to-digital converters, amplifiers and digital multichannel analysers with USB connectivity for communication with a computer. The digiBASE, made for scintillation detectors, also has an integrated photomultiplier tube. All detector systems are more or less portable and can be powered by a PC.

	Detector system			
	1	2	3	4
Crystal	HPGe	NaI(Tl)	NaI(Tl)	$LaBr_3$:Ce
Volume (L)	0.48	0.35	2×4.00	0.35
Efficiency [a,b] (%)	123	100	N/A	143
Resolution[a] (%)	0.15	5.4	8.5[c]	2.1
Electronics	DigiDART	DigiBASE[d]	DigiBASE[d]	DigiBASE[d]
Used in	Paper I Paper V	Paper I Paper III	Paper IV	Paper IV

[a] At 1.33 MeV

[b] Relative to a 7.62×7.62 cm^2 NaI(Tl)

[c] At 662 keV

[d] An open source linux driver for DigiBASE was developed during my PhD studies and is available for download at: http://libdbase.sourceforge.net

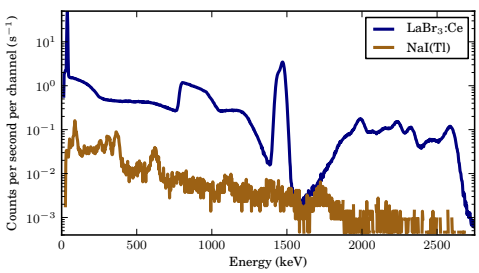

Figure 3.2: Count rates (s^{-1}) of the $LaBr_3$:Ce crystal (Detector system 4) and a NaI(Tl) of equal size (Detector system 2). The measurements were conducted in a shielded room with low levels of background radiation. From Nilsson et al. (2011).

Spectrometers

The detector systems are enumerated as listed in Table 3.1.

Detector system 1

A ruggedized, coaxial, p-type HPGe detector, $\varnothing = 84.0$, $z = 85.8$ mm, manufactured by ORTEC, connected to a 5 L Dewar specified

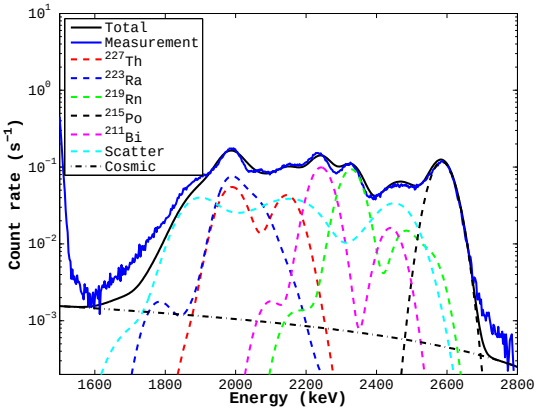

Figure 3.3: Simulated contributions of individual α-peaks from the ^{227}Ac decay series to the internal background of the $LaBr_3$:Ce crystal (Detector system 4). The measurement (blue solid line), cf. Fig. 3.2, is included for comparison. Adapted from Kock (2012).

to hold liquid nitrogen for 72 h (static).

Detector system 2

The backpack system used in Papers I and III consists of a cylindrical NaI(Tl), $\varnothing = 76.2$, $z = 76.2$ mm (3"$\times$ 3"), crystal from Saint-Gobain. The backpack system is also equipped with a computer and GPS unit for positioning.

Detector system 3

Two 4 L NaI(Tl) (4"$\times$4"$\times$16") from Saint-Gobain, each with its own MCA. The two signals were merged manually in Paper IV.

Detector system 4

The $LaBr_3$:Ce detector is cylindrical with $\varnothing = 76.2$, $z = 76.2$ mm (3"$\times$ 3") and manufactured by Saint-Gobain. Due to the presence of ^{227}Ac and ^{138}La in the crystal, cf. e.g. Nicolini et al. (2007), the detector has an internal background, shown in Fig. 3.2. The contribution from individual α-peaks in the actinium decay series are given in Fig. 3.3.

3.2 Visualisation

The typical mobile gamma-ray spectrometry system consists of one or several large-volume detectors and a GPS unit, both connected to a computer running in-house software. Generally, the lack of standardisation in the software area, especially when considering car-borne gamma-ray

spectrometry, has led many organisations to develop their own software using their own methods, many of which are not published in scientific journals.

The amount of data produced when conducting repeated short-term measurements can be quite large. One way to present the data sequences to a human operator in a comprehensive way is to use imaging; that is, to visually represent the data. When searching for orphan sources the search crew might be concentrating on a plot, or in worst case on raw spectra, for an extensive period of time. The need for some kind of filtration in the data presentation process in order to assist the operator has therefore been identified (Cresswell and Sanderson, 2009; Hjerpe and Samuelsson, 2003; Hjerpe et al., 2001; Hovgaard, 1997).

Waterfall plot

Let $\boldsymbol{q} = \{q_1, \ldots, q_k\}$ be a spectrum of k channels and

$$\mathbf{Q} = \begin{pmatrix} \boldsymbol{q_1} \\ \vdots \\ \boldsymbol{q_n} \end{pmatrix} \tag{3.1}$$

a matrix holding n spectra, each collected for a time t. $\mathbf{Q}$ can be presented on a computer screen using some set of colours, $\boldsymbol{c} = \{c_1, \ldots, c_a\}$, i.e. a colour scheme of a colours. Each element q_{ij} would have to be scaled onto the range defined by $\boldsymbol{c}$; that is, we have to perform

$$\mathbf{W} = \alpha \cdot \mathbf{Q} \tag{3.2}$$

to represent $\mathbf{Q}$ on the screen as $\mathbf{W}$. The constant α depends on the method, but $\alpha = a/\max(q_{ij})$ is a common choice and was used in Paper I.

The denotation of the colour-coded pulse height distribution matrix, $\mathbf{W}$, as a 'waterfall plot' probably comes from its resemblance to a waterfall. Due to the energy dependence of the detector efficiency and Compton scattering more pulses are usually registered in the low-energy region of a spectrum. If $\mathbf{W}$ plotted with the vertical axis going from low energy (top) to high energy (bottom) as in Fig. 3.4 (a), the name can be understood. The technique has also been referred to as the 'rainbow method' (Aage and Korsbech, 2003).

Filtered displays

Differential displays, for instance visualisation of

$$\mathbf{q}' = \mathbf{q}_t - \mathbf{q}_{t-1} \tag{3.3}$$

i.e. the difference between the current and the last measurement, can be a way of enhancing changes in spectral data. In Paper I we used a similar technique, but instead of studying the difference from Eq. 3.3 we used a set of previously measured spectra to estimate the background. We then visualised the changes by means of the difference between the current spectra, $\mathbf{q}_t$, and the background estimate.

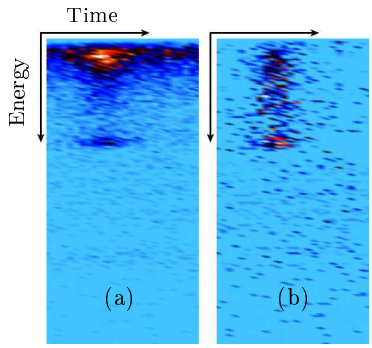

Figure 3.4: A NaI(Tl) ^{137}Cs passage visualised using the waterfall plot (a), cf. Eq. 3.2, and the deviation display (b), cf. Eq. 3.5. Both displays use a colour scheme of 256 colours. *Image courtesy of Jonas Nilsson, Lund University.*

The spectral windows method is a standard way to present data stripped from the natural decay series (U and Th) and potassium (IAEA, 1991, 1995; ICRU, 1994), widely used in AGS, cf. e.g. Grasty and Cox (1997) and Sanderson et al. (1997). If the energy response of the spectrometer is known then the mean natural background contribution in a given energy window can be subtracted, assuming an uniform activity distribution in the ground. A stipping matrix, $\mathbf{S}$, whose elements are the spillover ratios from the background nuclides to the energy windows of the others, can be constructed. The method is presented in Cresswell et al. (2006) as a sum over the j spectral windows

$$C_{si} = \sum_j C_{nj} s_{ij}^{-1} \tag{3.4}$$

where s_{ij}^{-1} are the elements of $\mathbf{S}$ after inversion, and C_{si} and C_{ni} the stripped and net counts in spectral window i, respectively. The method works well above 400 keV, but due to increased Compton scattering in

the low-energy region, leading to a non-flat background profile, the background estimation becomes difficult at lower energies (Martin-Burtart et al., 2012).

Cresswell and Sanderson (2009) used a filtered differential method to subtract the local background from the current spectrum. The local background was estimated using a moving average, cf. Eq. 2.17, constructed from recent spectra. Spectra showing significantly different levels than would be expected for a slowly varying radiation field were excluded from the analysis. A waterfall-like display was then constructed by means of the filtered local background.

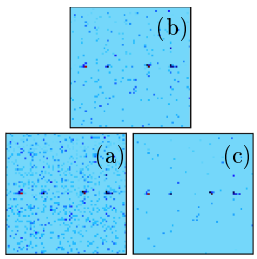

Figure 3.5: Example of deviation displays for three different smoothing constants: $N = 1$ (a); $N = 2$ (b) and $N = 3$ (c), cf. Eq. 3.5. Adapted from Paper I.

Deviation display

In Paper I we presented a method to create a smooth graphical interpretation using the difference between the current and a set of previous spectra. The background estimate can be constructed in different ways; we have used either a moving average or all previous measurements. Here, the length of the background is denoted by n[1]. Instead of storing the raw spectra, $\mathbf{q}$, as given in Eq. 3.1, the quantity

$$q_i = \max\left\{0, \frac{C_i - (m_i + N \cdot s_i)}{N \cdot s_i}\right\} \tag{3.5}$$

was calculated for each channel (or bin), i, where C_i are the counts, m_i and s_i the mean and sample standard deviation of the background estimate and N is a constant. An example is shown in Fig. 3.4 (b). The quantity in Eq. 3.5 is similar to what is commonly referred to as a z-score (Tewari et al., 1988), or standard score (Dixon and Massey, 1957), i.e. $z = \frac{x-\mu}{\sigma}$. The standard represents the distance between the raw score and the mean in units of standard deviation. The quantity in

[1] In Paper I it was denoted by j.

Eq. 3.5 is instead the distance from the raw score and the mean plus N sample standard deviations in units of N sample standard deviations, i.e. the constant N sets the level of smoothing applied to $\mathbf{Q}$, cf. Fig. 3.5. Negative values of q_i are ignored to enhance positive deviations in the display.

3.3 Statistical inference

In Paper II we break down the general hypothesis, given in Eq 2.18, into two new hypotheses. For a radioactive counting problem using k channels, we get

$$H_0^{(\mathrm{S})} : \sum_{i=1}^{k} \mu_i = \sum_{i=1}^{k} \lambda_i \tag{3.6a}$$

$$H_0^{(\mathrm{R})} : \mu_i/\mu = \lambda_i/\lambda \quad \text{for} \quad i = 1 \ldots k \tag{3.6b}$$

$$H_0^{(\mathrm{SR})} : \mu_i = \lambda_i \quad \text{for} \quad i = 1 \ldots k \tag{3.6c}$$

where μ and λ are the Poisson means of sample and background, respectively, and the superscripts S and R denote sum and ratio, respectively. The third hypothesis, Eq. 3.6c, is just a combination of Eqs. 3.6a and 3.6b. The advantage of the hypotheses above is that the spectrometric capability of the detector is reflected in the hypotheses (Eqs. 3.6b and 3.6c) as well as the classic problem of radioactive counting (Eq. 3.6a).

Tests on count rate

Since the publication by Currie in 1968, the health physics community has adopted his terminology (Currie, 1968, 1999). Today, critical levels (L_C) and detection limits (L_D) are widely used concepts, and even standards (HPS, 1996). However, the method of Currie is known to yield an excess of false positives since $H_0^{(\mathrm{S})}$ is rejected at the α-level for all non-zero sample counts, as long as the background count is zero (Strom and MacLellan, 2001).

In Paper II, where we also analyse the method of Currie, we try to solve this problem by using a modified version of Sumerling & Darby's (S&D) cumulative binomial test. By using a modification proposed by

Lancaster (1961), half the probability of the first term is subtracted

$$\begin{aligned} P_{\mathrm{SDmidp}} &= \frac{1}{2}P(X = x \,|\, x+y) + P(X > x \,|\, x+y) \\ &= \frac{1}{2}\binom{x+y}{x} q^x (1-q)^y + \sum_{i=x+1}^{x+y} \binom{x+y}{i} q^i (1-q)^{x+y-i} \end{aligned} \tag{3.7}$$

where x and y are the counts in sample and background respectively and $q = \mu/(\mu+\lambda)$, where μ and λ are defined above. Thus, $H_0^{(S)}$ is rejected at the α level if

$$P_{\mathrm{SDmidp}} \leq \alpha \tag{3.8}$$

where "midp" stands for midpoint, indicating that only half the probability at x is taken into account.

Tests on spectral distribution

If the i:th channel of a sample has true Poisson mean μ_i, then, and as shown in Paper II, the probability of observing a pulse configuration $\mathbf{x} = (x_1, \ldots, x_k)$ in channels $1, \ldots, k$ from sample, given a total of x pulses in the k channels, is a binomial

$$P(X_1 = x_1 | X_1 + X_2 = x) = \binom{x}{x_1} q_1^{x_1} (1-q_1)^{x-x_1} \tag{3.9}$$

or multinomial

$$P(\mathbf{X} = \mathbf{x} | X_1 + \cdots + X_k = x) = \binom{x}{x_1, \ldots, x_k} q_1^{x_1} \cdots q_k^{x_k} \tag{3.10}$$

probability, depending on the number of channels used, cf. Fig. 3.6. $q_i = \mu_i/\mu$ is the Poisson means fraction for channel i. For $k \geq 3$ the probability is multinomial and can be described by Eq. 3.10 and for $k = 2$ the probability is binomial and described by Eq. 3.9. The corresponding equations for the background sample can easily be constructed by replacing $\mathbf{x}$ with $\mathbf{y}$ and letting $q_i = \lambda_i/\lambda$.

Goodness-of-fit tests

In principle one can, given $\mathbf{x}$, $\mathbf{y}$ and enough computing time, calculate all the possible permutations and their corresponding probabilities. This approach is sometimes referred to as the naive approach (Nagarajan

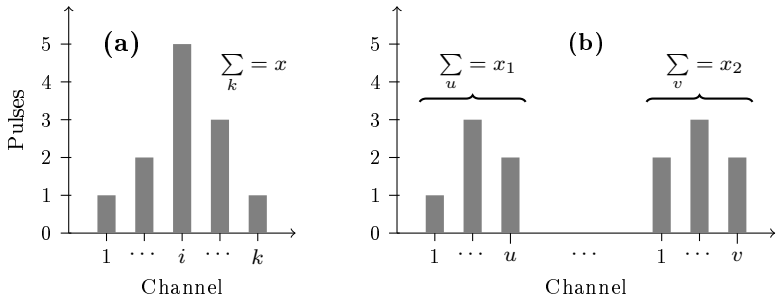

Figure 3.6: Two examples of spectral distributions. The probability of obtaining a pulse configuration within the channels, given a total count of x, can be calculated using Eqs. 3.10 and 3.9. In the left example (a), the multinomial probability is $P(\mathbf{X} = \mathbf{x}|X_1 + \cdots + X_k = x)$ whereas in the right example (b), two regions are analysed resulting in a binomial probability $P(X_1 = x_1|X_1 + X_2 = x)$.

et al., 2005). Once all probabilities are known the cumulative distribution function can be calculated by summing the individual probabilities (Cressie and Read, 1989). While the naive approach in one form or another has been suggested by some authors e.g. Méray (1994); Méray and Demény (2001) and Demény et al. (2002), it is easy to see that the complexity of the problem rapidly increases as the number of channels k and pulses x grow. In combinatorics, the problem is described by the classical urn problem with replacement but without ordering; there are

$$\binom{k+x-1}{x} = \frac{(k+x-1)!}{x!\,(k-1)!} \tag{3.11}$$

ways to arrange x pulses in k channels (Blom, 1984). As an example, for $k = 6$ and $x = 25$, according to Eq. 3.11, there are

$$\binom{k+x-1}{x} = \frac{30 \cdot 29 \cdots 26}{5 \cdot 4 \cdot 3 \cdot 2} = 142506 \tag{3.12}$$

possible arrangements that need to be traversed in order to calculate the cumulative distribution function.

Keich and Nagarajan presented a way to avoid the complexity of the multinomial problem described above (Keich and Nagarajan, 2006; Nagarajan et al., 2005). They used a fast Fourier transform (FFT) approximation, thereby avoiding the aforementioned permutations. However, as their method is based on a goodness-of-fit for of multinomial model, the cell probabilities q_i (cf. Eq. 3.10) have to be known. The FFT method of Keich and Nagarajan was also analysed in Paper II.

Likelihood ratio tests

The principle of maximum likelihood (ML) is a method for estimation. The maximum likelihood estimator (MLE), $\hat{a}$, for a data sample $x_1, \ldots, x_k$, is the value of a for which the likelihood

$$\mathcal{L}(x_1, \ldots, x_k) = \prod P(x_i, a) \tag{3.13}$$

is at maximum. Since $\ln \mathcal{L} = \sum \ln P(x_i, a)$, the sum of the logarithms of the probabilities is often maximised instead, which gives the same maximum (Barlow, 1989).

Baker and Cousins (1984) analysed the likelihood function of a multinomial sample. The method proposed in Paper II is based on similar likelihood functions, but for a pair of multinomial observations: the sample, $\boldsymbol{x}$, and the background, $\boldsymbol{y}$, which are considered independent. By introducing $\xi_i = \mu_i/\mu$ and $\eta_i = \lambda_i/\lambda$, the likelihood function, cf. Eq. 3.13, for the pair can be written

$$\mathcal{L}(\boldsymbol{\xi}, \boldsymbol{\eta}) = c_x c_y \left(\prod_{i=1}^{k} \xi_i^{x_i} \right) \left(\prod_{i=1}^{k} \eta_i^{y_i} \right) \tag{3.14}$$

where c_x, c_y are constants.

Under $H_0^{(\mathrm{R})}$, i.e. $\boldsymbol{\xi} = \boldsymbol{\eta}$, the sum of the observations $z = x + y$ will also be described by a multinomial. Maximising the likelihood function for the sum $\boldsymbol{z}$ results in

$$\sup_{H_0} \mathcal{L} = c_x c_y \prod_{i=1}^{k} \left(\frac{z_i}{z} \right)^{z_i} \tag{3.15}$$

where $z_i = x_i + y_i$ and z_i/z is the MLE for bin i. However, under H_1 the supremum of Eq. 3.14 has to be used directly since $\boldsymbol{\xi} \neq \boldsymbol{\eta}$. The logarithm of the ratio of the maximised likelihood functions under H_0 and H_1 is the log-likelihood ratio statistic, Λ. In the limit of large counts, the statistic

$$-2 \ln \Lambda = 2 \sum_{i=1}^{k} \left\{ x_i \ln \left(\frac{x_i}{x} \right) + y_i \ln \left(\frac{y_i}{y} \right) - z_i \ln \left(\frac{z_i}{z} \right) \right\} \tag{3.16}$$

is approximately χ^2-distributed with $k - 1$ degrees of freedom (Wilks, 1938). Thus, $H_0^{(\mathrm{R})}$ is rejected at the α-level if:

$$1 - F_{k-1}(-2 \ln \Lambda) \leq \alpha \tag{3.17}$$

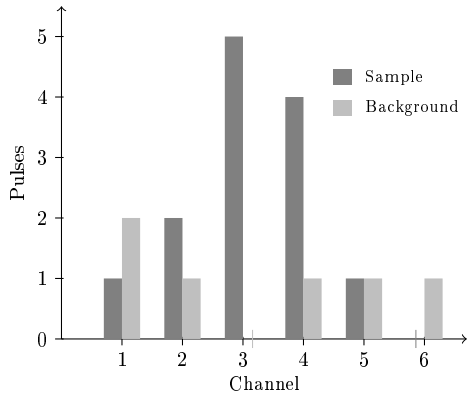

Figure 3.7: Example of a sample-background pair for $k = 6$. $x = 13$, $y = 6$ and hence $z = 19$. $p_S = 0.06$, $p_R = 0.14$ and $p_c = 0.05$. Noting that the source pulses can be expected in the centre channels, the channels are combined two and two (1&2, 3&4 and 5&6) and the test is repeated for $k = 3$, yielding $p_S = 0.06$, $p_R = 0.08$ and $p_c = 0.03$.

where $F_\nu(x)$ is the cumulative χ^2-distribution with ν degrees of freedom.

The likelihood method yields the multinomial probability in linear time; one would have to perform $\mathcal{O}(k)$ operations to get the answer using Eq. 3.16. Comparing with the example from the naive approach, as given in Eq. 3.12, the likelihood method involves 6 iterations, that is a factor 10^4 fewer iterations in this particular example.

In Paper II we also explored the possibility of constructing a one-sided test for the important case $k = 2$. The form

$$\Lambda_> = \begin{cases} \dfrac{\sup_{H_0} \mathcal{L}}{\sup_{H_1} \mathcal{L}} & \text{if} \quad \dfrac{x_1}{x} > \dfrac{y_1}{y} \\ 1 & \text{otherwise} \end{cases} \tag{3.18}$$

was presented and evaluated. In this case $H_0^{(\mathrm{R})}$ is rejected at the α-level if

$$1 - \frac{1}{2} F_1(-2 \ln \Lambda_>) \leq \alpha \tag{3.19}$$

Combining tests

In Paper II we combine the mid-p version of S&D's cumulative binomial method, cf. Eq. 3.7, with a one-sided likelihood ratio, cf. Eq. 3.18, by using the method proposed by Fisher (1932, 1948). Two independent tests can be combined through their p-values, p_1, p_2; the combined test will then have a p-value, p, of

$$p = (1 - \ln(p_1 p_2)) p_1 p_2 \tag{3.20}$$

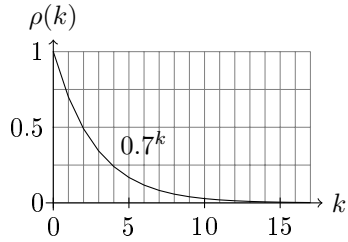

Figure 3.8: Plot of the autocorrelation function, $\rho(k) = 0.7^k$, used in Paper IV.

where $p \in \mathcal{U}(0,1)$. Fig. 3.7 presents an example where the p-value of a test based solely on count rate (p_S), cf. Eq. 3.8, is presented along with the p-value of a test based solely on the spectral distribution (p_R), cf. Eq. 3.17. The two p-values are then combined using Fisher's method, Eq. 3.20, resulting in the p-value of the combined test (p_c). The combined test is referred to in the text as the proposed test.

Correlated samples

Hjerpe et al. (2001) addressed the problem of autocorrelation, cf. Section 2.3, by approximating the full sample distribution prior to performing the actual mobile search. The downside of this approach is the fact that it cannot be applied to areas with unknown distributions. In Paper IV we address the issue of autocorrelation by applying a correction factor, $\sqrt{1/\gamma}$, to the sample standard deviation of the n background measurements, where

$$\gamma = 1 - \frac{2}{n-1} \sum_{k=1}^{n-1} \left(1 - \frac{k}{n}\right) \rho(k) \tag{3.21}$$

n is the sample size and $\rho(k)$ the autocorrelation function (ACF) (Shumway and Stoffer, 2011). Instead of estimating the autocorrelation by the use of Eq. 2.16 in Section 2.3 we simply assume an ACF which gives decreasing correlation as the lag, k, increases, cf. Fig. 3.8.

3.4 Ground-to-air comparisons

The ground-to-air comparisons presented in Paper III were done at three different locations in Scania, chosen for their different characteristics, cf. Figs. 2.2-2.5 in Section 2.3. An overview of the measurement points is given in Fig. 3.9.

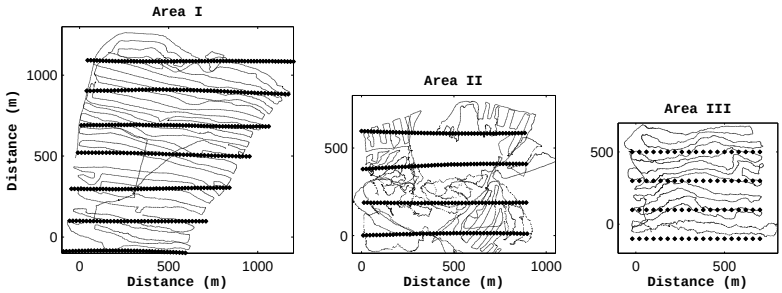

Figure 3.9: AGS flight lines (bold, horizontal lines) and ground samples (thin lines), plotted for the three survey areas. Adapted from Paper III.

Data validation

The primary fluence fraction, derived in Section 2.1

$$\phi_f(\theta') = \frac{1}{\mathrm{E}_2(\mu_a h)} \int_0^{\theta'} \sin\theta \exp(-\mu_a h \sec\theta)\, \mathrm{d}\theta \tag{3.22}$$

was used to compare two systems with different fields of view (FOV). In Paper III we evaluated the correlation between AGS and ground data measured with a portable spectrometer (Detector system 2) by using different θ' in Eq. 3.22. Measurements very far away from the point of interest, i.e. large θ', are not very representative for the local radiation environment and do not improve the correlation between the two sets. As shown in Fig. 3.10 up to about 90 % of the fluence generally improved the correlation, why all backpack measurements within the radius

$$r = h \tan\theta' \tag{3.23}$$

from a given AGS sample were included in the comparison, where $\phi_f(\theta') = 0.9$. The total backpack response was calculated by summation over all measurements within r using inverse distance weighting (Shepard, 1968). Fig. 3.11 shows the solutions for Eq. 3.22 as a function of the horizontal distance, i.e. the radius, r. As seen in the figure, typical optimal distances for data inclusion are in the range $r = [100, 200]$ m for $h = [30, 60]$ m.

In Paper IV, we used SSM's vehicle described in Section 3.1, which was equipped with 2×4 L NaI(Tl) (Detector system 3) and a 7.62×7.62 cm^2 $LaBr_3$:Ce (Detector system 4). For this study, no field of view

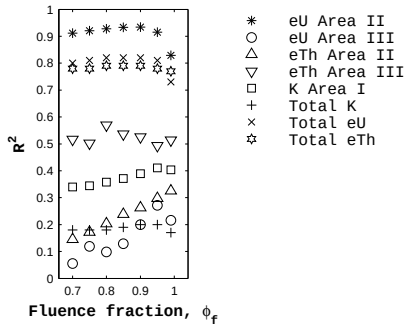

Figure 3.10: Coefficient of correlation, R^2, between data sets as a function of the primary fluence fraction. As the polar angle θ' is increased, the fluence fraction $\phi_f(\theta')$ and the correlation R^2 also increases, up to a certain point. Adapted from Paper III.

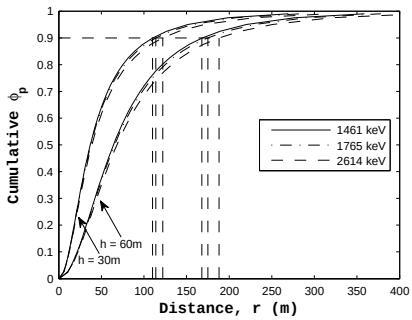

Figure 3.11: Theoretical cumulative primary photon fluence for a uniform depth distribution as function of the horizontal distance, r, at two flight heights, h. The vertical dashed lines mark the 90 % cumulative fluence radii. Adapted from Paper III.

correction was used. Instead, drawing on the results from Paper III, CGS data was normalised to the mean of the area and compared to normalised, gridded AGS data.

3.5 Background radiation gradients

The area surveyed in Paper IV contains strong, well-defined gradients in the background radiation, especially in the eTh component. As can be seen in Fig. 3.12, two routes, referred to in the text as route I and route II were defined along two of the roads passing through the area with elevated eTh-levels.

To account for the gradients we calculated the so-called step function, f'_{AGS}, which describes the slope of a gradient in a time series of measurements. For a discrete function, f'_{AGS}, is an approximation of the first derivative. The information from f'_{AGS} regarding the gradients was incorporated into a moving average, MA_n, cf. Eq. 2.17, by the use of

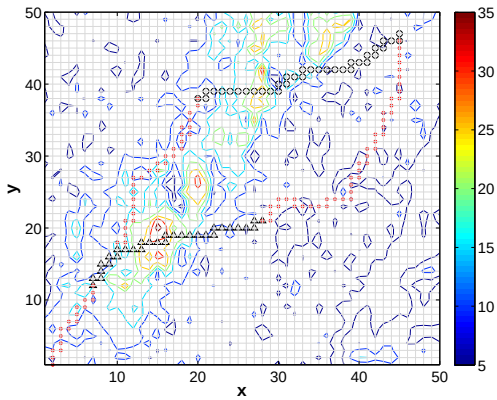

Figure 3.12: Contour plot of interpolated AGS eTh data (ppm) of the area from Paper IV. The cell size of the 50×50 grid is 180×180 m^2. Two excerpts from the roads, referred to as route I (black triangles) and route II (black circles) are also plotted. Adaped from Paper IV.

weights

$$\mathrm{MA}_n^w = \frac{1}{n} \sum_{k=t-n}^{t-1} C_k + w_k \tag{3.24}$$

where C_t are the CGS counts at time t and the superscript w stands for "weighted". The weights, w_t, were proportional to f'_{AGS}

$$w_t = 2\, s_{\mathrm{MA}} \cdot f'_{\mathrm{AGS}} \tag{3.25}$$

where s_{MA} is the sample standard deviation of the n CGS samples. Adjusting the mean from MA_n to MA_n^w, was our approach to solve the problem of excess false positives due to systematic variation in the background radiation levels. The problem with lag as shown in Fig. 2.6 should not be as serious when using weights; hence the sample size, n, was set to 40 to reduce the variance. Since $f'_{\mathrm{AGS}} < 0$ for negative steps, leading to negative weights, the sensitivity of a statistical test using MA_n^w rather than MA_n should also be improved in a negative gradient.

To determine the effect from the use of weights and autocorrelation correction factor, γ, described in Section 3.3, an upper 95 % prediction interval endpoint for the next sample, C_{t+1}, was calculated. Assuming that samples are normally distributed

$$U_{1-\alpha} = \mathrm{MA}_n + \sqrt{1 + \frac{1}{n}}\, T_{\alpha,n-1} \cdot s_{\mathrm{MA}} \tag{3.26}$$

is the upper interval endpoint, where $T_{\alpha,\nu}$ is the 100(1-α)th percentile of the Student's t-distribution with ν degrees of freedom (Walpole et al., 2002). The interval endpoint for the weighted moving average can be

obtained by substituting MA_n^w for MA_n in Eq. 3.26. Likewise, the bias-reduced sample standard deviation, $\sqrt{1/\gamma}\, s_{\mathrm{MA}}$, can be used instead of s_{MA} to account for autocorrelation in MA_n or MA_n^w.

3.6 Microphonic noise

In Paper V, the objective was to study the occurrence of microphonic noise induced from vibrations in a mobile gamma spectrometry system using an HPGe (Detector system 1). Accelerometers sampled (at 610 Hz) the frequencies and magnitudes of the vibrations in the x, y and z-directions. The study aimed at finding a correlation between vehicle speed and the number of microphonic events found in the low-energy region of the spectrum for two different detector mounting configurations. The use of accelerometers allowed for a study of the vibration frequencies and their connection to the induced microphonic noise using fast Fourier transform.

A statistical method was used to discriminate between normal and microphonic spectra. The mean sum of pulses with energies $10 \leq E \leq 100$ keV for the three latest spectra, $C = \frac{1}{3}(C_t + C_{t-1} + C_{t-2})$ (s^{-1}), measured while moving was compared to a static background count rate, C_0 (s^{-1}). The test statistic employed was

$$u = \frac{C - C_0}{s_c/\sqrt{3}} \tag{3.27}$$

where s_c is the sample standard deviation[2]. u, being a standardised variable, will have an approximate normal distribution with mean zero and unit variance, i.e. $u \sim \mathcal{N}(0,1)$. Using hypothesis testing, as described in Section 2.4, tables of the standard normal distribution at significance level $\alpha = 0.1\,\%$, the rejection limit is $\lambda_\alpha = 3.09$ (Blom, 1984). Samples for which $u \geq \lambda_\alpha$ are said to contain microphonic noise.

[2]In Paper V C was denoted by $\bar{x}$ and s_c by σ. The notation is changed, for conformity with the other formulae in this text.

Chapter 4

Results and comments

4.1 Visualisation

As illustrated in Fig. 4.1, the deviation display method presented in Paper I effectively homogenises the visual representation, suppressing the Compton scattering at low energies and the full absorption background peak lines of both detector systems as well as the internal background of Detector system 4. Figure 4.2 demonstrates the sensitivity of the deviation display method to weak signals at high energies ($E > 1.5$ MeV). Compared to the waterfall plot (a), where the anomaly also can be seen, it should be easier for an operator to detect the full extent of the signal in the deviation displays (b and c).

The length of the moving average, n, cf. Eq. 2.17 in Section 2.3, is an important issue and is discussed in Paper I and to some extent also in Paper IV. Ultimately, the validity of the background estimate depends on non-stochastical factors such as the geology of the measurement site. The data in Fig. 4.2 were measured in a high-variability area with ^{137}Cs fallout, near Gävle, Sweden. The shorter background (c) in the Figure shows a stronger signal compared to the longer background displays (a and b), but it also contains more noise. The impact of a longer background is similar to choosing a larger smoothing constant, N, cf. Fig. 3.5 in Section 3.2. Both alternatives lead to a more homogeneous, but also a more insensitive, display. Figures 4.1 and 4.2 were constructed using $N = 1$ and thus gives a visual representation of the standardised counts in each bin.

In Paper IV we try to minimise the impact of systematic variations in the background radiation due to geology by means of AGS background

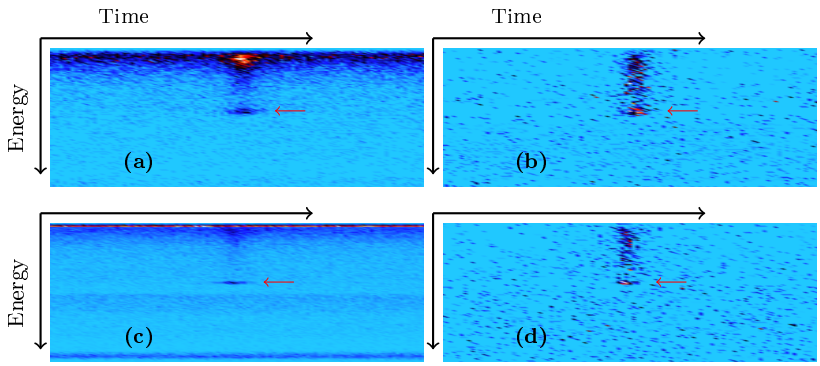

Figure 4.1: Comparison of waterfall plots (a, c) and deviation displays (b, d) for NaI(Tl) (Detector system 2, a and b) and $LaBr_3$:Ce (Detector system 4, c and d) detector types. A ^{137}Cs point source is passed by the detectors. The primary energy of ^{137}Cs (662 keV) is indicated by red arrows. Note the suppressed background in the deviation displays (b, d) in general and the suppressed internal background in the $LaBr_3$:Ce deviation display (d) in particular. Adapted from Nilsson et al. (2011).

data. This approach could be useful also when visualising data. By replacing the mean, m_i, and sample standard deviation, s_i, in Eq. 3.5 with the weighted moving average MA_n^w and autocorrelation compensated sample standard deviation $\sqrt{1/\gamma} \cdot s_{\mathrm{MA}}$, cf. Eqs. 3.24 and 3.21 in Sections 3.5 and 3.3 respectively, the accuracy of the background estimate should improve in areas with large systematic variations. This should also improve the homogeneity of the deviation display in such areas.

4.2 Statistical inference

False positive tests

The false positive rate of the proposed test and it's two constituents: the S&D mid-p test on counts of pulses and the likelihood ratio test on spectral distribution, all show false positive rates close to the predefined rate, α, for all but the very lowest count rates. The reader is referred to Paper II for a complete presentation of the false positive rates (cf. Tables 1-3, Paper II).

Apart from the inherent problem with lack of information in discrete data for low count rates, one can also be concerned about the validity

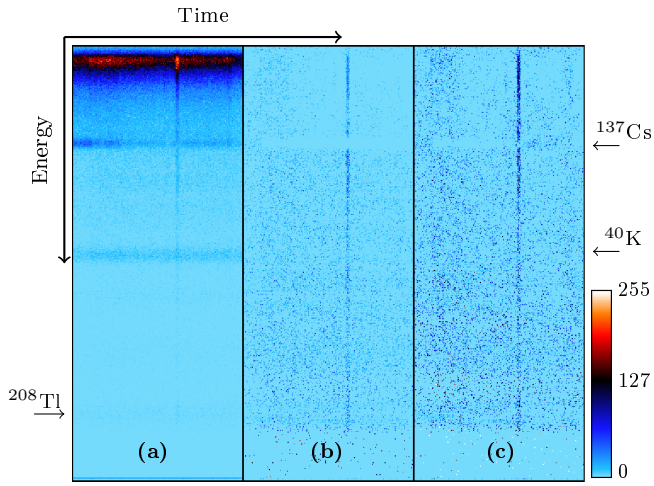

Figure 4.2: A ^{232}Th anomaly visualised by a waterfall plot (a) and deviation displays (b, c) using two different background sampling times: ∼300 s (a, b) and 50 s (c). Each display contains about 200 s of measurements. Note the improvement in visibility of the ^{232}Th signal at high energies in the deviation displays. Adapted from Paper I.

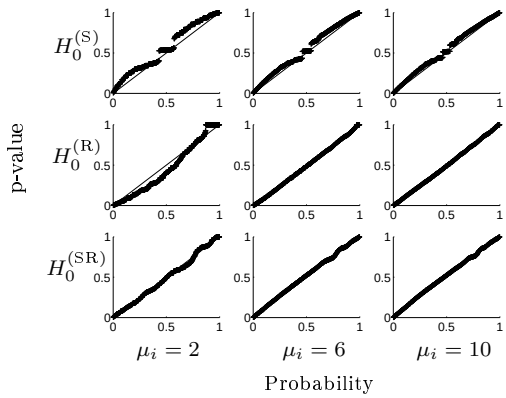

Figure 4.3: Probability versus p-values (x-marks) for the statistical tests constituting the proposed test ($k = 2$), using Poisson means: $\mu_i = \lambda_i = \{2, 6, 10\}$. Ideally, the p-values should fall on the line given by an $\mathcal{U}(0, 1)$ distribution (solid line). The distribution of p-values for the proposed test, testing for $H_0^{(SR)}$, shows good agreement with $\mathcal{U}(0, 1)$ in the lower tail, even at low count rates.

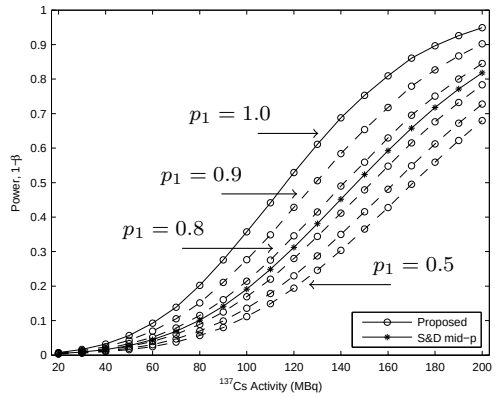

Figure 4.4: Power of the one-sided proposed test ($k = 2$) for different ^{137}Cs activities. The power of the proposed test depends on the validity of the assumed spectral distribution, here: $x_1/x > y_1/y$. p_1 is the probability of a detected ^{137}Cs pulse ending up in channel 1. The geometry and procedure of the test is described in Paper II, from which the figure was adapted.

of Wilks' χ^2-approximation of the log-likelihood ratio, Λ. As stated in Section 3.3, $\Lambda \to \chi^2(k-1)$ as the sample size $n \to +\infty$. However, and as shown in Fig. 4.3 for the special case $k = 2$, this concern seems unfounded. At least for $\mu_i = \lambda_i \geq 6$, as the p-value of the likelihood test is well described by an $\mathcal{U}(0,1)$ distribution.

Power tests

The power $(1-\beta)$ of the (one-sided) combined test for $H_0^{(\mathrm{S})}$ (counts of pulses) and $H_0^{(\mathrm{R})}$ (spectral distribution) for $k = 2$, as defined in Eqs. 3.8 and 3.19 in Section 3.3, can be seen in Fig. 4.4. In the same figure, the power of the test on counts of pulses (S&D mid-p) is also given, for comparison. From Fig. 4.4 it is clear that the proposed test potentially has greater power. However, the power of the combined test depends on the power of the test for $H_0^{(\mathrm{R})}$, which in turn ultimately depends on how uniformly the counts are distributed within the two channels.

Another example using the same procedure for power tests, described in detail in Section 3.2 in Paper II, but this time using ^{60}Co, is given in Fig. 4.5. The only difference is the linear attenuation coefficients for the two ^{60}Co primary photon energies, which are different from that of ^{137}Cs. The power curves given in Fig. 4.5 were evaluated for three channels ($k = 3$), which under $H_0^{(\mathrm{SR})}$ has equal mean count rates, and using the two-sided likelihood test, cf. Eq. 3.17 in Section 3.3. In this example $p_1 = 1$, which means that two of the channels were background channels.

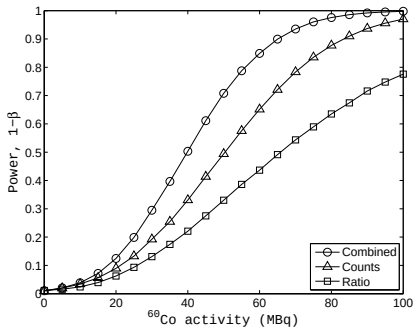

Figure 4.5: Power of the two-sided proposed test (circles) for different ^{60}Co activities. The power of the two-sided likelihood test (squares, $k = 3$) and mid-p version of S&D's test (triangles) are also given. α was set to 1 %. The procedure of the power test is described in detail in Paper II.

The key to maximise the power of the proposed test is to maximise the power of the test on spectral distribution. That is, to design the test so that most pulses from the actual source registers in one of the k bins. This effect can be seen in Fig. 4.4, where the test for $p_1 = 1$ yields the greatest power. Fig. 3.7 in Section 3.3 gives a good example of how this can be achieved in practice. The central channels are combined into a new bin and two background bins are defined on each side of the central bin. Given a reasonable resolution, the majority of counts should fall in the central bin (under H_1). Assuming that the there is no peak in the region for background-only data, as is the case for e.g. ^{60}Co, an approximately uniform spectral distribution can be expected. Hence, situations close to those presented in Figs. 4.4-4.5 ($p_1 \geq 0.8$) should arise.

Independent samples

The statistical tests described in Paper II assumes that the current sample x and the background sample y are independent. But in Paper IV we concluded that consecutive samples, measured in a gradient, can be expected to be autocorrelated. It may thus seem paradoxical that two samples, measured only seconds apart when the vehicle is stopped, are considered independent. But considering the random nature of radioactive decay, which is well described by a Poisson process, the independence of two samples taken from the same underlying (Poisson) distribution is no enigma. As soon as the vehicle starts moving and, more importantly, the radiation background changes, autocorrelation becomes a problem.

4.3 Ground-to-air comparisons

Backpack comparisons

The scatter plots shown in Fig. 4.6 were obtained using the field of view (FOV) correction, described in Section 3.4 and Paper III. The relationships between AGS and backpack data for most area/nuclide combinations are inconclusive. The exceptions are eU from Area II and eTh from Area III. Clearly, eU within Area II and eTh within Area III show a positive correlation, but most samples reside above the $y = x$ line. The AGS data exhibits greater variability than does the backpack data, an effect that possibly can be explained by the averaging of backpack data points in the FOV correction.

When combining all three areas, eU and eTh show a strong positive correlation with slope close to unity and intersection close to zero, cf. Fig. 4.7. The scattering of samples at low activity levels still shows a large spread, but this could also be expected since these samples have a net count close to zero, associated with a large stochastic uncertainty. By closer examination of Fig. 4.7 two clusters with different slopes, originating from different areas (Area II and III) can be observed. The normalised response of the backpack system is greater compared to that of the AGS system as the activity increases. This can be an effect of greater variability at the ground level. As the variability in activity increases, the averaging due to the FOV correction becomes less apparent.

Car-borne comparisons

One of the aims of Paper IV was to test if the good agreement between AGS and terrestrial data shown in Fig. 4.7 would still hold when replacing the backpack with a CGS system. Drawing from the results of Paper III, an area with large variations in the background radiation was identified. Comparisons of normalised eTh CGS and AGS data for routes I and II, cf. Fig. 3.12 in Section 3.5, are shown in Fig. 4.8. Although there are some discrepancies, mainly in the parts with lower eTh activity, the main features are in fairly good agreement. The figures show that if the eTh features are large enough to show up in the AGS data, the influence of the road on CGS data (which should lead to a bias) can be neglected.

It is unfeasible to use ground-to-air comparisons in areas with very low background activity or very small variability in the background activity. This can be seen by studying the comparisons within Area I and

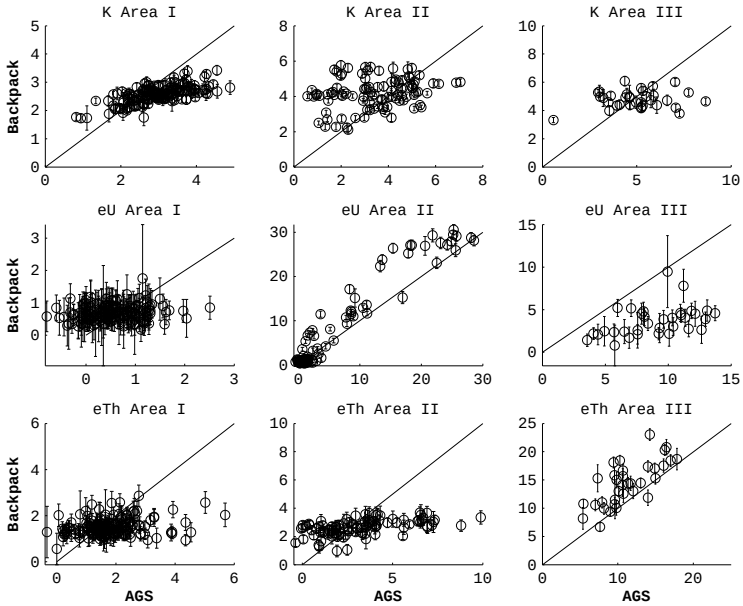

Figure 4.6: Normalised count rates of ^{40}K, eU and eTh respectively, for backpack system vs. AGS. The line $y = x$, corresponding to a perfect positive correlation, is also given in each subfigure, for comparison. Adapted from Paper III.

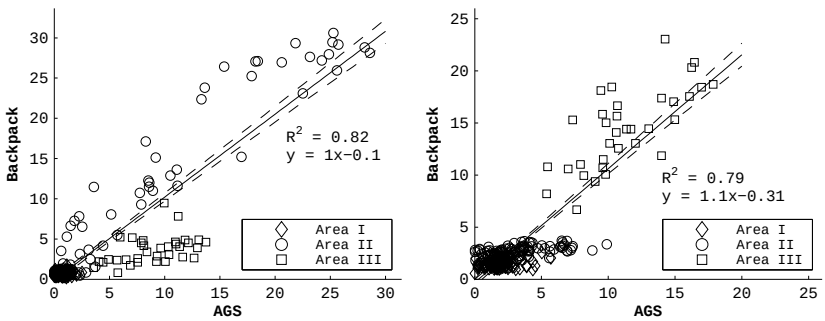

Figure 4.7: Scatter plots of eU (left) and eTh (right) for areas I-III with a linear best fit (least squares, solid line). The equations, R^2-values and 95 % confidence intervals (dashed lines) of the fit is also given. Adapted from Paper III.

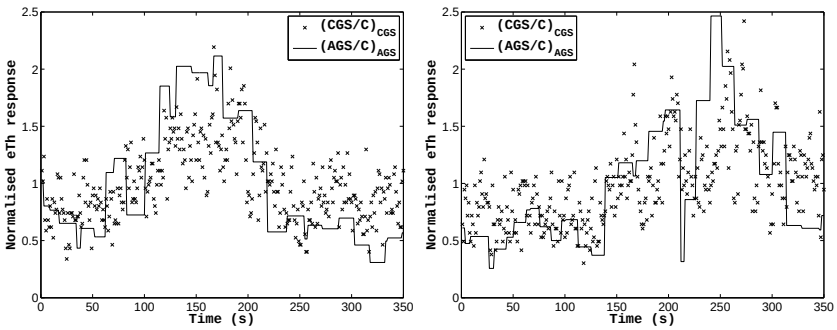

Figure 4.8: Normalised eTh CGS (x-marks) and AGS (sold line) responses along routes I (left) and II (right). Adapted from Paper IV.

the comparisons for ^{40}K in Fig. 4.6. The same result applies to car-borne data as well; while good agreements can be seen for the sections with gradients in Fig. 4.8, there are greater discrepancies in the low-activity sections at the beginning and end of each route.

4.4 Background radiation gradients

The step function derived from AGS eTh data, $f'(t)_{\mathrm{AGS}}$, for the two routes can be seen in Fig. 4.9 along with the normalised eTh CGS responses. To reduce the fluctuations in f'_{AGS} the AGS data was smoothed using a moving average of length 10. As can be seen in Fig. 4.9 the AGS first derivative approximation does not align perfectly with the CGS responses. Despite the discrepancies, f'_{AGS} still offers a rough prediction on the sign and slope of the background eTh gradients along the routes at the ground level.

Table 4.1 shows the number of false positives along routes I and II for the different MA-statistics. Assuming the counts were normally distributed, the results should equal α, which was 5 %. The lag of the average leads to inaccurate averages when using the unweigted moving average, MA_{40}, as can be seen in Fig. 4.10. Incorporating the systematic changes by using the weighted moving average, MA^{w}_{40}, improved the accuracy of the mean compared with MA_{40}. The reduction in the number of false positives was modest, but after correcting for autocorrelation, indicated in Table 4.1 with a superscript of γ, the overall results were quite acceptable for Detector system 3.

Due to the much smaller efficiency of Detector system 4, the eTh

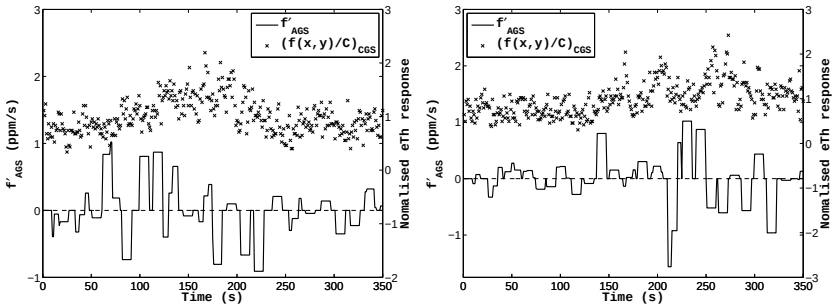

Figure 4.9: AGS step function, f'_{AGS}, (left axes) for eTh along routes I (left) and II (right). The normalised CGS eTh response is also given, for comparison (right axes). Adapted from Paper IV.

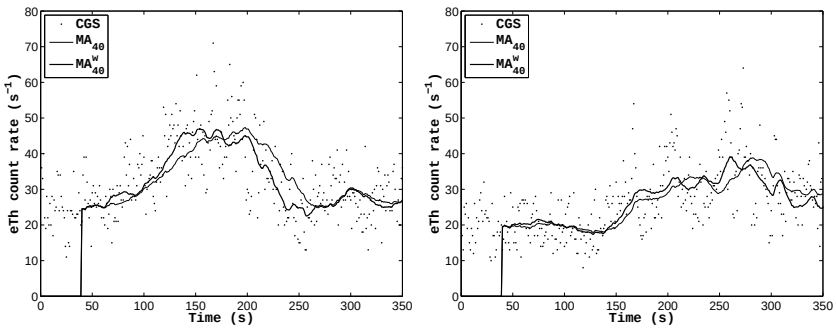

Figure 4.10: MA_{40} (thin line) and MA^{w}_{40} (thick line) for eTh along routes I (left) and II (right). The CGS count rate is also given, for comparison. Adapted from Paper IV.

gradients given by f'_{AGS} were instead used to weight the full spectrum counts. Table 4.1 gives the results from these tests as well. The use of weights leads to a slightly greater reduction in the number of false positives for the $LaBr_3$:Ce system. This can probably be attributed to the use of full spectrum counts rather than eTh primary counts, but overall the results are comparable to those of the larger Detector system 3.

No tests of the false negative rates or power were done in Paper IV, but when visually inspecting the response of the different MA-statistics along the two routes, shown in Fig. 4.10, it is clear that MA^{w} is lower than MA in the negative gradients. The conclusion would be that the

Table 4.1: Number of false positives, n_f, given in % along routes I and II for NaI(Tl) (Detector system 3) and $LaBr_3$:Ce (Detector system 4), using four of different MA statistics. The expected number of false positives for a 95 % prediction interval ($\alpha = 5\,\%$) using a sample size, n, of 312 is 15.6. Adapted from Paper IV.

	False positives			
	Route I ($n = 312$)		Route II ($n = 312$)	
	NaI(Tl)	$LaBr_3$:Ce	NaI(Tl)	$LaBr_3$:Ce
MA_{40}	6.4 ($n_f = 20$)	8.3 ($n_f = 26$)	7.1 ($n_f = 22$)	7.7 ($n_f = 24$)
MA_{40}^{γ}	5.8 ($n_f = 18$)	6.4 ($n_f = 20$)	5.8 ($n_f = 18$)	6.7 ($n_f = 21$)
MA_{40}^{w}	6.4 ($n_f = 20$)	5.8 ($n_f = 18$)	6.1 ($n_f = 19$)	5.5 ($n_f = 17$)
$MA_{40}^{w,\gamma}$	5.1 ($n_f = 16$)	4.5 ($n_f = 14$)	4.5 ($n_f = 14$)	4.2 ($n_f = 13$)

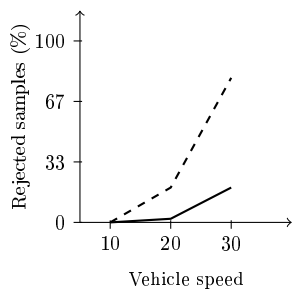

Figure 4.11: Microphonic noise samples from Detector system 1, in %, as a function of vehicle speed for the two mounting configurations: detector on the floor (dashed line) and detector in the dampener (solid line).

probability of detecting an orphan source is greater in these regions by using MA^{w}. Of course, in the positive gradients the false alarm rates were lower when using MA^{w}, at the expense of the false negative rates in these regions. But lower sensitivity in positive background radiation gradients is an acceptable price to pay in order to avoid excess false positives.

4.5 Microphonic noise

As shown in Paper V and as can be seen in Figs. 4.11-4.12, the microphonic noise of Detector system 1 increases with vehicle speed. The percentages of rejected events were 0, 19 and 79 % at 10, 20 and 30 km h^{-1}, respectively. The effect was less prominent when using the dampener: 0, 2 and 19 % at the same vehicle speeds. The induced noise grows exponentially, which is a good reason to keep vehicle speeds modest when driving on uneven roads. When considering all samples for each mount-

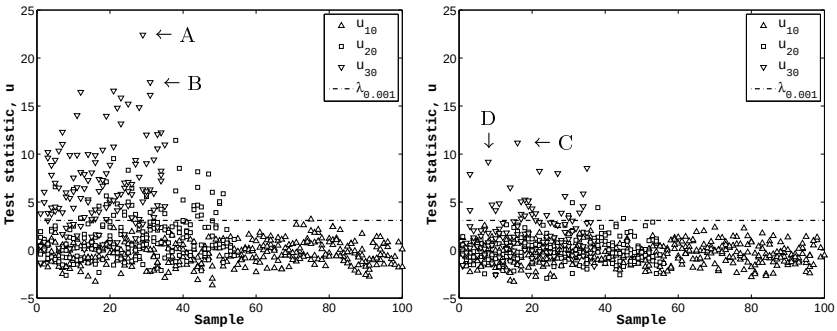

Figure 4.12: Samples above the dashed line ($p < 0.001$) contain microphonic noise. Detector mounted directly on the floor (left) and in the vibration dampener (right). Adapted from Paper V.

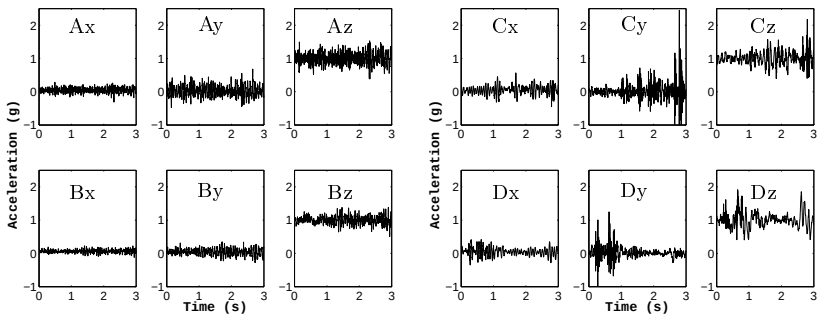

Figure 4.13: Accelerometer xyz-data for samples A-D, cf. Fig. 4.12. Adapted from Paper V.

ing configuration, the overall reduction of microphonic noise was 79 % when using the dampener.

The magnitudes of the vibrations alone cannot explain the induced microphonic noise. In the accelerometer data included in Fig. 4.13, the accelerations recorded when using the dampener (C and D) are at least as severe as the samples recorded with no dampener (A and B). Rather, the fast ripples seen in all directions in the samples without dampener (A and B) seem to be the cause. This explanation is confirmed by the Fourier transform analysis, shown in Fig. 4.14, where a shift towards lower vibration frequencies is observed when using the dampener.

To assess the effects of microphonic noise on the FWHM and full energy peak efficiency (FEPE), the FWHM of the ^{40}K, ^{214}Bi and ^{208}Tl

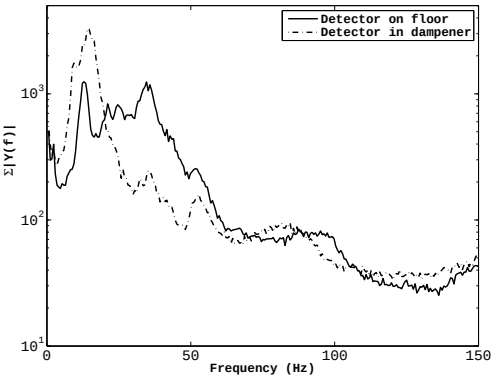

Figure 4.14: Sum of single sided Fast Fourier Transform (FFT) amplitudes of all vibration measurements in the z-direction (up and down) conducted at 30 km h^{-1} for both mounting configurations. When the detector is mounted in the vibration dampener configuration a frequency shift towards lower frequencies is observed. Adapted from Paper V.

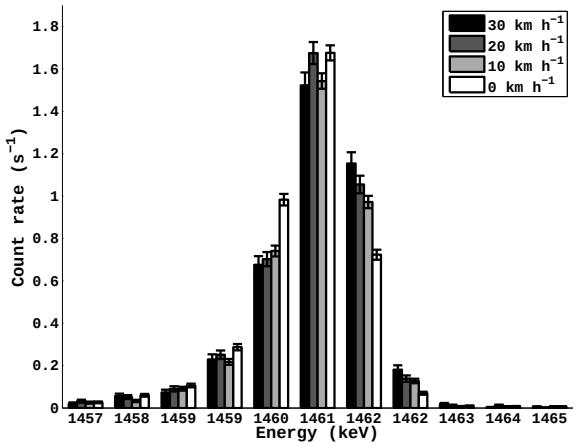

Figure 4.15: Mean count rates (s^{-1}) in the ^{40}K region with standard errors for four different vehicle speeds without dampener. The energy bins are rounded to nearest integer.

peaks along with the count rates in the ^{40}K region were studied at different vehicle speeds. With the detector mounted directly on the floor, the changes in FWHM, ΔFWHM, relative to the value of the background measurements (at 0 km h^{-1}, $FWHM_0$) are listed in Table 4.2. The FWHM, and hence the resolution of the system, degrades as soon as the vehicle starts moving. The worst resolutions were measured at 30 km h^{-1}, where ΔFWHM-values of 10-19 % were observed. Figure 4.15 shows the total count rates in the ^{40}K peak region at different vehicle speeds. Even when summing all channels and comparing the results, no evidence was found of lower FEPE. The mean total dead time of the system was also analysed with the same result; the microphonic pulses do not seem to paralyse the electronics of the detector system.

Table 4.2: ΔFWHM (%) relative to 0 km/h ($FWHM_0$) of different peaks for Detector system 1 at different vehicle speeds. Uncertainties assume a Gaussian peak shape.

			ΔFWHM (%)		
	Energy (keV)	$FWHM_0$ (keV)	10 km/h	20 km/h	30 km/h
^{40}K	1461	2.68 ± 0.03	5.3 ± 1.5	0.5 ± 1.7	10.3 ± 2.0
^{214}Bi	1765	2.98 ± 0.11	13.8 ± 6.1	10.2 ± 7.7	18.7 ± 9.0
^{208}Tl	2614	3.09 ± 0.08	11.7 ± 3.8	9.8 ± 4.5	19.4 ± 5.3

It is difficult to draw any general conclusions from the observations presented in Paper V, which is a case study. For example, a frequency shift may not always occur for other detector systems, roads or mounting configurations. To further explore the phenomena and to find ways to reduce the microphonic noise for a given detector system one could use the statistical test described in Section 3.6 in an environment where the vibrations are under control. Possible resonance frequencies of the detector system would then be of particular interest. Another interesting approach would be to analyse the vibration characteristics of the vehicle. Knowledge of the vehicle's vibrations could then be valuable in the design of an effective detector mounting system.

Chapter 5

Major conclusions

The use of airborne gamma-ray spectrometry to account for gradients in the natural background radiation can reduce the number of false alarms when using terrestrial gamma surveys to search for orphan sources in areas with a systematic variability. However, ground-to-air comparisons are not feasible for areas with low background activity or low activity variability. For such areas, even spatially close measurements can be considered approximately random so that Poisson statistics can be directly applied. Using a test combining a Poisson model for counts of pulses with a likelihood test of the observed pulse distribution can increase the probability of detecting an orphan source.

The major conclusions of each paper were as follows:

I. A method for data visualisation which enhances positive deviations was presented. The method yields satisfactory results over the full energy range both for high- and low resolution spectrometers when used in different background radiation environments.

II. Most of the statistical tests found in the literature focus solely on counts of pulses from a radioactive sample. Inclusion of a test on the spectral distribution of the detected pulses can increase the power of the combined test without introducing additional false positives or unacceptable algorithm complexities.

III. Comparisons of terrestrial and airborne background surveys for three characteristic areas showed a positive correlation between

the two, provided that the area exhibits sufficient variability in activity. The statistical distributions were also shown to be similar between the two measurement techniques; most areas could be described by normal distributions.

IV. Airborne surveys can be used at the ground level to account for background radiation gradients. Using a weighted moving average, with weights derived from the step function of the airborne data, reduced the number of excess false positives due to positive gradients. Correcting for autocorrelation further improved the false positive rates.

V. Microphonic noise caused by vibrations can be a problem when using HPGe detectors in mobile gamma-ray spectrometry. The noise, appearing as pulses in the low energy region, increases exponentially with the speed of the vehicle. Much of the induced noise may be averted by mounting the detector in a shock-absorbing environment.

Acknowledgements

Thanks to:

- My supervisors:
  - Christer Samuelsson for introducing me to the field of radiation physics, the patience, humour and the open door
  - Christopher Rääf for the warm welcome in Malmö, the time and the excellent scientific advice
- Co-authors:
  - Karl Östlund for the many discussions and Friday humour
  - Jonas Nilsson, my sounding board in the world of bits and bytes
  - Jan Lanke, Department of Statistics, for sharing your vast knowledge
  - Robert Finck, SSM, for the support at all levels
- Former and new colleagues in the environmental radiology group:
  - Ünal, Hanna, Mats, Kurt, Gertie, Christian, Therése, Maria, Mikael H., Ylva, Fredrik H., Sören and Elis
- Former and new colleagues at the Departments in Lund and Malmö:
  - Martin, Magnus, Daniel, Marcus, Marie, Erik, Kristoffer, Fredrik N., Pernilla, David, Mattias, Lars *et al.*
- All members of the national emergency preparedness organisation I've met through the years
- South Skåne Regiment, P7, for your hospitality in letting me conduct many of my experiments at the beautiful fields of Revingehed

- Erik Hedström for the LaTeX-template and Markus Nilsson for the tips & tricks
- My friends, old and new
- My family for your love
- Dream Theater for the music

This PhD study was funded by a grant from the Swedish Radiation Safety Authority

Bibliography

Aage, H.K. and Korsbech, U. (2003), Search for lost or orphan radioactive sources based on NaI gamma spectrometry. *Appl. Radiat. Isotopes*, 58(1); pp. 103–113

Abramowitz, M. and Stegun, I. (1972), *Handbook of mathematical functions*. New York: Dover, 10th edn.

Agresti, A. and Gottard, A. (2005), Comment: Randomized confidence intervals and the mid-p approach. *Stat. Sci.*, 20(4); pp. 367–371

Agresti, A. and Gottard, A. (2007), Nonconservative exact small-sample inference for discrete data. *Comput. Stat. Data. An.*, 51(12); pp. 6447–6458

Baker, S. and Cousins, R.D. (1984), Clarification of the use of chi-square and likelihood functions in fits to histograms. *Nucl. Instrum. Meth. A*, 221(2); pp. 437–442

Barlow, R.J. (1989), *Statistics: A guide to the use of statistical methods in the physical sciences*. New York: John Wiley & Sons Ltd., 1st edn.

Beck, H.L., DeCampo, J. and Gogolak, C. (1972), *In situ Ge(Li) and NaI(Tl) gamma-ray spectrometry*. USAEC report HASL-258

Bernhardsson, C., Zvonova, I., Raaf, C. and Mattsson, S. (2011), Measurements of long-term external and internal radiation exposure of inhabitants of some villages of the Bryansk region of Russia after the Chernobyl accident. *Sci. Total. Environ.*, 409(22); pp. 4811–4817

Berry, G. and Armitage, P. (1995), Mid-p confidence intervals: a brief review. *The Statistician*, 44(4); pp. 417–423

Blom, G. (1984), *Sannolikhetsteori med tillämpningar* (in swedish). Lund: Studentlitteratur, 2nd edn.

Boson, J., Lidström, K., Nylén, T., Ågren, G. and Johansson, L. (2006), In situ gamma-ray spectrometry for environmental monitoring: a semi-empirical calibration method. *Radiat. Prot. Dosim.*, 121(3); pp. 310–316

Box, G.E.P. and Jenkins, G.M. (1976), *Time series analysis: forecasting and control*. San Francisco: Holden-Day

Bristow, Q. (1983), Airborne γ-ray spectrometry in uranium exploration. principles and current practice. *Int. J. Appl. Radiat. Isot.*, 34(1); pp. 199–229

Campi, F. and Porta, A.A. (2005), Sensitivity tests and risk evaluation for steelworks portal systems. *Radiat. Meas.*, 39; pp. 161–173

Chu, S.Y.F, Ekström, L.P. and Firestone, R.B (1999), *WWW Table of Radioactive Isotopes*. Version 2.0, Feb 1999. http://nucleardata.nuclear.lu.se/nucleardata/toi

Cousins, R.D., Linnemann, J.T. and Tucker, J. (2008), Evaluation of three methods for calculating statistical significance when incorporating a systematic uncertainty into a test of the background-only hypothesis for a poisson process. *Nucl. Instrum. Meth. A*, 595(2); pp. 480–501

Cousins, R.D., Hymes, K.E. and Tucker, J. (2010), Frequentist evaluation of intervals estimated for a binomial parameter and for the ratio of poisson means. *Nucl. Instrum. Meth. A*, 612(2); pp. 388–398

Cressie, N. and Read, T.R.C. (1989), Pearson's χ^2 and the loglikelihood ratio statistic G^2: A comparative review. *Int. Stat. Review*, 57(1); pp. 19–43

Cresswell, A.J. and Sanderson, D.C.W. (2009), The use of difference spectra with a filtered rolling average background in mobile gamma spectrometry measurements. *Nucl. Instrum. Meth. A*, 607(3); pp. 685–694

Cresswell, A.J., Sanderson, D.C.W. and White, D.C. (2006), Cs-137 measurement uncertainties and detection limits for airborne gamma spectrometry (AGS) data analysed using a spectral windows method. *Appl. Radiat. Isotopes*, 64(2); pp. 247–253

Currie, L.A. (1968), Limits from qualitative detection and quantitative determination. *Anal. Chem.*, 40(3); pp. 586–593

Currie, L.A. (1999), Detection and quantification limits: origins and historical overview. *Anal. Chim. Acta.*, 391; pp. 127–134

Demény, O., Méray, L., Somlai, J., Bodnár, R. and Révay, Zs. (2002), A new gamma spectral analysis algorithm for the determination of the origin of ^{137}Cs contamination. *J. Radioanal. Nucl. Ch.*, 254(2); pp. 311–314

Dixon, W.J. and Massey, F.J. (1957), *Introduction to statistical analysis*. New York: McGraw-Hill, 2nd edn.

Dowdall, M., Andersson, K. G., Pálsson, S. E. and Sidhu, R. Singh (2010a), Malevolent use of radioactive materials: An international exercise in the analysis of gamma-spectrometric data. *Appl. Radiat. Isotopes*, 68(9); pp. 1789–1797

Dowdall, M., Selnæs, Ø., Standring, W., Nielsen, S., del Risco Norrlid, L., Pálsson, S., Renvall, T. and Sidhu, R. Singh (2010b), An emergency response intercomparison exercise using a synthetically generated gamma-ray spectrum. *J. Radioanal. Nucl. Ch.*, 283; pp. 31–43

Dowdall, M., Smethurst, M.A., Watson, R., Mauring, A., Aage, H.K., Andersson, K.G. and Pálsson, S.E. (2012), Car-borne gamma spectrometry: a virtual exercise in emergency response. *J. Environ. Radioactiv.*, 107; pp. 68–77

Duftschmid, K.E. (2002), Over the border - The problems of uncontrolled radioactive materials crossing national borders. *J. Radiol. Prot.*, 22; pp. 31–43

Finck, R. and Ulvsand, T. (2003), Search for orphan gamma radiation sources, experiences from the barents rescue 2001 execise. In: *Proceedings, Security of Radioactive Sources held at IAEA, Vienna, Austria, 10-13 March 2003*, pp. 123–137

Finck, R., Johansson, J., Persson, B.Å., C., Samuelsson and Östlund, K. (2008), Close reality in radiological emergency exercises. In: *Proceedings of the 12th Congress of the International Radiation Protection Association (IRPA), October 19-24, 2006, Buenos Aires, Argentina*

Finck, R.R. (1992), *High resolution field gamma spectrometry and its applications to problems in environmental radiology.* Ph.D. thesis, Lund University, Malmö and Lund, Sweden

Fisher, R. A. (1932), *Statistical methods for research workers.* London: Oliver and Boyd, 4th edn.

Fisher, R. A. (1948), Questions and answers #14. *Am. Stat.*, 4(2); p. 30

Franklin, A. (2002), William Wilson and the absorption of beta rays. *Phys. perspect.*, 4; pp. 40–77

Geelhood, B.D., Ely, J.H., Hansen, R.R., Kouzes, R.T., Schweppe, J.E. and Warner, R.A. (2004), Overview of portal monitoring at border crossings. In: Metzler, S.D. (Ed.), *2003 IEEE Nuclear Science Symposium, Conference record, vols 1-5*, IEEE; Nucl & Plasma Sci Soc, pp. 513–517, IEEE Nuclear Science Symposium/Medical Imaging Conference, Portland, OR, Oct 19-25, 2003

Gerward, L. (1999), Paul Villard and his discovery of gamma rays. *Phys. perspect.*, 1; pp. 367–383

Gilmore, G. (2008), *Practical gamma-ray spectrometry*. Weinheim: Wiley-VCH Verlag, 2nd edn.

Grasty, R.L. (1995), Environmental monitoring by airborne gamma ray spectrometry, experience at the Geological Survey of Canada. In: *IAEA-TECDOC-827*, Vienna, Austria, pp. 93–101

Grasty, R.L. and Cox, J.R. (1997), A carborne gamma-ray spectrometer system for natural radioactivity mapping and environmental monitoring. In: Hovgaard, J. (Ed.), *Rapid Environmental Surveying Using Mobile Equipment*, Copenhagen: Nordic Nuclear Safety Research, pp. 71–90

GSL (2011), *GNU Scientific Library, v. 1-15*. www.gnu.org/software/gsl

Hjerpe, T. (2004), *On-line mobile in-situ Gamma spectrometry*. Ph.D. thesis, Lund University, Lund, Sweden

Hjerpe, T. and Samuelsson, C. (2003), A comparison between gross and net count methods when searching for orphan radioactive sources. *Health Phys.*, 84(2); pp. 203–211

Hjerpe, T., Finck, R.R. and Samuelsson, C. (2001), Statistical data evaluation in mobile gamma spectrometry: An optimization of on-line search strategies in the scenario of lost point sources. *Health Phys.*, 80(6); pp. 563–570

Hovgaard, J. (1997), *Airborne gamma-ray spectrometry: statistical analysis of airborne gamma-ray spectra*. Ph.D. thesis, Technical University of Denmark, DTU

Hovgaard, J., Toivonen, H., Multala, J., Mellander, H., Jensen, J. and Koivukoski, J. (Eds.) (1997), *RESUME-95: Rapid Environmental Surveying Using Mobile Equipment, Report NKS RESUME 95, Copenhagen*

HPS, Health Physics Society (1996), *Performance criteria for radiobioassay. An American National Standard. ANSI/HPS N13.30-1996*. American National Standards Institute, New York, USA

Hubbell, J.H. and Seltzer, S.M. (2004), *Tables of x-ray mass attenuation coefficients and mass energy-absorption coefficients (version 1.4)*. National Institute of Standards and Technology (NIST), Gaithersburg, MD, USA

IAEA (1991), *IAEA Technical Report Series 323, Airborne gamma ray spectrometer surveying*. International Atomic Energy Agency (IAEA), Vienna, Austria

IAEA (1993), *The radiological accident in Soreq*. International Atomic Energy Agency (IAEA), Vienna, Austria

IAEA (1995), *IAEA-TECDOC-827, Application of uranium exploration data and techniques in environmental studies*. International Atomic Energy Agency (IAEA), Vienna, Austria

IAEA (1996), *The radiological accident at the irradiation facility in Nesvizh*. International Atomic Energy Agency (IAEA), Vienna, Austria

IAEA (1998), *The radiological accident in Tammiku*. International Atomic Energy Agency (IAEA), Vienna, Austria

IAEA (2000a), *The radiological accident in Istanbul*. International Atomic Energy Agency (IAEA), Vienna, Austria

IAEA (2000b), *The radiological accident in Yanango*. International Atomic Energy Agency (IAEA), Vienna, Austria

IAEA (2002a), *The radiological accident in Gilan*. International Atomic Energy Agency (IAEA), Vienna, Austria

IAEA (2002b), *The radiological accident in Samut Prakarn*. International Atomic Energy Agency (IAEA), Vienna, Austria

IAEA (2003), *IAEA-TECDOC-1344, Categorization of radioactive sources, Revision of IAEA-TECDOC-1191, Categorization of radiation sources*. International Atomic Energy Agency (IAEA), Vienna, Austria

IAEA (2004), *The radiological accident in Cochabamba*. International Atomic Energy Agency (IAEA), Vienna, Austria

ICRU (1994), *Gamma-ray spectrometry in the environment, ICRU report 53*. International Committee on Radiological Units and Measurements (ICRU), Bethesda, MD, USA

ICRU (2006), *Sampling for radionuclides in the environment, ICRU report 75*. International Committee on Radiological Units and Measurements (ICRU), Oxford University Press

Keich, U. and Nagarajan, N. (2006), A fast and numerically robust method for exact multinomial goodness-of-fit test. *J. Comput. Graph. Stat.*, 15(4); pp. 779–802

Kocher, D.C. and Sjoreen, A.L. (1985), Dose-rate conversion factors for external exposure to photon emitters in soil. *Health Phys.*, 48(2); pp. 193–205

Kock, P. (2012), *Deconvoluting the internal contamination of the $LaBr_3$:Ce crystal.* International Radiation Protection Association (IRPA), poster presentation, 13th IRPA Congress, 13-18 May 2012, Glasgow, Scotland

Lancaster, H.O. (1961), Significance tests in discrete distributions. *J. Am. Stat. Assoc.*, 56(294); pp. 223–234

Lavi, N., Groppi, F. and Alfassi, Z.B. (2004), On the measurement of ^{40}K in natural synthetic materials by the method of high-resolution gamma-ray spectrometry. *J. Environ. Radioactiv.*, 38; pp. 139–143

Lidström, K and Nylén, T. (1998), *Beredskapsmetoder för mätning av radioaktivt nedfall (in swedish).* FOA-R–98-00956-861–SE, FOA, Umeå, Sweden

Martin, P., Timis, S., McGill, A., Ryan, B. and Pfitzner, K. (2006), Use of airborne γ-ray spectrometry for environmental assessment of the rehabilitated Nabarlek uranium mine, Australia. *Environ. Monit. Assess.*, 116; pp. 531–553

Martin-Burtart, N., Guillot, L. and Nourreddine, A.-M. (2012), Airborne spectrometry: Extraction of low energy γ-rays using two or three spectral windows. *Appl. Radiat. Isotopes*, 70(8); pp. 1784–1791

Mellander, S.H. (1988), *Airborne gammaspectrometric measurements of the fall-out over Sweden after the nuclear reactor accident in Chernobyl, USSR.* Report TFRAP 8803 Swedish Geological Co., Uppsala, Sweden

Méray, L (1994), Deconvolution of nuclear spectra of low counts. *Nucl. Instrum. Meth. A*, 353(1-3); pp. 272–275

Méray, L. and Demény, O. (2001), Detection limit and decision thresholds in spectrometry. *Appl. Spectrosc.*, 55(8); pp. 1102–1108

Minty, B.R.S. (1997), Fundamentals of airborne gamma-ray spectrometry. *AGSO J. Aust. Geol. Geophys.*, 17(2); pp. 39–50

Morales, J., Garcia, E., Ortiz de Solorzano, A., Morales, A., Nuñez-Lagos, R., Puimedon, J., Saenz, C. and Villar, J.A. (1992), Filtering microphonics in dark matter germanium experiments. *Nucl. Intrum. Meth. A*, 321(1-2); pp. 410–414

Nagarajan, N., Jones, N. and Keich, U. (2005), Computing the P-value of the information content from an alignment of multiple sequences. *Bioinformatics*, 21(suppl 1); pp. 311–318

Nicolini, R., Camera, F., Blasi, N., Brambilla, S., Bassini, R., Boiano, C., Bracco, A., Crespi, F. C. L., Wieland, O., Benzoni, G., Leoni, S., Million, B., Montanari, D. and Zalite, A. (2007), Investigation of the properties of

a 1 " x 1 " LaBr3 : Ce scintillator. *Nucl. Intrum. Meth. A*, 582(2); pp. 554–561

Nilsson, J., Finck, R., Kock, P. and Samuelsson, C. (2011), *Using the $LaBr_3$:Ce scintillation detector for mobile γ-spectrometry.* Nordic society for radiation protection (NSFS), poster presentation (S8-P7), NSFS-2011 Conference, 22-25 Aug 2011, Reykjavik, Iceland

Nobelstiftelsen (1965), *Nobel lectures, including presentation speeches and Laureates' biographies.* Singapore: World Scientific

Pujol, Ll, Gonzalez-Gonzalez, J. A. and Suarez-Navarro, M. J. (2011), Application of a pedestrian portal monitor at Madrid International Airport in Spain. *Radiat. Meas.*, 46(4); pp. 451–456

Quayle, D., Ungar, K., Hoffman, I. and Korpach, E. (2010), Developments in radiological-nuclear support to security through the Canadian CBRNE Research and Technology Initiative (CTRI). In: *IRPA 2010 Proceedings*, International Radiation Protection Association (IRPA), pp. 1766–1771, Third European IRPA Congress, 14-18 June 2010, Helsinki, Finland

Sanderson, D.C.W. and Ferguson, J.M. (1997), The European capability for environmental airborne gamma ray spectrometry. *Radiat. Prot. Dosim.*, 73(1-4); pp. 213–218

Sanderson, D.C.W., Allyson, J. D., McConville, P., Murphy, S. and Smith, J. (1997), Airborne gamma ray measurements conducted during an international trial in Finland. In: Hovgaard, J. (Ed.), *Rapid Environmental Surveying Using Mobile Equipment*, Copenhagen: Nordic Nuclear Safety Research, pp. 235–254

Sanderson, D.C.W., Cresswell, A.J., Scott, E.M., Lauritzen, B., Karlsson, S., Strobl, C., Karlberg, O. and Lang, J.J (2003), Report on exercise data comparisons. In: *An international comparison of airborne and ground based gamma ray spectrometry*, Glasgow, Scotland, UK: Univeristy of Glasgow, pp. 9–174

Sanderson, D.C.W., McLeod, J.J. and Ferguson, J.M. (2001), A European bibliography on airborne gamma-ray spectrometry. *J. Environ. Radioactiv.*, 53(3); pp. 411–422

Shepard, D. (1968), A two-dimensional interpolation function for irregularly-spaced data. In: *Proceedings of the 1968 23rd ACM national conference*, pp. 517–524

Shumway, R.H. and Stoffer, D.S. (2011), *Time series analysis and its applications with R examples.* New York: Springer

Simmons, J.G (1996), *The scientific 100: A ranking of the most influential scientists, past and present.* New York: Citadel Press

Strom, D.J. and MacLellan, J.A. (2001), Evaluation of eight decision rules for low-level radioactivity counting. *Health Phys.*, 81(1); pp. 27–34

Sumerling, T.J. and Darby, S.C. (1981), *Statistical aspects of the interpretation of counting experiments designed to detect low levels of radioactivity.* National Radiological Protection Board (NRPB); NRPB-R113, Chilton, UK

Takoudis, G., Xanthos, S., Clouvas, A. and Potiriadis, C. (2010), Determining minimum alarm activities of orphan sources in scrap loads; Monte Carlo simulations, validated with measurements. *Nucl. Instrum. Meth. A*, 614(1); pp. 57–67

Tewari, S.G., Nagaraja, K.N. and Surya Kumar, N.V. (1988), Data enhancement techniques for airborne gamma ray spectrometric data. In: *IAEA-TECDOC-472*, Vienna, Austria, pp. 87–116

Tyler, Andrew N. (2008), In situ and airborne gamma-ray spectrometry. In: Povinec, Pavel P. (Ed.), *Analysis of environmental radionuclides*, *Radioactivity in the environment*, vol. 11, Elsevier, pp. 407 – 448

Ulvsand, T., Finck, R.R. and Lauritzen, B. (Eds.) (2002), *NKS/SRV seminar on Barents Rescue 2001 LIVEX gamma search cell*, vol. NKS-54. Roskilde, Denmark: NKS Secretariat

UNSCEAR (2000), *Sources and effects of ionizing radiation, volume 1: sources.* United Nations Scientific Committee of the Effects of Atomic Radiation (UNSCEAR), New York, USA

Walpole, R. E., Myers, R. H., Myers, S. L. and Ye, K. (2002), *Probability & statistics for engineers & scientists.* Upper Saddle River: Prentice Hall, 7th edn.

WHO (2009), *WHO handbook on indoor radon: a public health perspective.* World Health Organization (WHO), Geneva, Switzerland

Wilks, S.S. (1938), The large-sample distribution of the likelihood ratio for testing composite hypotheses. *Ann. Math. Stat.*, 9; pp. 60–62

Yoshida, N. and Kanda, J. (2012), Tracking the Fukushima Radionuclides. *Science*, 336(6085); pp. 1115–1116

Zhang, Y., Xiong, S. and Chen, T. (1998), Application of airborne gamma-ray spectrometry to geoscience in China. *Appl. Radiat. Isotopes*, 49(1-2); pp. 139–146

Åkerblom, G. (1995), The use of airborne radiometric and exploration survey data and techniques in radon risk mapping in Sweden. In: *IAEA-TECDOC-827*, Vienna, Austria, pp. 159–180

Östlund, K, Finck, R. and C., Samuelsson (2010), Radiological emergency exercises facing the collaboration issue of different response authorities. In: *IRPA 2010 Proceedings*, International Radiation Protection Association (IRPA), pp. 1253–1262, Third European IRPA Congress, 14-18 June 2010, Helsinki, Finland

Papers I–V

Paper I

Applied Radiation and Isotopes 68 (2010) 1832–1838

Contents lists available at ScienceDirect

Applied Radiation and Isotopes

journal homepage: www.elsevier.com/locate/apradiso

A deviation display method for visualising data in mobile gamma-ray spectrometry

Peder Kock [a,*], Robert R. Finck [b], Jonas M.C. Nilsson [a], Karl Östlund [a], Christer Samuelsson [a]

[a] Department of Medical Radiation Physics, Clinical Sciences, Lund University, University Hospital, SE-221 85 Lund, Sweden
[b] Swedish Radiation Protection Authority, SE-171 16 Stockholm, Sweden

ARTICLE INFO

Article history:
Received 4 September 2009
Received in revised form
1 February 2010
Accepted 1 April 2010

Keywords:
Mobile gamma spectrometry
Radioactive source search
Orphan sources
Data visualisation

ABSTRACT

A real time visualisation method, to be used in mobile gamma-spectrometric search operations using standard detector systems is presented. The new method, called deviation display, uses a modified waterfall display to present relative changes in spectral data over energy and time. Using unshielded ^{137}Cs and ^{241}Am point sources and different natural background environments, the behaviour of the deviation displays is demonstrated and analysed for two standard detector types (NaI(Tl) and HPGe). The deviation display enhances positive significant changes while suppressing the natural background fluctuations. After an initialisation time of about 10 min this technique leads to a homogeneous display dominated by the background colour, where even small changes in spectral data are easy to discover. As this paper shows, the deviation display method works well for all tested gamma energies and natural background radiation levels and with both tested detector systems.

1. Introduction

Many tasks in the field of emergency preparedness calls for mobile gamma-ray detecting systems. When searching for orphan sources (IAEA, 2004) or mapping contaminated areas the search areas can be vaguely defined and vast. The pre-knowledge of source conditions, for instance, may range from none to almost complete information on source geometry, radionuclide identity and activity. Irrespective of whether air- or carborne, the search crew needs some guidance when interpreting the signal from the detector. The objective of this paper is to describe one such guidance method for visualising significant changes in the field of view of the detector.

Considering carborne platforms alone, the common recipe for mobile detecting systems is one or several large volume gamma-ray detectors, repeated short-term measurements and not too slow vehicle velocities. The detector platform itself needs special-designed computer software that deals with the constant information flow from the detector, positioning system and additional devices. Often, the Graphical User Interface (GUI) of such a program displays a wide range of user-defined parameters and graphs in real time. From simple parameters like intensity levels of specific radionuclides (Mellander, 1998) or potassium-stripped counts (PSC) in a region of interest (Hjerpe and Samuelsson, 2003) via simple displays like the "waterfall" display (see "rainbow method" in Aage and Korsbech, 2003), to more complex filtered displays (Cresswell and Sanderson, 2009) and imaging routines (Ziock et al., 2003, 2007). Many methods implemented in such programs have pre-defined alarm levels on different parameters, helping the search crew with indication. Alarms are, however, not within the scope of this paper.

The largest challenge when interpreting mobile gamma spectrometric information is the ever-changing radiation background. Ideally, both systematic changes and stochastic fluctuations in the photon field must be taken into account in order to achieve a sensitive and at the same time reliable search method. While stochastic fluctuations can be dealt with using statistical methods, incorporation of systematic changes into the search method is difficult and requires some knowledge *a priori*.

This paper describes a method to construct a straightforward and informative display—the *deviation display* (DD)—that enhances positive changes in spectral data. One purpose of this work was to construct a detector-independent method to display data in real time. This means that the deviation display should be suitable for all energies, both scintillator- and semiconductor-systems and at all naturally occurring levels of radiation. The method works with real time data and the deviation display functions both as a search tool and as an overview of background radiation trends. Consequently, this method could improve the search effort when searching for gamma-emitting sources using mobile platforms.

2. Theory and methods

The signal processing problems present in mobile gamma spectrometry are virtually the same as in other fields of digital

* Corresponding author. Fax: +46 46 127 249.
E-mail address: Peder.Kock@med.lu.se (P. Kock).

0969-8043/$ - see front matter © 2010 Elsevier Ltd. All rights reserved.
doi:10.1016/j.apradiso.2010.04.004

signal processing. Commercially available software, like MATLAB,[1] offers a large set of tool kits for processing and presentation of digital data. One of the functions found in MATLAB is the waterfall window display. Conventional waterfall displays present consecutive colour-scaled data arrays side by side as seen from above. Individual bins within each array are mapped on a colour range consisting of contrasting colours. After each data acquisition the measured data is added as a coloured line to the display, making it flow with time (for a brief description see Aage and Korsbech, 2003 or the MATLAB user manual).

2.1. The deviation display method

The proposed deviation display method is based on relative comparisons on a channel-by-channel basis. Let $m_{i,j}$ be the mean count rate (s^{-1}) in channel i after j measurements

$$m_{i,j} = m_{i,j-1} + \frac{c_{i,j} - m_{i,j-1}}{j} \quad (1)$$

where $c_{i,j}$ is the observed count rate using the same notation. The observed counts per time unit in channel i fluctuates about its mean with a sample standard deviation of

$$s_{i,j} = \sqrt{\frac{1}{j-1}\sum_{k=1}^{j}(c_{i,k} - m_{i,j})^2} \quad (2)$$

The dimensionless standard Z score, as computed by Tewari et al. (1988), can then be used to find anomalous regions in the spectral data

$$Z_{i,j} = \frac{c_{i,j} - m_{i,j}}{s_{i,j}} \quad (3)$$

Here, a modified version of the Z score statistic is used. Let $q_{i,j}$ be the relative deviation from the mean plus n standard deviations.

$$q_{i,j} = \max\left\{0, \frac{c_{i,j} - (m_{i,j-1} + n \cdot s_{i,j-1})}{n \cdot s_{i,j-1}}\right\} \quad (4)$$

The observed jth count rate is thus put in relation to the expected count rate based on the latest $j-1$ observations for that channel. For each sampled spectra j, the vector $\mathbf{q}_j = [q_{1,j}, q_{2,j}, \ldots, q_{nj}]^T$ is calculated. All negative elements in $\mathbf{q}_j$ are set to zero in order to enhance positive changes in the count rate. By storing the historical maximum positive deviation, q_{max}, a relative deviation can be calculated. Using a colour scheme of C colours each $q_{i,j}$ is colour-coded, i.e. mapped in the range [0,C] by scalar multiplication.

$$\mathbf{w} = \frac{C}{q_{max}} \cdot \mathbf{q} \quad (5)$$

The weighted vector $\mathbf{w}$ represents a new column in the deviation display matrix $\mathbf{Q}$, which has m columns (histories) and n rows (channels). The deviation display algorithm takes as input parameter the weighted column-vector $\mathbf{w}$ and adds it to the display matrix $\mathbf{Q}$ ($m \times n$ elements), thus pushing out the oldest spectra if more than m measurements exist. In surveys with high-purity germanium (HPGe) detectors, using a conversion gain of n=4096 channels or more is not uncommon. With m=250 histories to display, this means that over 10^6 elements has to be evaluated and displayed for each new sampled spectra. But since a 4096 pixel column will not fit onto most computer screens, $\mathbf{w}$ can be scaled down to, for example, a 512 element vector by forming one new bin out of every eight channels.

[1] MATLAB is a software package produced and supported by The MathWorks, Inc, Natick, MA, USA.

2.2. Background estimation

As the number of collected spectra j grows, each channel mean $m_{i,j}$ will approach the true background mean as long as there is no systematic changes in the background radiation level. This will result in a homogeneous deviation display dominated by the background colour of choice. In other words, the stochastic background fluctuations within each channel will be suppressed, enhancing significant positive changes in the count rate.

The optimal size of the set of spectra, j, can vary depending on the prerequisites of the measurement situation. Normally more samples give a better estimation, but this is not always the case in mobile gamma spectrometry, since the samples are not drawn from the same distribution. If the background radiation level is drastically changing over short distances (hundreds of metres), as in many urban areas, a high spatial resolution can be favourable, thus limiting the number of samples, j, which can be used to build up a representative background. In the other extreme, a background where the fluctuations are purely stochastical, allows for a large j giving a very good estimation of the background level in each channel. This situation, or at least a good approximation of it, can be found when the detector is stationary, like in most laboratories.

A number of different background subtraction techniques exist. In a recently published study, independent of this work, Cresswell and Sanderson (2009) used a rolling average background constructed from filtered difference spectra. The filtering was based on both full spectrum count rates and count rates for the spectral windows used in the standard windows stripping analysis. Spectra passing all the filters were added to the rolling background. In this work, the filtering is instead done on a channel-by-channel (or bin-by-bin) basis as shown in Eq. (4), rejecting only negative $q_{i,j}$. Furthermore, as described below, the background approach here is different from that of Cresswell and Sanderson (2009). To make the method detector-independent it is necessary to allow for a fairly large number of background spectra j. While 30 s of background sampling might be enough for large NaI(Tl) that is seldom the case for HPGe and small NaI(Tl) detectors, given moderate background levels.

In the field experiment (see next section) the same methodology for background sampling as described in Hjerpe et al. (2001) was used. Here, instead of deciding alarm levels, the background measurements were used to sample the relative deviations, $q_{i,j}$. Hjerpe and Samuelsson (2003) showed that a representative background distribution could be estimated after about 45 min by driving around the area where the experiments should take place. Since the field experiment in this work was undertaken at the same site, this result applies here as well. Hence the natural background distribution, shown in Fig. 1, was sampled by driving around the area in question for about 45 min.

3. Materials and experiments

3.1. Spectrometry systems

In the field experiment a P-type high-purity germanium (HPGe) detector,[2] model no. GEM 100-S, with 123% relative efficiency from Ortec[3] was mounted in a GMC van at a height of approximately 2 m above the ground. The detector's cylinder axis was horizontally orientated with the end-cap facing the rear of the van. A digital, portable, multi-channel analyser (MCA, Ortec Digidart), with the conversion gain set to 4096 channels was used.

[2] s/n p41629A

[3] Ortec, 801 S. Illinois Ave., Oak Ridge, TN, USA.

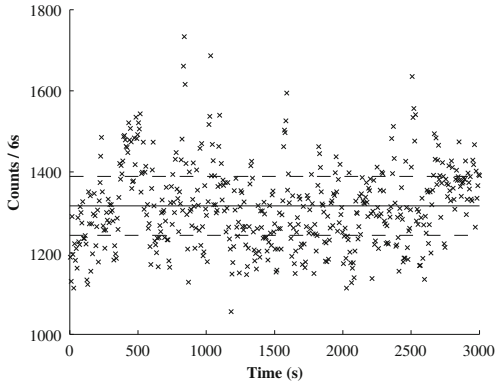

Fig. 1. Full spectrum gross count rates of background measurements from the field experiment at Revingehed. The dashed lines mark ± 2 standard deviations about the mean (solid line) of a Poisson distribution.

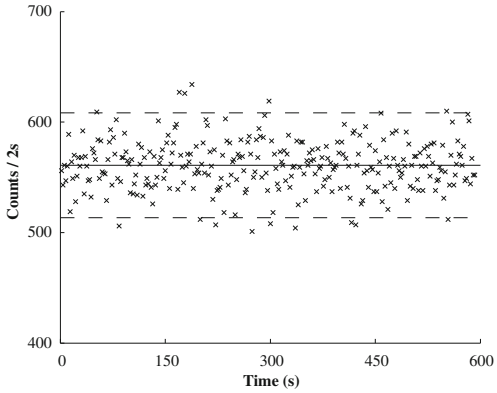

Fig. 2. Full spectrum gross count rates of background measurements from the laboratory experiment. The dashed lines mark the ± 2 standard deviations about the mean (solid line) of a Poisson distribution.

The MCA communicated with a laptop-PC over the USB (Universal Serial Bus) interface, sending a new pulse height distribution when requested. To reduce microphonia due to the roughness of the road, the detector was mounted on a layer of approximately 10 cm of foam rubber.

The NaI(Tl) spectrometry system used in the laboratory experiment is a portable backpack solution. It uses a 7.62 $\times$ 7.62 cm cylindrical detector[4] from Saint-Gobain,[5] model no. 3M3/3, equipped with a 14-pin PMT (photomultiplier tube), integrated bias supply, pre-amplifier and digital MCA manufactured by Ortec (Ortec Digibase). The system was made for field use and assembled by Gammadata.[6]

3.2. Field experiment

To test the sensitivity of the method described in this work on a strong point source far away, a field experiment was undertaken at the military training ground near Revingehed, 15 km east of Lund, Sweden. An isotropic ^{137}Cs source with an activity of 1.8 GBq, sealed in a 2 mm thick steel capsule, was used to represent an orphan source.

The critical distance (CD) is defined by Hjerpe and Samuelsson (2003) as "the distance from the road at which a source can be detected with 50% probability when driving by". Here, the source was placed at $D=130$ m perpendicular to a 400 m long straight stretch of the road and driven by 10 times at a speed of 50 km h^{-1}. This distance was not arbitrarily chosen, it equals the CD of a 2 GBq ^{137}Cs source using a 7.62 $\times$ 7.62 cm NaI(Tl) system and the PSC-method, as shown by Hjerpe and Samuelsson (2003).

With the source sealed in the steel capsule and at a distance of 130 m, the primary photon fluence rate at the road was approximately 10% lower than that for the same distance in Hjerpe and Samuelsson (2003). This difference is balanced by the slightly larger detector used in this work, making the experiment carried out in this work comparable to those of Hjerpe and Samuelsson (2003), in terms of sensitivity.

3.3. Laboratory experiment

To demonstrate the cross-detector application of the deviation display method a small-scale experiment with a ^{241}Am source (70 kBq) was done using the NaI(Tl) backpack system described above. By choosing a primary photon energy in the X-ray band (60 keV), the natural background level is substantially increased due to scattered photons. This energy was chosen to demonstrate the ability of the DD-method to enhance positive changes in an energy band with higher background noise, where a weak signal is harder to distinguish.

A plastic tube containing the sealed ^{241}Am source was carried ten times past the detector at close range ($\simeq 10$ cm) and at a slow constant speed (< 5 km h^{-1}). After every passage there was a pause for a few seconds to make each passage distinguishable. The sampling rate was 0.5 Hz. In this experiment the natural background distribution, shown in Fig. 2, was sampled for about 10 min. This relatively short time results in greater uncertainties in the measured channel means. However, when the detector is stationary, 10 min of measurements will suffice to give a rough approximation of the natural background.

3.4. MOBCAL-08 exercise

During 2008 the Swedish Radiation Protection Authority organised an exercise (MOBCAL-08) in the surroundings of Gävle in central Sweden. One task was to measure the background radiation levels using carborne gamma-ray spectrometry. As this area holds many places with high concentrations of radiocaesium due to Chernobyl fallout (NKS, 2002), the focus of the exercise was mainly on ^{137}Cs.

An excerpt of the background measured in the exercise by a team from the Swedish Customs is presented here to show some of the relative strengths and weaknesses of the DD compared to the normal waterfall display. The data were measured with a GR-460 system manufactured by SAIC Exploranium,[7] which uses a 4L NaI(Tl). Raw data for the 512 channels were extracted from the save files produced by the GR-460 software. The sampling rate was 1 Hz and the car held a speed of about 30 km/h. The

[4] s/n 60004-02515-1
[5] Saint-Gobain Cristaux, 104 Route de Larchant, Nemours, France.
[6] Gammadata Instrument AB, Vallong. 1, Uppsala, Sweden.
[7] SAIC Headquarters, 1710 SAIC Drive, McLean, VA, USA.

background gross counts along with the ^{137}Cs-window gross counts of the excerpt are presented in Fig. 6, for comparison with Figs. 1–2.

4. Results and discussion

Three examples are presented to elucidate the behaviour of the deviation display method, the field experiment represent a strong source far away and the laboratory experiment represent a weak source close to the detector, lastly an example from a more challenging background environment is presented.

4.1. Background distributions

The background gross count rates presented in Figs. 1, 2 and 6 were used to characterise the background environments. The $\pm 2\sigma$ dashed lines in the figures should contain about 95% of the samples given a single pure Poisson distribution. As expected, the variances are greater in the outdoor background distributions, where the detector is constantly moving around, thus sampling from a large number of different Poisson distributions. About 52% and 34% of the sampled counts are within the $\pm 2\sigma$- region for the field experiment and the MOBCAL-08 exercise backgrounds, respectively, while this region contained about 95% for the laboratory experiment. A good agreement with the theoretical Poisson distribution was expected in the laboratory experiment since the detector was stationary.

The statistical dispersion of the natural radiation background sampled at the field experiment site is still fairly low when compared to, for instance, that of an urban area (Jarman et al., 2008) or that of the MOBCAL-08 exercise (Fig. 6). This relative homogeneity in the background radiation levels also allowed for a large j, without increasing the risk of estimating the channel means from samples of an unrepresentative background distribution when driving around. A direct consequence of this "low-background" is that a CD measured at Revingehed with a certain method and detector system should be quite close to the ideal CD for that configuration.

A much more fluctuating background environment is seen in Fig. 6, showing some systematic changes which leads to a non-poissonian behaviour. As only 34% of the full spectrum counts fall within the range of $\pm 2\sigma$, finding an representative estimate of the channel means valid for the whole set is difficult if not impossible. The strong correlation between ^{137}Cs window gross counts and the full spectrum gross counts, both shown in Fig. 6, also confirms that Chernobyl fallout constitutes most of the background in the area. High and heterogeneous ^{137}Cs levels characterise this area, favouring a higher spatial resolution, thus favouring a relatively short background i.e. small j.

4.2. Deviation display method

The result from the HPGe field experiments at Revingehed is shown in Fig. 3. Several γ- lines from the natural background can be seen in the conventional waterfall display in the left half of Fig. 3. Among them, the 1.46 MeV line from ^{40}K is the most prominent. Colours are calculated with Eq. (5), so that q_{max} is displayed in white in the deviation display. In the conventional waterfall display the maximum count rate measured is displayed in white.

To avoid the influence of previous passages in the subsequent all statistics (m, s, j, q and q_{max} in Eqs. (1)–(5)) were reset to their background values after each source passage. The background value is simply a value stored immediately before the first source passage. This procedure, used in both the field and laboratory experiments, gives each run the same basic conditions in terms of deviation from the mean, and hence detection. This procedure is necessary to make each individual source passage comparable to the others as well as to Hjerpe and Samuelsson (2003), where the moving background was free of any source influence by the time of next passage.

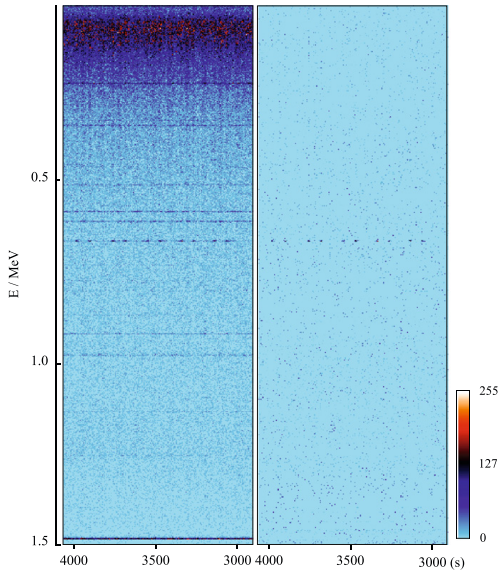

Fig. 3. Normal waterfall display (left) and new deviation display (right) from HPGe detector measurements, when passing the ^{137}Cs source ten times. Each pixel-column shows data sampled during 6 s. Data is pushed from left to right so that the oldest spectra is on the far right side of the figure.

As can be seen in Fig. 3, the image produced using the deviation display method is much more homogeneous than the normal waterfall display. The natural background is effectively suppressed, so that the lines disappear, leaving a display dominated by the background colour of choice. At the same time the method enhances positive significant changes over the whole energy range covered by the display, leaving the ten dots from the ^{137}Cs source passages.

The choice of n in Eq. (4), i.e. the number of standard deviations, is a balance between sensitivity and statistical strength. The DD images in Figs. 3 and 5 are produced using $n=2$, which gives a reasonable balance between the background noise level and the enhancement of changes on the positive side. For comparison, Fig. 4 shows the first four ^{137}Cs passages (rightmost in Fig. 3) from the field experiments, for three different n. As can be seen in the figure, the background suppression works better for the two higher values of n. On the other hand the source passages are "sharpened", covering smaller and smaller areas around the peak's centre channel with increasing n.

Fig. 5 shows the output from the low-energy region from the laboratory NaI(Tl) experiment. Again, the source's passage can be seen in both displays, but are more prominent in the deviation display. The poorer resolution of the NaI(Tl) detector results in

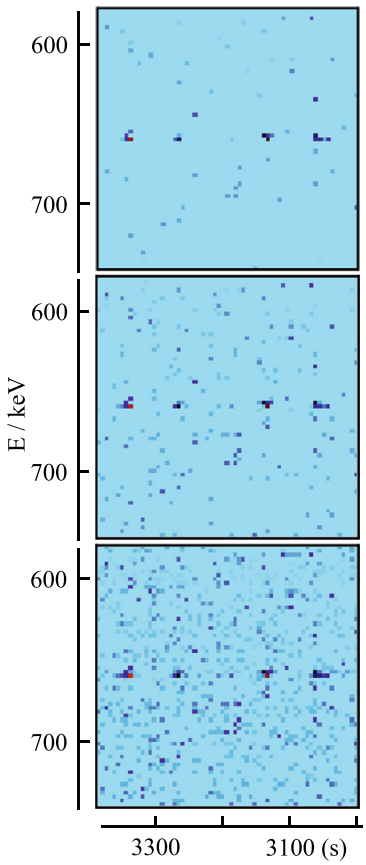

Fig. 4. Detailed view of the first four ^{137}Cs source passages from the field experiment, plotted for three different number of standard deviations, i.e. three different n from Eq (4). Bottom $n=1$, middle $n=2$ and top $n=3$.

broadened full energy "peak-lines" rather than the "peak-dots" observed in the HPGe-measurements (Figs. 3 and 4). The slightly higher noise level seen in Fig. 5 can be explained by the incomplete background estimation prior to the source passages and by the zoom level of the figure. This experiment shows that the deviation display method works well after about 10 min of background sampling for a stationary detector of this size, even in this high background regime.

The last 200 s from the 4L NaI(Tl) MOBCAL-08 exercise excerpt are shown in Fig. 7. The difference solely from the choice of background algorithm are presented in Fig. 7, showing two deviation displays produced using both a long (> 300 s) and a short (50 s) background. The high ^{137}Cs levels at the beginning of the excerpt leaves a band of void in the long background DD, while the short background DD displays some variations in ^{137}Cs levels. The DDs in Fig. 7 are also less homogeneous than the ones in Figs. 3–5, mainly due to drastic changes in the background level fluctuations (compare Figs. 1,2 and 6), but also due to the choice of n. The DDs in Fig. 7 were produced using $n=1$, which better shows the differences between the background algorithms.

A local ^{232}Th feature, visible in Fig. 7 through ^{208}Tl (2.61 MeV) and scattered radiation, appear after about 420 s. It is clearly visible and easily identifiable in the DDs alone. The normal waterfall display reveals a high contribution in the lower parts of the energy spectrum due to scattered photons from ^{232}Th daughters, with a slight enhancement to the 2614 keV ^{208}Tl peak. But the signal above about 1.5 MeV is clearly visible in the DDs only.

Background sampling times from 50 s to 45 min were used in this work. The initialisation time required for the DD method to produce an acceptable display depends on the detector type and size, the number of bins used and the background radiation level. However, as shown in the examples above, 10 min of sampling is enough for all but the most extreme scenarios.

5. Conclusions

The superior resolution of a HPGe-system compared to a NaI(Tl)-based system results in a narrower full energy region and thus a lower inherent background, giving a much sharper display. Hence, a source placed at the critical distance of a specific NaI(Tl)-system should be clearly observable when using a HPGe-system of equal size. This is confirmed on a qualitative level by the ten clearly visible dots produced by the deviation display, seen in Fig. 3. The results presented here are thus in line with those of Ziock and Nelson (2007), who argued that a semiconductor system will out perform a scintillation-based system of comparable size, given that spectroscopy can be used to limit the background (which is the case in this work).

The deviation display method gives satisfactory results for all tested systems, and at all tested energies. This method should, in fact, work with any detector used in mobile gamma spectrometry today, since it is based on relative comparisons. Furthermore, as a consequence of the relative comparisons, there is no need to rewrite the software when switching between detector types. The key to a good result using this method is stability in energy over time, since each channel (or bin) has its own statistics.

The initialisation time for the method depends on both internal (detector type and size and the number of bins) and external (background environment and shielding) factors. From the results of this work we conclude that 10 min of sampling, stationary or mobile, would be a sufficient initialisation time for all but the most extreme detector/background scenarios.

Depending on the characteristics of the background environment, the choice of background sampling technique giving the best deviation display differ. When the detector is stationary, a large number of background spectra yields a more representative mean, hence giving a more homogeneous and "eye friendly" display. The same conclusion applies when mobile in areas with small to moderate systematic changes in the background radiation levels, for example that of the field experiment presented in this work. Conversely when mobile in more challenging environments a small number of background spectra is preferable. A conservative choice when searching for anomalies in an unknown area would be to start with a fairly small rolling background. The size may then be gradually increased (decreased), manually or by an algorithm checking the background variations, if the variations are low (high).

The deviation display method can also be a quick and convenient way to ensure that the detector system is working properly and that it is stable. Energy drift or microphonia can be readily spotted in the display as perturbations in the background levels. A slight energy calibration drift would appear as a new thin false source line in the DD. This should draw the attention of the

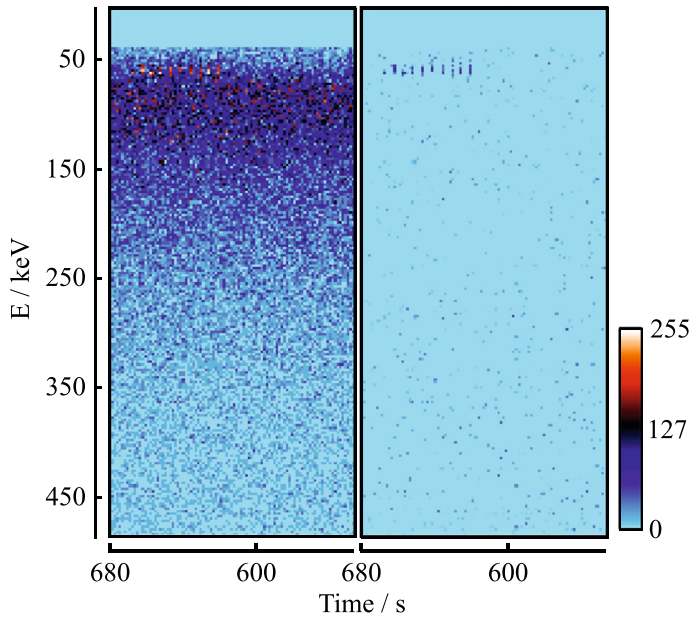

Fig. 5. Normal waterfall display (left) and new deviation display (right) from the laboratory experiment. The ^{241}Am source passes the detector ten times at a slow speed. Each pixel-column shows data sampled during 2 s. Data is pushed from left to right so that the oldest spectra is on the far right side of the figure.

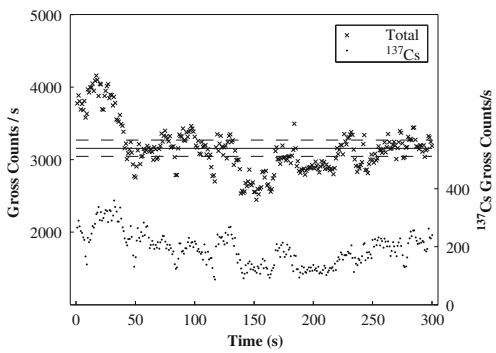

Fig. 6. Full spectrum and ^{137}Cs window gross count rates from the MOBCAL-08 exercise excerpt. The dashed lines mark the ± 2 standard deviations about the mean (solid line) of a Poisson distribution.

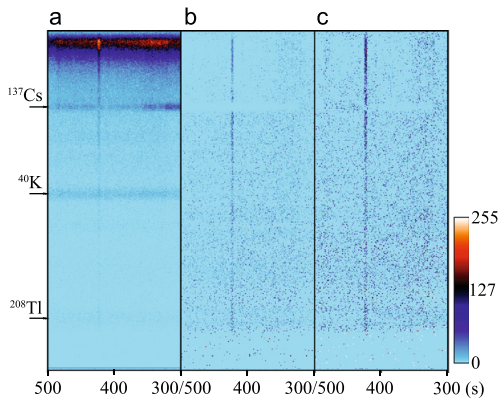

Fig. 7. The last 200 s of the MOBCAL-08 4L NaI(Tl) excerpt showing a local ^{232}Th feature. Normal waterfall display (a) and deviation displays sampled with approximately 300 s of background (b) and a rolling background of 50 s (c).

operator, who then can identify the perturbation by studying the normal waterfall display.

When searching for orphan sources or mapping contaminated areas, the new semi-automatic deviation display method presented here could assist the operator. It is automated in that the method continuously sorts out significant changes on the positive side. On the other hand the operator will have to study the display at all times to be able to detect an orphan source or increased levels of radioactivity. In conclusion, the search operation could benefit from combining the deviation display method with some fully automatic real time alarm method (see for example: Hjerpe and Samuelsson, 2003 or Jarman et al., 2008).

Acknowledgement

This work was supported by the Swedish Radiation Safety Authority, SSM.

References

Aage, H.K., Korsbech, U., 2003. Search for lost or orphan radioactive sources based on NaI gamma spectrometry. Appl. Radiat. Isot. 58, 103–113.

Cresswell, A.J., Sanderson, D.C.W., 2009. The use of difference spectra with a filtered rolling average background in mobile gamma spectrometry measurements. Nucl. Instrum. and Methods A 607, 685–694.

Hjerpe, T., Finck, R.R., Samuelsson, C., 2001. Statistical data evaluation in mobile gamma spectrometry: an optimization of on-line search strategies in the scenario of lost point sources. Health Phys. 80 (6), 563–570.

Hjerpe, T., Samuelsson, C., 2003. A comparison between gross and net count methods when searching for orphan radioactive sources. Health Phys. 84 (2), 203–211.

International Atomic Energy Agency (IAEA). 2004. Strengthening control over radioactive sources in authorized use and regaining control over orphan sources. IAEA-TECDOC-1388, Vienna.

Jarman, K.D., Runkle, R.C., Anderson, K.K., Pfund, D.M., 2008. A comparison of simple algorithms for gamma-ray spectrometers in radioactive source search applications. Appl. Radiat. Isot. 66, 362–371.

Mellander, H., 1998. Mobile gamma spectrometry. Stockholm SSI News 6 (1), 1–3.

NKS, 2002. In: Mellander, H., Aage, H.K., Karlsson, S., Korsbech, U., Lauritzen, B., Smethurst, M. (Eds.), Mobile Gamma Spectrometry Evaluation of the Resume 99 exercise. NKS-56. NKS Secretariat Roskilde, Denmark. ISBN 87-7893-111-8.

Tewari, S.G., Nagaraja, K.N., Surya Kumar, N.V., 1988. Data enhancement techniques for airborne gamma ray spectrometric data. IAEA-TECDOC-472, 87-116. Vienna; 1988.

Ziock, K.P., Burks, M.T., Craig, W., Fabris, L., Hull, E.L., Madden, N.W., 2003. Real-time generation of images with pixel-by-pixel spectra for a coded aperture imager with high spectral resolution. Nucl. Instrum. and Methods A 505, 420–424.

Ziock, K.P., Fabris, L., Carr, D., Collins, J., Cunningham, M., Habte, F., Karnowski, T., Marchant, W., 2007. A fieldable-prototype, large-area, gamma-ray imager for orphan source search. In: IEEE Nuclear Science Symposium Conference Record, vol. 2, pp. 949–958.

Ziock, K.P., Nelson, K.E., 2007. Maximum detector sizes required for orphan source detection. Nucl. Instrum. and Methods A 579, 357–362.

Paper II

Nuclear Instruments and Methods in Physics Research A 681 (2012) 55–60

Contents lists available at SciVerse ScienceDirect

Nuclear Instruments and Methods in Physics Research A

journal homepage: www.elsevier.com/locate/nima

A real-time statistical alarm method for mobile gamma spectrometry—Combining counts of pulses with spectral distribution of pulses

Peder Kock [a,*], Jan Lanke [b], Christer Samuelsson [a]

[a] Medical Radiation Physics, Department of Clinical Sciences Malmö, Lund University, Skåne University Hospital Malmö, SE-205 02 Malmö, Sweden
[b] Department of Statistics, Lund University, Sweden

ARTICLE INFO

Article history:
Received 9 September 2011
Received in revised form
2 April 2012
Accepted 13 April 2012
Available online 21 April 2012

Keywords:
Gamma spectrometry
Hypothesis testing
Low counts
Multinomial distribution

ABSTRACT

A well-founded decision needs to take into account as much information from a sample as possible. In gamma spectrometry, the number of photons and their energy are the two quantities readily accessible to the physicist and both should be used in order to increase the power of a statistical test. While the problem of counts of pulses has been much studied the problem of spectral distribution of pulses has been generally overlooked. This work presents a statistical test combining tests on count rate and tests on spectral distribution. The proposed method is shown to have an acceptable false positive rate and, when compared with two other test statistics found in the literature, greater power.

1. Introduction

Statistical inference about analyte activity present in a sample is an important research topic in health physics and part of the more fundamental question: is there a signal present? To answer this question, using statistical inference, one either accepts or rejects the null hypothesis

H_0 : No signal present in sample
versus
H_1 : Signal present in sample

at an *a priori* determined significance level, α. The test statistic used can vary, but ideally the probability of rejecting H_0 when it is in fact true, i.e. a false positive or type I error, should be α [5].

Strom and MacLellan [19] evaluated eight test statistics with respect to their actual false positive rates, α'. For the lowest count rates (typically a Poisson mean $\mu_b < 2$), they found that no method satisfied the predefined significance level, α. It has long been known that this result is due to the discrete nature of counting statistics and the effects are especially severe in the low-level region (see e.g. [2,7,14]). Interestingly, the most well-known method in the health physics field, given by Currie [9], also showed the worst result with regard to α', even for intermediate count rates, while the method of Stapleton showed good results, i.e. $\alpha' \approx \alpha$ for $\mu_b > 5$ [19].

Taking into account the spectral information in a gamma-ray spectrum (or histogram) should increase the power of the test, but going from one bin to multiple bins also increases the complexity of the problem. One method, which calculates the probability for each possible pulse configuration, given some background distribution, was presented by Méray [15]. Compared with the single-bin method of Currie this approach significantly lowered the *detection limit* (see Ref. [9] for a definition) [16].

This work presents a new test based on a combination of a count rate test, viz. a modification of the Sumerling and Darby (S&D) test [20], and a likelihood ratio test of the spectral distribution of the counts. The two *p*-values so obtained are subjected to Fisher's method for combining *p*-values. Both the false and true positive rates for the proposed method are evaluated and compared with those of several other methods.

The method described in this work is designed for, and evaluated in, a mobile gamma spectrometry context. This typically means conducting repeated short-term measurements, possibly for an extended period of time, while searching for a radioactive source. To avoid too many false positive alarms the chosen α is small (0.1–1%) and the count rates in the simulations are low to intermediate ($5 \leq \mu_b \leq 30$). High count rate environments, where pulses are abundant, can provide many challenges but generally not with respect to the problem addressed in this

* Corresponding author. Tel.: +46 40 33 86 64.
E-mail address: peder.kock@med.lu.se (P. Kock).

0168-9002/$ - see front matter © 2012 Elsevier B.V. All rights reserved.
http://dx.doi.org/10.1016/j.nima.2012.04.038

work. The present work might still be useful in other scientific fields, despite the chosen context.

2. Theory and methods

Starting with the basic model of radioactive counting, the Poisson distribution, we show that the spectral distribution of pulses, given the total count, is described by binomial or multinomial probabilities, depending on the number of channels used. We then present two hypotheses that split the radioactive counting problem into two parts: first, the problem of pulse sums, and secondly, the problem of spectral distribution.

2.1. Single-channel Poisson model

Suppose we have a radioactive counting experiment with two samples. These samples will henceforth be referred to as *background* and *sample*. Suppose also that the experiment involves only one channel in which pulses are registered. The probability of observing k pulses from *sample* is a Poisson probability

$$P(X=k)=\frac{e^{-\mu}\mu^k}{k!} \tag{1}$$

where μ is the true mean. Substituting μ by λ in Eq. (1) then gives the probability of observing k pulses from *background*. By combining the counts from sample, x, and background, y, so that $z=x+y$, the conditional probability of observing a sample-background pair can be written

$$P(X=x,Y=y|Z=z)=\binom{z}{x}q^x(1-q)^y \tag{2}$$

where $q=\mu/(\mu+\lambda)$. For a derivation, which is straight-forward using two Poisson distributions, see e.g. [6,19].

An interesting observation is that in high energy physics (HEP) and gamma-ray astronomy (GRA) the single-channel problem of Poisson ratios is called signal-bin/sideband and the on/off problem respectively. It is an old problem that has got much attention, see e.g. Cousins et al. [6] for a comprehensive review. The problem is also well known in the health physics/gamma-ray spectroscopy field, see e.g. [1,9,10,18,19].

2.2. Dual-channel properties

If the pulses from sample and background are split into two separate channels, c_1 and c_2, then for each channel the probability of observing k pulses from background or sample is given by Eq. (1), substituting μ by the appropriate true mean. The joint probability of observing x_1 and x_2 pulses from sample in the two channels is then

$$P(X_1=x_1,X_2=x_2)=P(x_1)P(x_2)=\frac{e^{-\mu_1}\mu_1^{x_1}}{x_1!}\frac{e^{-\mu_2}\mu_2^{x_2}}{x_2!} \tag{3}$$

where the first step can be carried out since the random variables X_1,X_2 are assumed to be independent. The background pulses are also Poisson distributed with true means λ_1,λ_2 in c_1 and c_2 respectively. The probability of observing $Y_1=y_1$ and $Y_2=y_2$ counts in background is also given by Eq. (3), substituting μ_i by λ_i. The conditional probability of observing a pair of counts from sample, given the sum of the counts, can be shown to be

$$P(X_1=x_1|X_1+X_2=x)=\binom{x}{x_1}\left(\frac{\mu_1}{\mu_1+\mu_2}\right)^{x_1}\left(\frac{\mu_2}{\mu_1+\mu_2}\right)^{x-x_1} \tag{4}$$

and analogously for the background

$$P(Y_1=y_1|Y_1+Y_2=y)=\binom{y}{y_1}\left(\frac{\lambda_1}{\lambda_1+\lambda_2}\right)^{y_1}\left(\frac{\lambda_2}{\lambda_1+\lambda_2}\right)^{y-y_1} \tag{5}$$

2.3. Multichannel properties

Moving on to k channels and using the notation

$$x=x_1+x_2+\cdots+x_k \tag{6a}$$

$$\mu=\mu_1+\mu_2+\cdots+\mu_k \tag{6b}$$

$$q_1=\frac{\mu_1}{\mu},\ q_2=\frac{\mu_2}{\mu},\ldots,q_k=\frac{\mu_k}{\mu} \tag{6c}$$

$$\mathbf{x}=(x_1,x_2,\ldots,x_k) \tag{6d}$$

$$\mathbf{q}=(q_1,q_2,\ldots,q_k) \tag{6e}$$

the probability of observing $\mathbf{x}$ in channels $1,2,\ldots,k$ is

$$\begin{aligned}P(\mathbf{x})&=\frac{e^{-\mu}\mu^x}{x_1!x_2!\cdots x_k!}\left(\frac{\mu_1}{\mu}\right)^{x_1}\left(\frac{\mu_2}{\mu}\right)^{x_2}\cdots\left(\frac{\mu_k}{\mu}\right)^{x_k}\\&=\frac{e^{-\mu}\mu^x}{x!}\binom{x}{x_1,x_2,\ldots,x_k}q_1^{x_1}q_2^{x_2}\cdots q_k^{x_k}\end{aligned} \tag{7}$$

where

$$\binom{x}{x_1,x_2,\ldots,x_k}=\frac{x!}{x_1!x_2!\cdots x_k!}$$

is a multinomial coefficient. The conditional probability of observing $\mathbf{x}$, given a total of x pulses, is then

$$P(\mathbf{x}|x)=\frac{P(\mathbf{x})}{P(x)}=\binom{x}{x_1,x_2,\ldots,x_k}q_1^{x_1}q_2^{x_2}\cdots q_k^{x_k} \tag{8}$$

which is a probability in a multinomial distribution, $\mathrm{Mult}_k(x;\mathbf{q})$. Note that if we are interested only in the ith frequency in Eq. (8) it is binomially distributed

$$(x_i|x)\in\mathrm{Bin}(x,q_i). \tag{9}$$

The probability of observing a spectral distribution $\mathbf{y}$ within background can be derived using Eqs. (6) and (7), substituting x_i and μ_i by y_i and λ_i.

2.4. Hypotheses

To test if sample and background are two samples from the same underlying distribution several tests and hypotheses can be constructed. In this work we choose to study two different hypotheses, the first one, $H_0^{(S)}$, concerning the pulse sum and the second, $H_0^{(R)}$, concerning the spectral distribution within the samples

$$H_0^{(S)}:\sum_{i=1}^{k}\mu_i=\sum_{i=1}^{k}\lambda_i \tag{10a}$$

$$H_0^{(R)}:\mu_i/\mu=\lambda_i/\lambda\quad\text{for } i=1\ldots k \tag{10b}$$

$$H_0^{(SR)}:\mu_i=\lambda_i\quad\text{for } i=1\ldots k \tag{10c}$$

where, as easily seen, $H_0^{(SR)}$ is the combination of $H_0^{(S)}$ and $H_0^{(R)}$.

2.5. Test statistics for $H_0^{(S)}$

2.5.1. Sumerling and Darby's method

The probability mass function (pmf) of S&D is given in Eq. (2). Summing over all probabilities from x up to $z=x+y$ gives the

probability of observing x or more pulses in sample, given the sum, z, of the pulses in sample and background

$$P_{\mathrm{SD}} = \sum_{i=x}^{z} \binom{z}{i} q^i (1-q)^{z-i} \tag{11}$$

which is the test statistic [20]. If the counting times of sample and background are equal, then $q=1/2$. In the case of different counting times for sample (t_x) and background (t_y), q becomes

$$q = \frac{t_x}{t_x + t_y} \tag{12}$$

The null hypothesis, $H_0^{(S)}$, that the sample is blank is rejected if a blank sample would have produced a gross count at least as large as the one observed at most $100\alpha\%$ of the time [20]; that is, if

$$P_{\mathrm{SD}} \le \alpha. \tag{13}$$

As noted by Refs. [2,7], the binomial test is known to be conservative, i.e. it will always reject H_0 less than $100\alpha\%$ of the time under H_0.

2.5.2. Currie's method

The test proposed by Currie [9] is based on a comparison of the net count $x-y$ and the quantity

$$C_{\mathrm{currie}}(y) = k_\alpha \sqrt{2y} \tag{14}$$

where k_α is the quantile of a standard normal distribution such that $P(X > k_\alpha) = \alpha$; $H_0^{(S)}$ is rejected at the α-level if $x-y > C_{\mathrm{currie}}$.

ANSI/HPS N13.30-1996 [12] presented Eq. (14) in a more general form, where the counting times of background (t_y) and sample (t_x) can be different

$$C_{\mathrm{N13.30}}(y,t_x,t_y) = k_\alpha \sqrt{\frac{y}{t_y}\left(\frac{1}{t_x} + \frac{1}{t_y}\right)} \tag{15}$$

Strom and MacLellan [19] therefore dubbed this variant of Currie's rule to "N13.30". In this form the null hypothesis, $H_0^{(S)}$, is rejected if the net count rate $R_n = x/t_x - y/t_y > C_{\mathrm{N13.30}}$.

2.5.3. Stapleton's method

Stapleton's method, described in [19], computes a standard normal deviate, $z_{\mathrm{stapleton}}$, from the observed counts x, y and counting times t_x, t_y

$$z_{stapleton}(x,y,t_x,t_y) = 2\frac{\sqrt{\frac{x+d}{t_x}} - \sqrt{\frac{y+d}{t_y}}}{\sqrt{\frac{1}{t_x} + \frac{1}{t_y}}} \tag{16}$$

where d is a parameter, $0 < d < 1$. Throughout this work, d was 0.4 to be comparable to the results of Strom and MacLellan [19]. Using this test, $H_0^{(S)}$ is rejected if $z_{\mathrm{stapleton}} > k_\alpha$.

2.5.4. Sumerling and Darby, mid-p version

As noted above, the S&D method is known to be conservative. A proposition to remove the conservativeness of discrete test statistics was proposed by Lancaster [14]; the method has been evaluated and recommended by e.g. Refs. [2,3,7]. In our case the technique amounts to taking only half the probability in the first term of Eq. (11)

$$\begin{aligned} P_{\mathrm{SDmidp}} &= \frac{1}{2}P(X = x|z) + P(X > x|z) \\ &= \frac{1}{2}\binom{z}{x} q^x (1-q)^{z-x} + \sum_{i=x+1}^{z} \binom{z}{i} q^i (1-q)^{z-i} \end{aligned} \tag{17}$$

where the second term is interpreted as zero if $x=z$. As for the S&D-method, $H_0^{(S)}$ is rejected at the α-level if $P_{\mathrm{SDmidp}} \le \alpha$. Since $P_{\mathrm{SD}} > P_{\mathrm{SDmidp}}$ the latter version will be less conservative.

2.6. Test statistics for $H_0^{(R)}$

2.6.1. Goodness-of-fit test

The fit of a multinomial model to a data set, $\mathbf{x}$, can be tested using a goodness-of-fit (GoF) test [4]. The probability of observing a data set at least as extreme as the one observed, $P(\mathbf{x})$, can be written as

$$P_{\mathrm{fit}} = \sum_{\mathbf{a}:P(\mathbf{a}) \le P(\mathbf{x})} P(\mathbf{a}). \tag{18}$$

To test if an observed outcome $\mathbf{x}$ came from a distribution according to the null, Cressie and Read [8] gives the following four-step recipe:

1. For every possible outcome $\mathbf{a}$, calculate the probability $P(\mathbf{a})$ according to Eq. (8).
2. Rank the probabilities from smallest to largest.
3. Starting with the smallest rank, add the consecutive probabilities up to and including that associated with $\mathbf{x}$; this cumulative probability gives the chance of obtaining an outcome that is no more probable than $\mathbf{x}$.
4. Reject H_0 if this cumulative probability is at most α.

Naively traversing all combinations at least as extreme as $\mathbf{x}$ (steps 1 and 2) quickly becomes computationally infeasible, as the number of channels k, and pulse sum x, grow. To overcome this, an approximation to the distribution of the log-likelihood ratio statistic G^2 can be used instead. One such approximation, based on Fast Fourier Transform (FFT), is given by Keich and Nagarajan. The p-value of the fit is approximated from the entropy score

$$s_0 = \sum_{i=1}^{k} x_i \ln\left(\frac{x_i}{\pi_i x}\right) \tag{19}$$

where π_i are the expected background cell probabilities and $x = \sum x_i$ [13,17]. However, in order to use the multinomial GoF test, the background probabilities π_i have to be known.

2.6.2. Test using likelihood ratio

A test of the pulse distribution can be performed using the likelihood function. The multinomial probability function is given in Eq. (8). Using the same notation we now have two multinomial observations, the sample $\mathbf{x}$ and the background $\mathbf{y}$, which are independent. The likelihood function is

$$P(\mathbf{x}|x)P(\mathbf{y}|y)$$

where

$$P(\mathbf{x}|x) = c_x \prod_{i=1}^{k} \left(\frac{\mu_i}{\mu}\right)^{x_i} \tag{20}$$

$$P(\mathbf{y}|y) = c_y \prod_{i=1}^{k} \left(\frac{\lambda_i}{\lambda}\right)^{y_i} \tag{21}$$

here c_x and c_y are irrelevant constants.

If we introduce

$$\xi_i = \frac{\mu_i}{\mu}, \quad \eta_i = \frac{\lambda_i}{\lambda}$$

the likelihood function can be written as

$$\mathcal{L}(\boldsymbol{\xi},\boldsymbol{\eta}) = c_x c_y \left(\prod_{i=1}^{k} \xi_i^{x_i}\right)\left(\prod_{i=1}^{k} \eta_i^{y_i}\right) \tag{22}$$

and under the null hypothesis $\xi=\eta$ we get

$$\sup_{H_0}\mathcal{L}=c_x c_y\prod_{i=1}^{k}\left(\frac{z_i}{z}\right)^{z_i} \tag{23}$$

where $z_i=x_i+y_i$, $z=x+y$, while

$$\sup_{H_1}\mathcal{L}=c_x c_y\left(\prod_{i=1}^{k}\left(\frac{x_i}{x}\right)^{x_i}\right)\left(\prod_{i=1}^{k}\left(\frac{y_i}{y}\right)^{y_i}\right) \tag{24}$$

Using the notation

$$\Lambda=\frac{\sup_{H_0}\mathcal{L}}{\sup_{H_1}\mathcal{L}} \tag{25}$$

the log-likelihood ratio statistic is obtained as

$$-2\ln\Lambda=2\sum_{i=1}^{k}\left\{x_i\ln\left(\frac{x_i}{x}\right)+y_i\ln\left(\frac{y_i}{y}\right)-z_i\ln\left(\frac{z_i}{z}\right)\right\}. \tag{26}$$

This statistic has an approximate $\chi^2(k-1)$ distribution for large counts [21]. $H_0^{(R)}$ is rejected at the α level if

$$1-F_{k-1}(-2\ln\Lambda)<\alpha \tag{27}$$

where F_{k-1} is the cumulative chi-square function for $k-1$ degrees of freedom. Note that the method only traverses the sum given in Eq. (26) once, it therefore has linear complexity i.e. $\mathcal{O}(k)$.

In the special case $k=2$ there is a possibility to distinguish between one- and two-sided tests; the version described above is two-sided. However, there are situations where a one-sided test could be useful. Suppose we have two bins, the first one covering a region of interest and the second a region where only background pulses are expected. The alternative hypothesis would then be

$$H_{1,>}:\frac{\mu_1}{\mu}>\frac{\lambda_1}{\lambda}. \tag{28}$$

Clearly $\sup_{H_0}\mathcal{L}$ is still given by Eq. (23) while, cf. Eq. (24)

$$\sup_{H_{1,>}}\mathcal{L}=\begin{cases}\sup_{H_1}\mathcal{L} & \text{if } \frac{x_1}{x}>\frac{y_1}{y}\\ \sup_{H_0}\mathcal{L} & \text{otherwise}\end{cases} \tag{29}$$

and hence

$$\Lambda=\begin{cases}\frac{\sup_{H_0}\mathcal{L}}{\sup_{H_1}\mathcal{L}} & \text{if } \frac{x_1}{x}>\frac{y_1}{y}\\ 1 & \text{otherwise}\end{cases} \tag{30}$$

Now $-2\ln\Lambda$ has, under H_0, an approximate distribution that is no longer $\chi^2(1)$; rather, it is a mixture in equal proportions of a $\chi^2(1)$ and a $\chi^2(0)$ where $\chi^2(0)$ is a one-point distribution at zero.

2.7. The proposed method

Combining a test on the pulse sum, $H_0^{(S)}$, with a test on the pulse distribution, $H_0^{(R)}$, can be expected to present advantages: utilising more of the information contained in the sample will likely increase the power of the test. Given p-values from two independent tests, one can combine them according to Fisher [11]

$$p_{SR}=(1-\ln(p_S p_R))p_S p_R \tag{31}$$

where p_{SR} is the p-value of the combined test. Another possibility is to derive the likelihood ratio directly for $H_0^{(SR)}$, cf. Section 2.4; however, that option is not explored further in this work. Instead we propose using the mid-p version of the S&D method given in Eq. (17) in conjunction with a test on the likelihood ratio, given in Eq. (30). In the present work we consider only the case $k=2$ and use the one-sided version of the likelihood ratio test.

3. Numerical calculations and Monte Carlo simulations

3.1. False positives

The actual false positive rates α' were derived by direct calculations or estimated through paired-blanks Monte Carlo simulations. A recipe for the direct probability calculations of α' is given in Appendix D.1 by Cousins et al. [6]. The direct calculation method was used for all methods testing the pulse sum, i.e. $H_0^{(S)}$. For the methods testing $H_0^{(R)}$ or $H_0^{(SR)}$ the direct method was not used because of the complexity of the multinomial problem.

The false positive rate was evaluated for Poisson true means $\mu=\lambda$, ranging from 5 to 30 with α at 0.1% and 1%. These are strict significance levels; for example Strom and MacLellan evaluated α's from 0.1% to 5%. However, for mobile gamma spectrometry a false alarm rate of more than 1% would be inadequate as many short-term measurements are carried out, often for an extended period of time. For each λ in the simulations, $2k\times10^6$ samples (one sample and one background, for each channel) were drawn from an appropriate Poisson distribution.

3.2. True positives

While the actual false positive rate simulations evaluate the test statistics with respect to their false alarm rate, another set of numerical calculations and simulations were required to evaluate the method's sensitivities. By simulating a ^{137}Cs point source at $r=20$ m from a virtual detector, the different methods were evaluated with respect to their true positive rates, i.e. their sensitivities. In all simulations and calculations 1 s observations were used.

The source emitted photons isotropically which, after attenuation in air, gave rise to a mean count rate, N s^{-1}, in the detector

$$N(A)=\frac{\epsilon p_\gamma e^{-ar}}{4\pi r^2}A=1.683\times10^{-7}A \tag{32}$$

where A is the ^{137}Cs activity (Bq), $a=9.4\times10^{-3}$ m^{-1} the assumed linear attenuation coefficient in air, $p_\gamma=0.851$ the probability of 662 keV photon emission given a ^{137}Cs decay and $\epsilon=1.2\times10^{-3}$ m^2 the assumed detector efficiency. The latter corresponds to a detector with a relative efficiency of roughly 50% in relation to a 3 in. × 3 in. NaI(Tl).

The true positive Monte Carlo simulations were constructed using the following scheme; for each activity A:

1. Perform the following n times:
   i. Draw 2k background samples $a_i,b_i\in\mathrm{Po}(\lambda_i)$.
   ii. Draw ^{137}Cs pulses $a_\gamma\in\mathrm{Po}(N(A))$, cf. Eq. (32).
   iii. Add a_γ to $\mathbf{a}$ according to $\mathbf{p}=(p_1,\ldots,p_k)$.
   iv. Check whether H_0 is rejected at the α-level using $\mathbf{x}=\mathbf{a}$ and $\mathbf{y}=\mathbf{b}$.
2. Estimate the power of the test for activity A

$$1-\beta=\frac{n_{rejected}}{n} \tag{33}$$

where β is the probability of a false negative.

The range of activities tested was $A=[20,200]$ MBq, effectively adding $N=[3.37,33.7]$ pulses per second to the sample. The background count rate, λ_i, was 10. As in the previous section, the results for $H_0^{(S)}$ were instead derived using direct calculation.

4. Results and discussion

4.1. False positives—results under H_0

Results from the false positive calculations and simulations are given in Tables 1–3. Standard errors are given for the simulated results. The results are split into three tables: Table 1 holds the results for test statistics for $H_0^{(S)}$, Table 2 the results for test statistics for $H_0^{(R)}$ and Table 3 for the proposed method, testing $H_0^{(SR)}$. The tests on spectral distribution were done using two bins which had equal probabilities, $p_i = 1/2$, given an event. This has been performed using both the one- and the two-sided version.

With two exceptions the tests perform better at the 1%-level than at the 0.1%-level. The relation between the reference tests, as regards their performance, are the same at the two levels. The results of Currie's test are, as already demonstrated by e.g. Strom and MacLellan, unacceptable. Sumerling and Darby's test is very conservative, but most of this conservativeness is gone when using the mid-p version. Stapleton's test shows the overall best performance, but the proposed test and S&D mid-p test also yield false positive rates close to α. These latter two methods show relatively better results at the 0.1%-level, than at the 1%-level.

Table 1
Actual false positive rates, α', given in %, for the tests on $H_0^{(S)}$.

$\mu=\lambda$	$\alpha=0.1\%$				$\alpha=1\%$			
	Currie	S&D	S&D mid-p	Stapleton	Currie	S&D	S&D mid-p	Stapleton
5	2.768	0.029	0.067	0.143	5.79	0.33	0.65	1.19
10	1.483	0.044	0.078	0.136	3.57	0.55	0.91	1.02
15	0.948	0.051	0.085	0.120	3.08	0.60	0.90	1.00
20	0.742	0.059	0.091	0.108	2.70	0.65	0.94	1.01
25	0.618	0.062	0.092	0.106	2.43	0.70	0.97	1.00
30	0.532	0.065	0.094	0.103	2.22	0.70	0.95	1.02

Table 2
Actual false positive rates, α', given in %, for the tests on $H_0^{(R)}$ using two equiprobable bins. For the cases shown in the table the one-sided and two-sided likelihood ratio tests have identical α'.

$\mu_i=\lambda_i$	$\alpha=0.1\%$		$\alpha=1\%$	
	Likelihood ratio	Goodness-of-fit[a]	Likelihood ratio	Goodness-of-fit[a]
2.5	0.190 ± 0.004	0.001 ± 0.000	1.82 ± 0.01	0.12 ± 0.00
5	0.196 ± 0.004	0.060 ± 0.002	1.47 ± 0.01	0.95 ± 0.01
7.5	0.145 ± 0.004	0.126 ± 0.004	1.22 ± 0.01	1.31 ± 0.01
10	0.125 ± 0.004	0.107 ± 0.003	1.14 ± 0.01	1.25 ± 0.01
12.5	0.124 ± 0.004	0.100 ± 0.003	1.11 ± 0.01	1.12 ± 0.01
15	0.109 ± 0.003	0.103 ± 0.003	1.08 ± 0.01	1.07 ± 0.01

[a] Assumes known π_i.

Table 3
Actual false positive rates, α', given in %, for the proposed method using two equiprobable bins.

$\mu_i=\lambda_i$	Proposed method	
	$\alpha=0.1\%$	$\alpha=1\%$
2.5	0.070 ± 0.003	1.305 ± 0.011
5	0.153 ± 0.003	1.227 ± 0.011
7.5	0.121 ± 0.003	1.088 ± 0.010
10	0.107 ± 0.003	1.031 ± 0.010
12.5	0.103 ± 0.003	1.025 ± 0.010
15	0.097 ± 0.003	0.999 ± 0.010

One can imagine scenarios were it might be appropriate or advantageous to use the goodness-of-fit test, given by Keich and Nagarajan (K&N). One condition must, however, be met in order to use that method: the expected spectral distribution of the background has to be known. One would then expect the GoF test to perform better than the likelihood ratio tests at low values of λ, because the chi-square approximation, which is central to the likelihood ratio tests, is not very good at the lowest values of λ. However, as seen in Table 2, the results of the K&N GoF test are in the same range as the much simpler likelihood ratio tests at the 1%-level.

4.2. True positives—results under H_1

Figs. 1 and 2 present the results from the true positive simulations and calculations at the $\alpha = 0.1\%$-level. Fig. 1 shows the power $(1-\beta)$ of the different methods as a function of the activity, as described in Section 3.2. The methods of Currie and S&D are omitted from Fig. 1 due to their unacceptable false

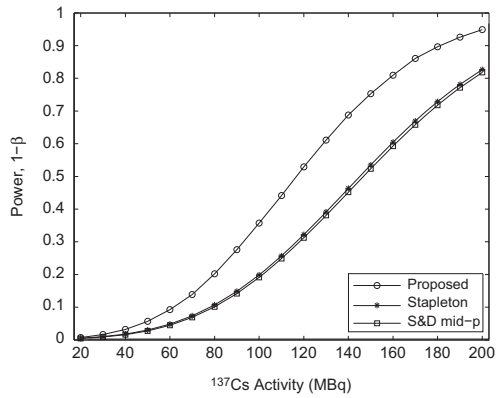

Fig. 1. Actual true positive rates, $1-\beta$, as a function of the ^{137}Cs activity.

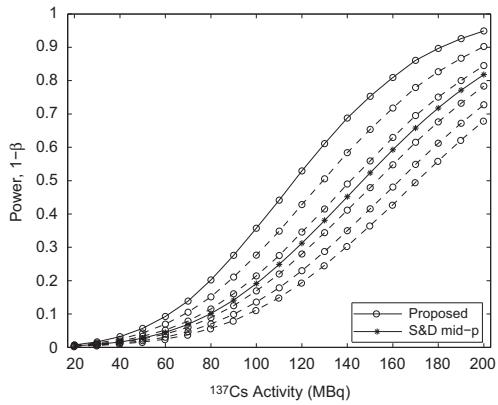

Fig. 2. Actual true positive rates, $1-\beta$, as a function of the ^{137}Cs activity, for a range of p_i parameter values. The mid-p version of Sumerling and Darby's test is also given, for reference. Top curve (solid line, circles): $\mathbf{p} = \{1.0,0\}$, then in steps of 0.1 (dashed lines, circles) to bottom curve (dashed line, circles) $\mathbf{p} = \{0.5,0.5\}$.

positive rates (cf. Table 2). As shown in Fig. 1 the proposed method has a higher power than the reference methods, for all levels of signal (activities) added.

Fig. 1 shows a best-case scenario for the special case $k=2$; that is, all ^{137}Cs pulses are placed in the first bin. This is favourable for the proposed method. However, and as described in the likelihood ratio test section (Section 2.6.2), it is not an unrealistic scenario. The effect of different signal probabilities, i.e. different $\boldsymbol{p}$, is shown in Fig. 2. As can be seen in Fig. 2, the power of the proposed method is higher than that of the S&D mid-p version as long as 70% or more ($p_1 \geq 0.7$) of the ^{137}Cs pulses are placed in the first bin. For values of p_1 below this critical level the proposed method performs worse than the methods testing for $H_0^{(S)}$ alone. This can be understood by considering that the proposed method is using the one-sided likelihood ratio test. This test, as shown in Eq. (30), is sensitive to a higher proportion of the total pulses in the first bin than the second. Cases where this is not true (50% if $\boldsymbol{p}=(0.5,0.5)$) are therefore ignored by the proposed method.

5. Conclusions

This work has presented a novel method consisting in combining counts of pulses with spectral distribution of pulses. The proposed method showed an acceptable false positive rate (α'), in relation to the given α, and good power ($1-\beta$), when compared with the reference methods. It is fast to use, with linear complexity in relation to the number of channels used.

Acknowledgements

The authors would also like to thank an anonymous reviewer for insightful suggestions and comments, especially concerning the single-channel on/off problem. This work was supported by the Swedish Radiation Safety Authority, SSM.

References

[1] J.L. Alvarez, Health Physics 93 (2) (2007) 120.
[2] A. Agresti, A. Gottard, Statistical Science 20 (4) (2005) 367.
[3] A. Agresti, A. Gottard, Computational Statistics & Data Analysis 51 (12) (2007) 6447.
[4] S. Baker, R.D. Cousins, Nuclear Instruments and Methods in Physics Research Section A 221 (2) (1984) 437.
[5] R.J. Barlow, Statistics: A Guide to the Use of Statistical Methods in the Physical Sciences, first ed., John Wiley & Sons, Ltd., New York, 1989.
[6] R.D. Cousins, J.T. Linnemann, J. Tucker, Nuclear Instruments and Methods in Physics Research Section A 595 (2) (2008) 480.
[7] R.D. Cousins, K.E. Hymes, J. Tucker, Nuclear Instruments and Methods in Physics Research Section A 612 (2) (2010) 388.
[8] N. Cressie, T.R.C. Read, International Statistical Review 57 (1) (1989) 19.
[9] L.A. Currie, Analytical Chemistry 40 (3) (1968) 586.
[10] L.-E. De Geer, Applied Radiation and Isotopes 61 (2–3) (2004) 151.
[11] R.A. Fisher, Statistical Methods for Research Workers, fourth ed., Oliver and Boyd, London, 1932.
[12] Health Physics Society, Performance Criteria for Radiobioassay, An American National Standard, ANSI/HPS N13.30-1996, American National Standards Institute, New York, USA, 1996.
[13] U. Keich, N. Nagarajan, Journal of Computational and Graphical Statistics 15 (4) (2006) 779.
[14] H.O. Lancaster, Journal of the American Statistical Association 56 (294) (1961) 223.
[15] L. Méray, Nuclear Instruments and Methods in Physics Research Section A 353 (1–3) (1994) 272.
[16] L. Méray, O. Demény, Applied Spectroscopy 55 (8) (2001) 1102.
[17] N. Nagarajan, N. Jones, U. Keich, Bioinformatics 21 (Suppl. 1) (2005) 311.
[18] W.E. Potter, Journal of Radioanalytical and Nuclear Chemistry 263 (2) (2005) 321.
[19] D.J. Strom, J.A. MacLellan, Health Physics 81 (1) (2001) 27.
[20] T.J. Sumerling, S.C. Darby, Statistical Aspects of the Interpretation of Counting Experiments Designed to Detect Low Levels of Radioactivity, National Radiological Protection Board (NRPB); NRPB-R113, Chilton, UK, 1981.
[21] S.S. Wilks, The Annals of Mathematical Statistics 9 (1938) 60.

Paper III

Journal of Environmental Radioactivity 102 (2011) 605–613

Contents lists available at ScienceDirect

Journal of Environmental Radioactivity

journal homepage: www.elsevier.com/locate/jenvrad

Comparison of airborne and terrestrial gamma spectrometry measurements - evaluation of three areas in southern Sweden

Peder Kock*, Christer Samuelsson

Department of Medical Radiation Physics, Clinical Sciences, Lund University, University Hospital, SE-221 85 Lund, Sweden

ARTICLE INFO

Article history:
Received 13 December 2010
Received in revised form
2 March 2011
Accepted 17 March 2011
Available online 9 April 2011

Keywords:
Airborne gamma spectrometry
Mobile gamma spectrometry
Background radiation
Potassium
Uranium
Thorium

ABSTRACT

The Geological Survey of Sweden (SGU) has been conducting airborne gamma spectrometry measurements of natural radioactivity in Sweden for more than 40 years. Today, the database covers about 80% of the country's land surface. This article explores the first step of putting this data into use in radioactive source search at ground level. However, in order to be able to use the airborne background measurements at ground level, SGU data must be validated against terrestrial data. In this work, we compare the SGU data with data measured by a portable backpack system. This is done for three different areas in southern Sweden. The statistical analysis shows that a linear relationship and a positive correlation exist between the air and ground data. However, this linear relationship could be revealed only when the region possessed large enough variations in areal activity. Furthermore, the activity distributions measured show good agreement to those of SGU. We conclude that the SGU database could be used for terrestrial background assessment, given that a linear transfer function is established.

1. Introduction

When searching for radioactive sources using mobile in-situ gamma spectrometry, the background from naturally occurring radionuclides in the ground and in air (radon) can pose a challenge. Geology, topography, soil density and moisture as well as the detector itself are some of the parameters affecting the gamma radiation field. Apart from these inherent challenges the mobile gamma spectrometry platform is moving through the terrain, constantly sampling from a more or less unknown background. Research has been conducted in the field since the dawn of portable gamma spectrometers and numerous methods exist to separate the background from the sources of interest, in real-time (e.g. Cresswell and Sanderson, 2009; Hjerpe and Samuelsson, 2003; IAEA, 2003; Kock et al., 2010).

Airborne gamma spectrometry (AGS) is a swift and effective technique when broad geographic regions must be surveyed. Its applications include mineral exploration (Smith, 1985), geological mapping (Zhang et al., 1998), environmental assessment and assessment of uranium mine site rehabilitation (Bollhöfer et al., 2008; Martin et al., 2006), fallout mapping (Mellander, 1998) and radioactive source search (Cresswell and Sanderson, 2009; Ulvsand et al., 2003). If the survey area is small, ground based mobile gamma spectrometry can be a good alternative or complement to AGS. Having the detector close to the ground gives a much better spatial resolution. This field of view difference for the two techniques is also a factor that makes comparisons between the two less straight forward.

Most of the studies found in the literature, comparing measurements conducted by AGS to ground measurements, focus on either ^{137}Cs or dose rate comparisons, while comparisons made on the natural radiation background are rare. Comparisons between AGS and ground measurements in various forms are discussed in detail with respect to; soil sampling (Tyler et al., 1996), in-situ measurements (Bucher et al., 2000; Sanderson et al., 1995; Tyler et al., 1996) and kerma rates (Bargholz and Korsbech, 1997). International exercises including RESUME-95 and 99, RADMAGS and ECCOMAGS have also been undertaken in Europe, where ground to air comparisons, mainly for ^{137}Cs, are discussed and evaluated (Hoovgaard and Scott, 1997; Mellander et al., 2002; Sanderson et al., 2003, 2004).

Hoovgaard and Scott (1997) pointed out that a linear relationship between terrestrial and airborne measurements allows the possibility of scaling between the different sets. Sanderson et al. (2003) compared carborne ^{137}Cs measurements to airborne and found generally low R^2-values, with intercepts and scale factors significantly different from 0 to 1 respectively. However, they also compared ^{137}Cs activity and dose rates from in-situ measurements to AGS, which produced an excellent agreement between the two. Mellander et al. (2002) and Sanderson et al. (2003) found that the carborne measurements underestimated activity with about 50% to

* Corresponding author. Tel.: +46 703325448; fax: +46 46 127 249.
E-mail address: peder.kock@med.lu.se (P. Kock).

0265-931X/$ – see front matter © 2011 Elsevier Ltd. All rights reserved.
doi:10.1016/j.jenvrad.2011.03.010

those of AGS. This was explained by differences in the field of view and with the influence of roads.

Having a high quality background database opens up new possibilities in mobile radioactive source search. Because of the (stochastic) natural background fluctuations and (systematic) environmental features it can be difficult to distinguish between a natural anomaly and an anthropogenic. Alarm algorithms tuned to detect anomalies typically suffer from so called type I (false positives) and type II (false negatives) errors (Barlow, 1989). A priori knowledge of the search area's activity distribution could, if properly incorporated in the alarm method, reduce the number of false alarms due to localised features and thus improve the search efficiency.

Airborne measurement campaigns measuring ^{40}K, ^{238}U and ^{232}Th have been carried out in Sweden since the late 1960's by the Geological Survey of Sweden (SGU). Today, SGU's database contains background data for about 80% of Sweden's area. Apart from its commercial and research applications, outlined above, this data cache offers potential a priori knowledge about the natural radiation background that could be used in mobile search operations at ground level, as recognized by IAEA (1990). However, before using the database in such a context it must be validated against terrestrial data. This article compares the AGS data to ground based measurements for three test areas in southern Sweden.

2. Survey sites

The Geological Survey of Sweden started their airborne gamma radiation measurements in the late 1960's, mainly to map uranium deposits. To this day SGU has potassium, uranium and thorium data for about 80% of Sweden, mainly excluding the mountain range along the Norwegian border. The grid consists of flight lines, flown during the snow-free season at 30–60 m altitude with 200–800 m line spacing. Data in the database are available as (radon stripped) concentrations along the flight lines. After the Chernobyl accident in 1986 SGU also mapped ^{137}Cs fallout (Mellander, 1998). However, radiocaesium will not be considered in this work.

Uranium (^{238}U) is measured through the radon daughter ^{214}Bi (1730 + 1765 keV, 18%) in its decay chain, while thorium (^{232}Th) is measured through ^{208}Tl (2614 keV, 99%) in its decay chain. Potassium (^{40}K) is measured directly at 1461 keV (11%). In geological surveys it is conventional to assume secular equilibrium in the decay chains of ^{238}U and ^{232}Th and report the results as equivalent uranium (eU) and equivalent thorium (eTh).

Three test areas were chosen for their different background compositions (Fig. 1). Table 1 summarise the basic characteristics and statistics for the three test areas. Apart from the different background levels between the areas, K, eU and eTh also vary significantly within some of the areas. An estimate of the area's variability is the Coefficient of Variation (CV), also given in Table 1.

Area I at Revingehed (N55°41.280′, E13°30.350′), located 15 km east of Lund, was chosen for its homogeneous and low background levels. The geology consists of sedimentary rocks with a flat topography. Especially U and Th are unusually low here in a Swedish context (compare Table 1 to UNSCEAR (2000)). Any ground-to-air comparisons made for these both radionuclides within this area will suffer from bad statistics due to the low count rates.

Within area II, located at Andrarum (N55°43.017′, E13°59.094′) some 50 km east of Lund, the U-component varies strongly due to

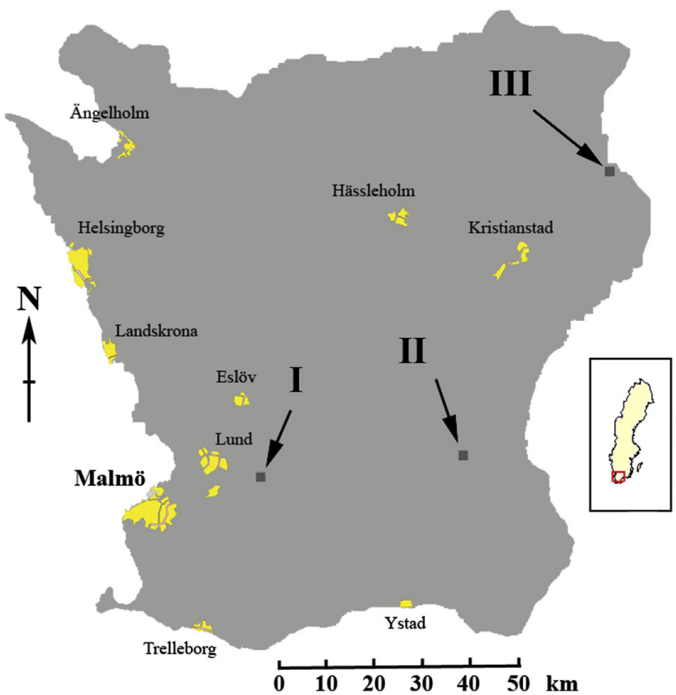

Fig. 1. Map over Scania (Skåne), the southernmost region of Sweden. Major urban areas and the three survey areas (I–III) are marked on the map.

Table 1
Summary characteristics and statistics for the three survey areas.

	Area I			Area II			Area III			Unit
Area	1.02			0.54			0.42			km^2
Flight height	62.5			57.2			30			m
AGS samples	449			203			76			–
AGS samp. time	250			250			400			ms
Ground samples	2362			2325			1327			–
Ground samp. time	9			9			9			s
	Mean	SD	CV(%)	Mean	SD	CV(%)	Mean	SD	CV(%)	
AGS ^{40}K	446.5	124.3	27.9	504.9	228.6	45.3	722.5	252.4	34.9	Bq kg^{-1}
AGS eU	10.5	12.1	115.0	113.7	155.1	136.5	167.9	62.5	37.2	Bq kg^{-1}
AGS eTh	11.6	7.3	62.7	21.3	15.3	72.0	73.0	23.3	31.9	Bq kg^{-1}
Ground ^{40}K	3.19	0.98	30.7	5.12	1.90	36.9	5.81	2.29	39.5	Counts s^{-1}
Ground eU	0.12	0.30	251.2	1.38	2.38	172.9	0.60	0.86	143.5	Counts s^{-1}
Ground eTh	0.21	0.23	110.4	0.36	0.33	90.9	1.94	1.13	58.1	Counts s^{-1}

the presence of uranium-rich alun shale in the south-western part of the area. Area II also includes a small lake (Verkasjön) and some slag heaps from an old mine which further increases the background variation within the area. A small stream gorge (Verkaån) crosses the area which is otherwise flat.

Area III is located west of Jämshög (N56°13.240′, E14°27.068′), some 100 km north-east of Lund, where granite gneisses start to dominate the geology. The background radiation level is generally increased and locations with exposed rock and large boulders give raise to some fluctuations. The topography is mainly flat with the exception of a slope in the western part of the area.

3. Methodology

3.1. Statistical analysis

Rather than direct comparison of activities per unit mass, we compare the net counts from the terrestrial platform with the given concentrations from SGU. Both terrestrial and AGS survey data sets are gridded onto a 50 × 50 grid using a triangle-based linear interpolation algorithm; GRIDDATA, found in MATLAB.[1] The interpolation fits the data onto a non-smooth surface, thus the first derivative may have discontinuities.

The two surfaces (AGS and ground level) are then compared through their normalised distribution functions. This comparison shows the overall agreement of normalised data. Especially non-normal distributions are interesting, since it is an indication of localised high (compared to the surroundings) activity concentrations. However, studying the distribution functions does not give any information on the spatial correlation.

3.2. Linearity and spatial correlation

The linearity and spatial correlation are instead investigated in a scatter plot. As mentioned above, the field of view of the detectors differs significantly between the two data sets. The ratio between the areas covered by an airborne detector to the backpack detector is typically about 10^3 (Tyler et al., 1996). In order to account for the different field of views between the ground and air surveys a method to upscale the ground survey data is presented.

Instead of using the GRIDDATA interpolation, a circle is constructed around each AGS sample with a radius corresponding to 90% of the primary photon fluence, assuming a semi-infinite depth distribution and azimuthal symmetry. The fraction of the total primary photon fluence, $\phi_f(\theta, E)$, at a detector at height h above the ground plane is

$$\phi_f(\theta, E) = \frac{1}{E_2(\mu_a h)} \int_0^\theta \sin\varphi \exp(-\mu_a h \sec\varphi) \mathrm{d}\varphi \quad (1)$$

where θ is the angle from the ground normal, h the height above ground, μ_a the linear attenuation coefficient in air (Finck, 1992) and

$$E_2(x) = x \int_x^\infty t^{-2} \exp(-t) \mathrm{d}t \quad (2)$$

is the second-order exponential integral. The 90% angle is obtained by solving for θ

$$\phi_f(\theta, E) = 0.9 \quad (3)$$

Now the 90% radius is simply

$$r = h \tan\theta \quad (4)$$

This procedure is repeated for $E = 1461$, 1765 and 2614 keV, thus obtaining three radii for each AGS sample. Fig. 2 shows solutions to the integral (1), presented as horizontal distances (Eq. (4)), for the

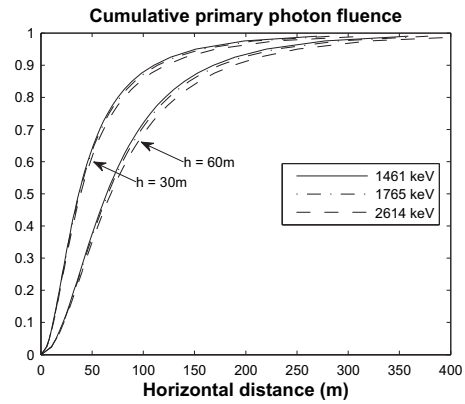

Fig. 2. Cumulative primary photon fluence for a uniform depth distribution as a function of the horizontal distance (r). The two heights, 30 m (three upper curves) and 60 m (three lower curves), correspond to the mean flight heights used in the AGS surveys.

[1] MATLAB is a software package produced and supported by The MathWorks, Inc, Natick, MA, USA.

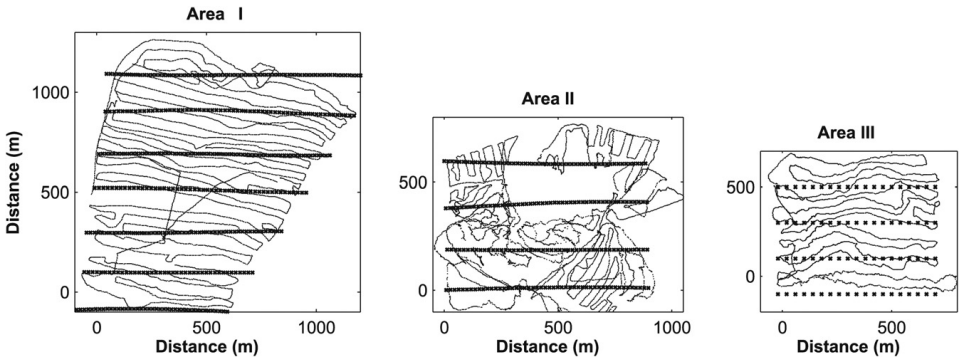

Fig. 3. Plot of sample points for the three survey areas. Flight lines are seen as horizontal (east-western) bold markers while the ground surveys are plotted with small dots. Note the lake within area II, which can be seen indirectly as the area lacking terrestrial samples.

three energies given above and the two typical AGS heights used in this work.

The results of the measurements conducted on ground within the calculated circle, u_i, are then summed together using inverse distance weighting

$$u(x) = \sum_{i=0}^{n} \frac{w_i(x)}{\sum_{j=0}^{n} w_j(x)} u_i \tag{5}$$

where

$$w_i(x) = \frac{1}{d(x, x_i)} \tag{6}$$

is the weighting function, $d(x, x_i)$the distance between the AGS point, **x**, and a sample point on the ground, x_i (Shepard, 1968).

3.3. Statistical uncertainties

Unfortunately no measurement uncertainties are given in the SGU database. For the ground samples the uncertainty can be derived from the poisson standard deviations in the estimated net counts, i.e.

$$\sigma_i = \sqrt{N + B\left(1 + \frac{n}{2m}\right)} \tag{7}$$

where N is the net count, B the subtracted background count from m channels on either side of the region of interest, which is n channels wide (Gilmore, 2008). Assuming that no errors reside from the position acquisition, the weighted sample mean $u(x)$, defined in Eq. (5), has a standard deviation of

$$\sigma_u(\bar{x}) = 2\sqrt{\sum_{i=0}^{n} \omega_i^2 \sigma_i^2} \tag{8}$$

where

$$\omega_i = \frac{w_i(x)}{\sum_{j=0}^{n} w_j(x)} \tag{9}$$

is the total weight factor applied to sample i. Eq. (8) gives the total counting statistical uncertainty ($k = 2$) of the weighted sample mean, with a level of confidence of approximately 95%.

3.4. Data sampling

The AGS surveys, shown in Fig. 3, contains data from lines flown at heights of about 60 m (area I and II) and 30 m (area III), with 200 m linespacing. Area I–II was surveyed in 1996, while the data from area III dates back to 1972. Measurement times were 250 ms for area I–III and 400 ms for area III. SGU data from before 1995 (i.e. area III) contains interpolated sample points with 40 m spacing along the flight line. Newer data (i.e. areas I–II) are recorded in the database at their sampling point. The AGS samples were smoothed along the flight lines, doubling the effective sample time to reduce the uncertainty from counting statistics. This was only necessary for the scatter plot analysis, were no interpolation was done on the SGU data set.

The terrestrial backpack survey was done in three stages during 2008–2010. Each area was surveyed during several hours of walking at pace of about 4–5 kmh^{-1}. A new spectrum was recorded to a laptop, which also was carried in the backpack, every 3rd second, giving thousands of spectra. Along with each spectrum a GPS position was stored. The samples were then smoothed to give 9s samples, thus reducing the statistical counting uncertainty somewhat. Net counts from ^{40}K, ^{214}Bi and ^{208}Tl were evaluated using extended background regions on either side of the peak (Gilmore, 2008). The net count was stored along with two position elements, yielding three xyz data sets from each area.

4. Spectrometry instrumentation

SGU uses a 16.7L NaI(Tl) mounted in a fixed-wing aircraft. The system was calibrated using four concrete pads, each with known concentrations of K, U and Th. The fourth pad is a null pad used for background correction. Unit spectra and stripping ratios were then calculated and used to measure terrestrial K, eU and eTh concentrations, assuming uniform depth distributions as described by the IAEA (IAEA, 1991; ICRU, 1994). At the time when area III was surveyed, SGU used a 6L NaI(Tl), calibrated by the same method. Both systems used an upward looking (currently 4L NaI(Tl)) detector to account for radon in the air.

The NaI(Tl) spectrometry system used in the ground survey is a portable backpack solution. It uses a 3 × 3″ (7.62 × 7.62 cm) cylindrical detector from Saint-Gobain,[2] model no. 3M3/3,

[2] Saint-Gobain Cristaux, 104 Route de Larchant, Nemours, France.

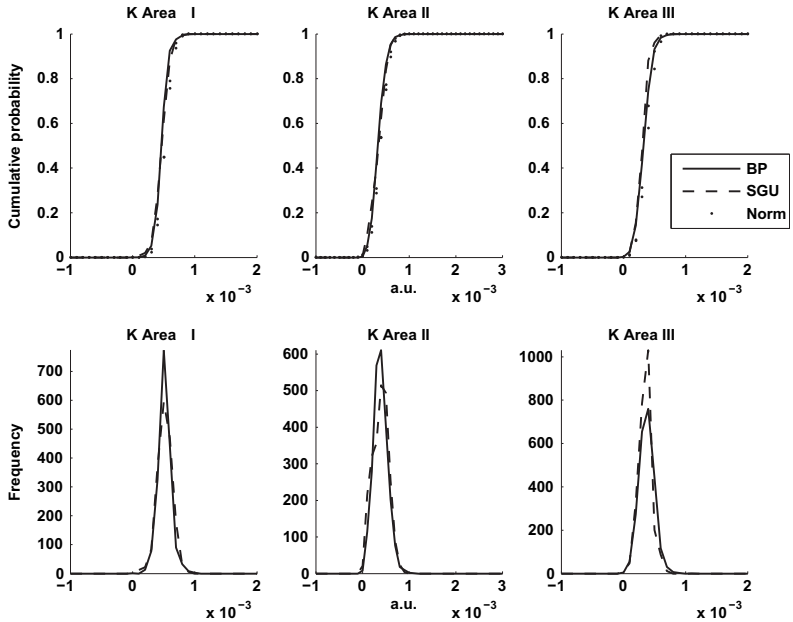

Fig. 4. Normalised sample and cumulative distributions for ^{40}K, areas I–III. Two distributions are presented within each subplot, SGU's AGS (dashed lines) and backpack (BP, full lines). The top graphs also shows the cumulative distribution function of a fitted normal distribution.

equipped with a 14-pin photomultiplier tube, integrated bias supply, pre-amplifier and digital multi-channel analyser manufactured by Ortec (Ortec Digibase). The system was made for field use and assembled by Gammadata.[3]

The backpack was not calibrated for the geometry assumed in this work. Multiplying the net counts from the ground measurements with a calibration-constant does not give any additional information regarding the shape of the statistical distributions or the spatial correlation. Rather, a calibration and absolute comparisons would introduce an additional uncertainty to the comparison. Instead, all ground-to-air comparisons are made on normalised data.

5. Results and discussion

5.1. Statistical distributions

The normalised distributions and cumulative distribution functions (cdf) of activity concentrations and net counts for SGU and backpack respectively are presented for K, eU and eTh in Figs. 4–6. Along with the survey samples a normal distribution fit is presented for comparison. Each bin has been normalised by the total number of samples, thus allowing for direct comparison of the two data sets within each subplot. Table 2 shows sample correlation coefficients (Pearson), r, between the AGS and ground data.

Potassium data in Fig. 4, shows a very good agreement between the two surveys, for all three areas ($r \geq 0.95$). The distributions all have Gaussian shapes which gives no indication of local high activity concentration within any of the three areas. This can also be seen by studying the CV in Table 1, were both potassium rows show modest variability.

When studying the uranium graphs in Fig. 5, a few features immediately stand out, one being the non-Gaussian distribution of U-activity within area II. Still, the ground and air survey distributions showed a good agreement for this area ($r = 0.92$). Area I has a mean close to zero, which is due to the low U-levels within this area (see Table 1). Especially the ground survey suffers from poor statistics, mainly from the background subtraction, which can be seen in the relatively large proportion of the samples with negative values. Area III, however, which shows a much larger distribution width for the backpack, should not suffer from poor counting statistics. The distributions are both normal but the widths were far from equal ($r = 0.68$). This can partly be explained by interference from scattered ^{208}Tl 2614 keV photons to the eU peak (1765 keV). In fact, the backpack distribution fits the SGU data better when plotting gross counts, which is an indication of a failure in the background subtraction. Another possibility is that the higher variability of ground data is due to localised high activity concentrations which are smoothed in the AGS data.[4]

Thorium data, shown in Fig. 6, also show a good agreement with $r \geq 0.9$. All three areas have gauss-like distributions, with slightly wider distributions for the terrestrial survey. Areas I and II have tails of negative values, again due to the relatively low mean activity concentration levels as shown in Table 1.

This analysis generally shows broader distribution peaks for the terrestrial surveys. One should bear in mind that the difference in

[3] Gammadata Instrument AB, Vallong. 1, Uppsala, Sweden.

[4] As suggested by an anonymous reviewer.

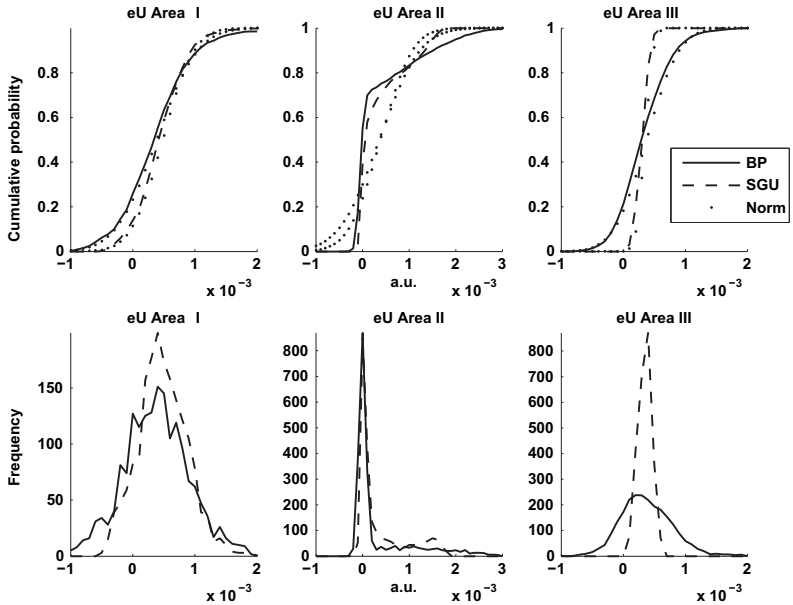

Fig. 5. Normalised sample and cumulative distributions for eU, areas I–III. Two distributions are presented within each subplot, SGU's AGS (dashed lines) and backpack (BP, full lines). The top graphs also shows the cumulative distribution function of a fitted normal distribution.

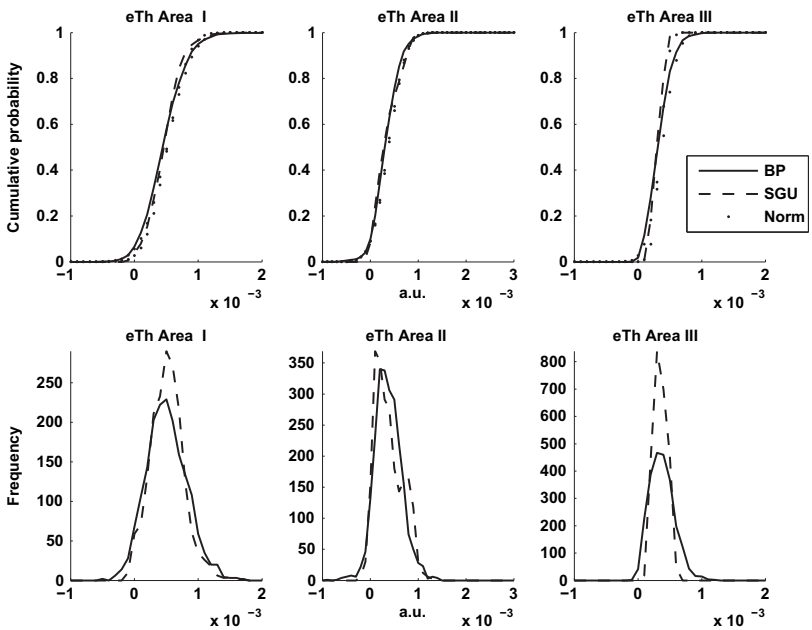

Fig. 6. Normalised sample and cumulative distributions for eTh, areas I–III. Two distributions are presented within each subplot, SGU's AGS (dashed lines) and backpack (BP, full lines). The top graphs also shows the cumulative distribution function of a fitted normal distribution.

Table 2
Sample Pearson correlation coefficients between normalised airborne and normalised ground-based statistical distributions.

	Area I	Area II	Area III
K	0.98	0.95	0.96
eU	0.94	0.92	0.68
eTh	0.97	0.94	0.92

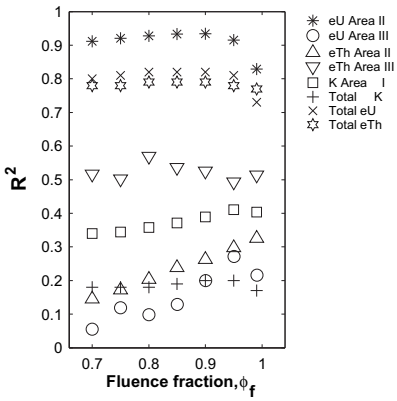

Fig. 7. Coefficient of correlation, R^2, from the scatter plots of AGS and ground based samples, plotted against the fraction of total primary photon fluence. All comparisons, except eTh in area III, show greater R^2-values as the fraction is increased to 90% of the total primary photon fluence.

field of view between the two detectors is not accounted for in this kind of analysis. Hence, the most important result from this analysis is that the general shapes of the distributions are the same. All but one (eU, area II) surveys are well described by a normal distribution, indicating one or many local high activity subareas within that area.

5.2. Spatial correlation and linearity

5.2.1. Field of view

The smoothing technique outlined in the methodology section enables a direct comparison of ground and air measurements. However, the choice of primary fluence fraction, ϕ_f Eq. (3), needs to be explained. In theory, incorporating all measurements from the ground survey in every comparison, i.e. setting the radius r to be infinite, should yield a higher correlation, since all photons then are accounted for and properly weighted. In practice, however, this is not the case, as shown in Fig. 7. The coefficient of determination, R^2, was calculated for fractions of the total primary photon fluence in the range $0.7 \leq \phi_f \leq 0.99$. A value of less than 0.7 resulted in too few ground samples in some cases (especially for area III), why this was set as the lower bound. In Fig. 7 it can be seen that R^2 generally increases as the fraction of total photon increases to about 0.9. This is true for all data sets except eTh in area III, while $\phi_f > 0.9$ shows ambiguous results. The drop at larger values of ϕ_f can be explained by the finite extent of the ground survey. Samples close to the edges of the survey areas will be biased, especially if the radius is too large. As an example, consider an AGS sample in one of the corners of the survey area. The measurement will only have 25% of its photons originating from the survey area, assuming homogeneous activity concentrations. The weighted ground sample will instead, at the same position, have all of its photons originating from the

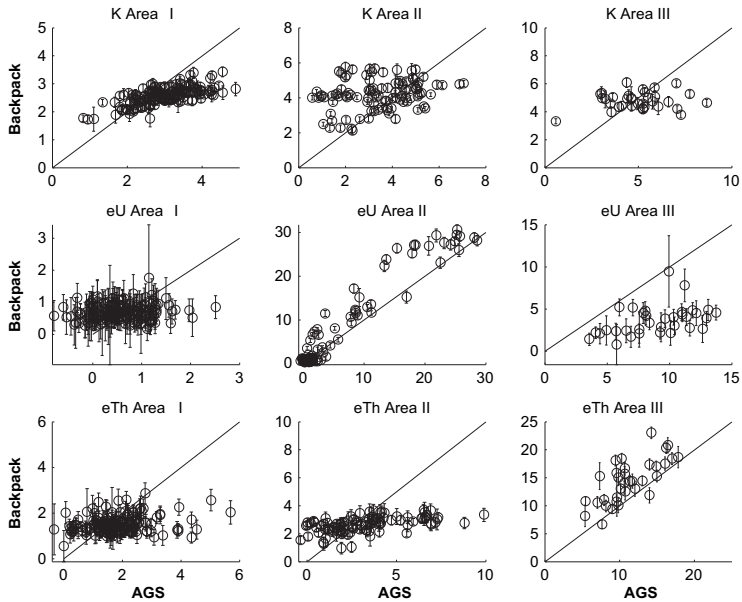

Fig. 8. Scatter plots of ^{40}K, eU and eTh for areas I–III. Normalised backpack count rates (vertical) with uncertainties ($k = 2$) versus normalised AGS concentrations (horizontal). Solid lines, $x = y$, are given in each subplot. Note the relatively large uncertainties in samples from area I compared to areas II–III.

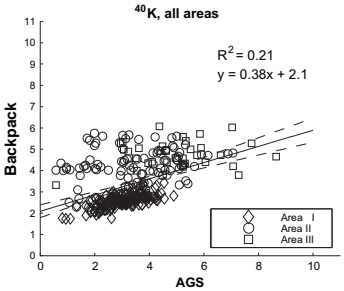

Fig. 9. Scatter plot of normalised ^{40}K samples. Dashed lines show 95% confidence interval for regression line. A weak positive correlation exists, with non-zero intercept and a slope significantly different from unity.

survey area. Therefore, setting the fraction to 0.9 seems to be a reasonable compromise.

5.2.2. Scatter plots

Fig. 8 shows scatter plots with AGS on the horizontal axis and weighted terrestrial data on the vertical axis. Ground data within the 90% radius (Eq. (4)) are weighted as defined in Eq. (5). Vertical uncertainties were then calculated according to Eq. (8). The result were normalised so that a good fit between AGS and terrestrial samples would lie on the straight line $y = x$.

The relative uncertainties of the weighted means, shown in Fig. 8, were generally in the order of a few to tens of percent, with a few exceptions. The uncertainty of each individual sample is greater, but when the samples are weighted and summed the uncertainty of the weighted sample mean drops. Generally, if there are n samples with equal weights and standard deviations, the standard deviation of the mean will decrease with a factor $1/\sqrt{n}$, according to the central limit theorem. Still some uranium samples incorporate the zero level within the given level of confidence (95%). Even though no uncertainties are given by SGU, it is safe to assume that the uncertainties in the AGS samples are at least as great as the ones shown for the terrestrial samples. This is due to the number n, which is equal to one for all AGS samples.

Uranium in area II as well as thorium in area III show a good straight line fit between the two data sets. From the figure one can

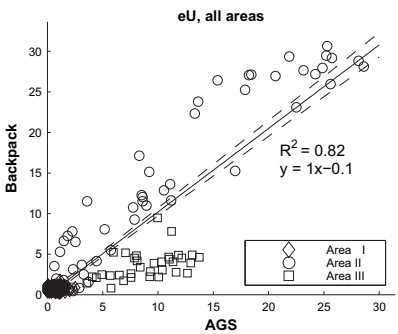

Fig. 10. Scatter plot of normalised eU samples. Dashed lines show 95% confidence interval for regression line. The regression gives unity slope and intercept close to zero, which shows a good agreement between ground and air measurements for eU.

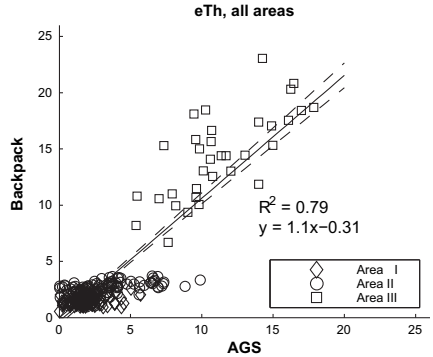

Fig. 11. Scatter plot of normalised eTh samples. Dashed lines show 95% confidence interval for regression line. A strong positive correlation exist, the straight line has an intercept and slope close to zero and unity respectively.

deduce that the mean and variability within the areas decide how good the straight line fit will be. Potassium, for instance, have a relatively small range of activities (which also can be seen in Fig. 4 and Table 1) within all three areas, yielding a poor correlation in the scatter plots.

To better understand the correlation between AGS and terrestrial data, Figs. 9–11 present scatter plots were all measurements from the three areas are presented together. Vertical errors are omitted, to make the figures more readable. Best straight line fits (least square), with 95% confidence intervals, and linear regression analyses R^2-statistic are also given in the figures. Again, the two background components with the largest variability (eU and eTh, Figs. 10 and 11) show strong positive correlations and good straight line fits, with slopes close to one and interceptions close to zero, while potassium (Fig. 9) shows a weak positive correlation.

The regression analysis is dominated by the area with the largest variability. In both Figs. 10 and 11 two clusters with different slopes can be seen. Uranium data from area III exhibit a much smaller slope than eU data from area II, while eTh data from area II exhibit a much smaller slope than eTh data from area III. In both figures the area with the most activity lies above the regression line. Most likely this is an effect due to the field of view difference, discussed above. The sensitivity to local variations are higher in the ground measurements, which reflects in clusters on either side of the $x = y$ line. It is also possible that airborne activity contribute to the ground based measurements, as no radon stripping was done in the terrestrial measurements. The results suggest that the ground data upscaling model presented in this work might fail for a single area, but that it gives satisfactory results if enough variability can be found in the data.

6. Conclusions

This study presents a model for upscaling of ground data to compensate for the field of view difference between AGS and ground data. Using the model we show that spatial ground-to-air correlation analysis on normalised data is feasible. Regression analysis of eU and eTh gave slopes close to one and intercepts close to zero, while ^{40}K only showed a weak positive correlation with slope and intercept significantly different from one and zero, respectively. The results show that the spatial correlation between AGS and ground data is stronger in areas where the activity variability is large; given a large enough mean activity. These areas also tend to be the most

challenging in ground based mobile radioactive source search operations. The strong spatial correlation between AGS and ground data for eU and eTh suggests that a linear transfer function can be established.

We have also shown that comparisons directly between air and ground spectral data can be made using the normalised distributions of the whole area. All but one distribution were normal, while eU in area II contained localised high radiation areas and thus a non-Gaussian distribution. Such non-Gaussian areas are especially problematic when searching for radioactive sources. They could trigger a false alarm of type I, when moving into, or type II, when moving out of, the area in question. Having a distribution shape from AGS data could therefore be part of a prognostic tool, to be used when conducting terrestrial radioactive search operations.

Acknowledgements

The authors wish to thank Sören Byström, Mats Wedmark and Johan Daniels at SGU for their feedback and help with making the SGU database available to us. Thanks also to Jonas Nilsson, Lund University, for his insightful suggestions. This work was supported by the Swedish Radiation Safety Authority, SSM.

References

Bargholz, K., Korsbech, U., 1997. Conversion of airborne gamma ray spectra to ground level air kerma rates. In: Bäverstam, U., Fraser, G., Kelly, G.N. (Eds.), Decision Making Support for Off-site Emergency Management, Proceedings of Fourth International Workshop, Aronsborg, Sweden, October 7–11 1996. Radiat. Prot. Dosimetry 73(1–4). Nuclear Technology Publishing, Ashford, UK, ISBN 1-87096-549-3, pp. 127–130.

Barlow, R.J., 1989. Statistics: A Guide to the Use of Statistical Methods in the Physical Sciences. John Wiley & Sons Ltd., New York.

Bollhöfer, A., Pfitzner, K., Ryan, B., Martin, P., Fawcett, M., Jones, D.R., 2008. Airborne gamma survey of the historic Sleisbeck mine area in the Northern Territory, Australia, and its use for site rehabilitation planning. J. Environ. Radioact. 99, 1770–1774.

Bucher, B., Rybach, L., Schwarz, G., 2000. Environmental mapping: comparison of ground and airborne spectrometry results under alpine conditions. In: Sanderson, D.C.W., McLeod, J.J. (Eds.), Recent Applications and Developments in Mobile and Airborne Gamma Spectrometry. Proceedings of the RADMAGS Symposium, University of Stirling, 15–18 June 1998, SURRC, University of Glasgow.

Cresswell, A.J., Sanderson, D.C.W., 2009. The use of difference spectra with a filtered rolling average background in mobile gamma spectrometry measurements. Nucl. Instrum. Methods Phys. Res. A 607, 685–694.

Finck, R. R., 1992. Doctoral Dissertation. High resolution field gamma spectrometry and its applications to problems in environmental radiology. Departments of Radiation Physics, Malmö and Lund, Lund University. pp. 1–138. Kristianstads boktryckeri, Malmö, Sweden. ISBN: 91-628-0739-0.

Gilmore, G., 2008. Practical Gamma-ray Spectrometry, second ed. Wiley-VCH Verlag, Weinheim.

Hjerpe, T., Samuelsson, C., 2003. A comparison between gross and net count methods when searching for orphan radioactive sources. Health Phys. 84 (2), 203–211.

Hoovgard, J., Scott, E.M., 1997. RESUME-95: results of an international field test of mobile equipment for emergency response. In: Bäverstam, U., Fraser, G., Kelly, G.N., Decision Making Support for Off-site Emergency Management. Proceedings of Fourth International Workshop, Aronsborg, Sweden, October 7–11 1996. Radiat. Prot. Dosimetry 73(1–4), pp. 219–224. Nuclear Technology Publishing, Ashford, UK ISBN 1-87096-549-3.

International Atomic Energy Agency (IAEA), 1990. The use of gamma ray data to define the natural environment. IAEA-TECDOC-566. Vienna, Austria.

International Atomic Energy Agency (IAEA), 1991. Airborne gamma ray spectrometer surveying. Technical Report Series 323. Vienna, Austria.

International Atomic Energy Agency (IAEA), 2003. Guidelines for radioelement mapping using gamma ray spectrometry data. IAEA-TECDOC-1363. Vienna, Austria.

International Commission on Radiation Units and Measurments (ICRU), 1994. Gamma-ray spectrometry in the environment. ICRU Report 53. Maryland, USA.

Kock, P., Finck, R.R., Nilsson, J.M.C., Östlund, K., Samuelsson, C., 2010. A deviation display method for visualising data in mobile gamma-ray spectrometry. Appl. Radiat. Isot. 68, 1832–1838.

Martin, P., Timis, S., Mcgill, A., Ryan, B., Pfitzner, K., 2006. Use of airborne γ-ray spectrometry for environmental assessment of the rehabilitated Nabarlek uranium mine, Australia. Environ. Monit. Assess. 116, 531–553.

Mellander H., 1998. Airborne gammaspectrometric measurements of the fall-out over Sweden after the nuclear reactor accident in Chernobyl, USSR. Swedish Geological Co, Report TFRAP 8803. Uppsala, Sweden.

Mellander, H., Aage, H.K., Karlsson, S., Korsbech, U., Lauritzen, B., Smethurst, M., 2002. Mobile Gamma Spectrometry. Evaluation of the Resume 99 Exercise. NKS-56. NKS, Roskilde, ISBN 87-7893-111-8.

Sanderson, D.C.W., Allyson, J.D., Tyler, A.N., Scott, E.M., 1995. Environmental applications of airborne gamma spectrometry. In: IAEA Technical Committee Meeting on the use of uranium exploration data and techniques in environmental studies. Proceedings of a technical committee meeting. Vienna, Austria 9–12 November 1993, IAEA-TECDOC-827, pp. 71–92. Vienna, Austria.

Sanderson, D.C.W., Cresswell, A.J., Scott, E.M., Lauritzen, B., Karlsson, S., Strobl, C., Karlberg, O., Lang, J.J., 2003. Report on Exercise Data Comparisons. In: An International Comparison of Airborne and Ground Based Gamma Ray Spectrometry. University of Glasgow, ISBN 0-85261-783-6, pp. 9–174.

Sanderson, D.C.W., Cresswell, A.J., Scott, E.M., Lang, J.J., 2004. Demonstrating the European capability for airborne gamma spectrometry: results from the ECCOMAGS exercise. Radiat. Prot. Dosimetry. 109, 119–125.

Shepard, D., 1968. A two-dimensional interpolating function for irregularly-spaced data. In: Proceedings of the 1968 23rd ACM national conference, pp. 517–524.

Smith, R.J., 1985. Geophysics in Australian mineral exploration. Geophysics 50 (12), 2637–2665.

Tyler, A.N., Sanderson, D.C.W., Scott, E.M., Allyson, J.D., 1996. Accounting for spatial variability and fields of view in environmental gamma ray spectrometry. J. Environ. Radioact. 33, 213–235.

Ulvsand, T., Finck, R.R., Lauritzen, B. (Eds.), 2003. NKS/SRV Seminar on Barents Rescue 2001 LIVEX Gamma Search Cell. NKS-54. NKS, Roskilde, ISBN 87-7893-108-8.

UNSCEAR, 2000. Sources and effects of ionizing radiation, volume 1: sources. United Nations scientific committee on the effects of atomic radiation, report to the general assembly, United Nations, New York.

Zhang, Y., Xiong, S., Chen, T., 1998. Application of airborne gamma-ray spectrometry to geoscience in China. Appl. Radiat. Isot. 49, 139–146.

Paper IV

On Background Radiation Gradients - The use of Airborne Surveys when Searching for Orphan Sources using Mobile Gamma-ray Spectrometry

Peder Kock*, Christopher Rääf, Christer Samuelsson

Medical Radiation Physics, Department of Clinical Sciences Malmö, Lund University, Skåne University Hospital Malmö, SE-205 02 Malmö, Sweden

Abstract

Systematic background radiation variations can lead to both type I and II errors when searching for orphan sources using car-borne mobile gamma-ray spectrometry. The stochastic variation at each point is well described by Poisson statistics, but when moving in a background radiation gradient the mean count rate will continually change, leading to inaccurate background estimations. Airborne gamma spectrometry (AGS) surveys conducted on the national level, usually in connection to mineral exploration, exist in many countries. These data hold information about the background radiation gradients which could be used at the ground level.

This article describes a method that aims to incorporate the systematic as well as stochastic variations of the background radiation. We introduce a weighted moving average where the weights are calculated from existing AGS data, supplied by the Geological Survey of Sweden. To test the method we chose an area with strong background gradients, especially in the thorium component. Within the area we identified two roads which pass through the high-variability locations. The proposed method is compared with an unweighted moving average. The results show that the weighting reduces the excess type I errors in the positive background gradients without introducing an excess of type II errors during passage in negative gradients.

Keywords: Airborne, Background Radiation, Orphan source, Mobile gamma spectrometry

1. Introduction

In mobile gamma-ray spectrometry, systematic changes in the background components can be a great challenge, e.g. when searching for orphan sources [1–3]. The possibility to use airborne gamma spectrometry (AGS) records as background estimates at the ground level has been suggested [4]. In a study conducted in areas with highly variable background levels comparing terrestrial and airborne spectra, a strong correlation between terrestrial and AGS measurements was shown [5]. Areas with high variability are also expected to cause more false positives (type I errors) than more homogeneous areas. Thus, background estimations based on AGS data should be useful in high-variability areas, where the data expects to correlate well.

Statistical hypothesis testing is a common way to indicate increased levels of radioactivity [6–8]. Ideally, a method should have a false alarm rate close to the predefined rate, α, and high power, $1 - \beta$, where β is the probability of a false negative (type II error). Different methods exist that can be used when searching for orphan sources, e.g. [1–3, 9, 10]. Strom and McLellan compared false alarm rates of eight statistical tests and found that many of these deviated from the predefined false alarm rate [8]. In a recent study we incorporated the information from the spectral distribution of the gamma counts and found that this increased the true positive rate, i.e. power, of the test [11].

When entering an area with a positive background radiation gradient without any *a priori* knowledge one would expect an excess of false positives, compared to the predefined level of significance, α. Trying to assess the background while moving in the gradient by means of, for example, a moving background (MB) [9], would mean that the background estimate is always too small compared to the background acquired at the current position. Analogously, while moving in a negative gradient, i.e. decreasing levels of background radiation, one

*Corresponding author (P. Kock)
Tel.: +46 40 33 86 64 peder.kock@med.lu.se

would expect an increase in the number of false negatives, i.e. a lower power of the test, $1 - \beta$.

One method to estimate the height of a peak is to use a trapezoidal formula [12]. This method, which is mostly applied to high-resolution spectra, uses a background region on either side of an isolated peak and assumes a linear background under the peak [13]. The trapezoidal method can also be used in mobile gamma-ray spectrometry to estimate the net counts in a region of interest [5]. Another common technique, mostly used with low-resolution spectrometers, is the spectral windows method where a stripping matrix is used to subtract the contributions from K, eU and eTh [14, 15]. Both methods estimate the background from the spectrum itself, which can be problematic in mobile gamma-ray spectrometry considering the short sampling times needed to attain good spatial resolution. The alternatives are to estimate the background from the latest n samples, e.g. by means of a moving average [2, 3, 9], or to use a previously measured set [7].

Many countries have AGS capabilities, cf. refs. [16–21], and have conducted baseline surveys, often in connection to mineral exploration. This work aims to explore the use of existing AGS measurements, which incorporate the systematic variations, along with statistical methods that handle the stochastic fluctuations. When searching for orphan sources, the combination of these methods could be used to avoid or at least reduce the number of additional false positives while in a positive gradient, and potentially increase the power of a test while in a negative gradient.

2. The Survey area

An area (9×9 km^2, centre N 56° 15.379', E 14° 13.769') in the southern part of Sweden (Scania, *sv.* Skåne) with strong gradients in the background radiation was identified by studying AGS data supplied from the Geological Survey of Sweden (SGU). The area is rural, covered by forest with a few small villages and dwellings connected with asphalt or gravel roads. Several small lakes as well as part of a larger lake (Immeln) are within the bounds of the area. However, the lakes are too far away from any road (>200 m) to influence the measurements of this study. The general topography is flat, but some hills rise as high as 30-40 m above the surroundings.

As can be seen in Fig. 1, the variations are largest in the eTh and eU components, while ^{40}K activity shows a more modest variation. An area extending in the north-northeast direction located in the middle of the figure

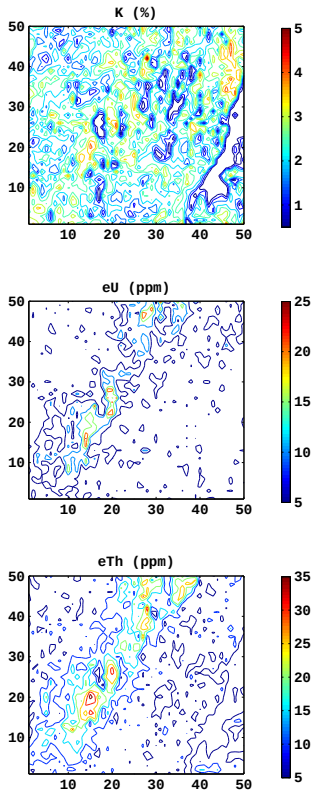

Figure 1: Contour plots of interpolated AGS data on a 50×50 grid (cell size 180×180 m^2).

shows increased eTh concentrations up to a factor 6-7 times those of the surroundings. The chosen area is well suited to test methods that account for systematic changes in the background radiation, since it has such a distinct subarea with elevated background radiation levels. The chosen area is also crossed by a number of roads, making it suitable for car-borne gamma spectrometry (CGS) surveys. In Fig. 2, two excerpts from the roads within the area are marked, henceforth referred to as 'route I' and 'route II'. Both pass through the area with increased eTh levels extending in the north-northeast direction of the area.

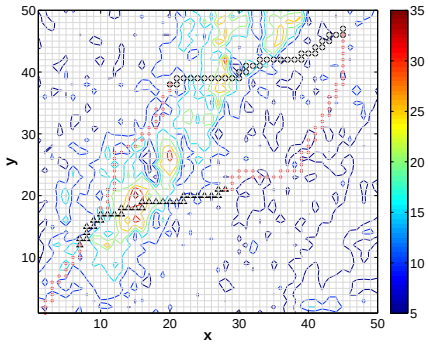

Figure 2: Contour plot of interpolated AGS eTh data (given in ppm) on a 50×50 grid (cell size 180×180 m^2). Triangles (route I) and circles (route II) mark the two CGS excerpts which pass through the area with elevated eTh levels. The rest of the roads are plotted with red dots.

3. Materials and Methods

3.1. Spectrometers and positioning

The Swedish Radiation Safety Authority (SSM) has three pickup vans equipped for conducting CGS surveys. One of the vans is currently stationed at the department in Malmö and available for this research project. The van holds 2×4 L NaI(Tl) crystals, mounted on a rail system which is suspended on the roof of the rear compartment of the van. The rail system offers positional flexibility, but in the present work the detectors were fixed as far away from each other as possible, one at the left side of the van and the other at the right side of the van. The detector signals of the two systems were summed in the post processing so that the effective detector volume was 8 L in this study.

In the centre of the rear compartment of the van there is also a slot for a high-purity germanium (HPGe) detector. However, for this study a $LaBr_3$:Ce (7.62×7.62 cm^2) detector was placed in the slot instead. This choice eliminates the need for liquid nitrogen while keeping a detector able to identify all gamma lines of interest. The vehicle speed was kept around 30 km h^{-1} and the sampling time was 1 s.

The AGS data used in this study was supplied by the SGU. The airborne survey of the area shown in Fig. 1 consists of 9856 spectra sampled in 1972. At the time SGU used a 6 L NaI(Tl) and a flight height of 30 m in the rural areas. The measurement time of the system was 400 ms. For a more detailed description of the system, cf. ref. [5].

3.2. Ground to air comparisons

In a previous study we showed that the normalised distribution functions of AGS and ground data were similar [5]. In the same study we also showed a linear relationship between the normalised airborne and terrestrial data sets, with a slope close to unity and an intersection close to zero, given enough activity variability. Based on these results we expect the normalised CGS data, $f(x, y)/C$, to be directly proportional to the normalised AGS measurements, or

$$\left(\frac{f(x,y)}{C}\right)_{\mathrm{CGS}} = \kappa \left(\frac{f(x,y)}{C}\right)_{\mathrm{AGS}} \tag{1}$$

where κ is a proportionality constant, $f(x, y)$ the expected counts at position (x, y) and C are normalisation factors of each data set.

3.3. Accounting for the systematic component

Gradients in the natural background can be detected using step detection, which is the one-dimensional equivalent to edge detection commonly used in image analysis. The step, i.e. the gradient, is the first derivative, which for a one-dimensional discrete function, f, can be approximated by

$$f'(t) = \frac{d\,f(t)}{d\,(t)} \approx f(t+1) - f(t) \tag{2}$$

where $f(t)$ is the functional value at time t.

Note that each sample $f(t)$ can be a compound value, for instance an interpolated cell value in a grid. Interpolation is generally required in order to use the data, since most AGS surveys are conducted using flight lines [22, 23]. Noise in the data will lead to strong fluctuations in the first derivative. To reduce the noise $f(t)$ can be smoothed, for instance using convolution with a Gaussian kernel or by forming a moving average. Along with the option to use of a threshold value, T, for which values $|f'(t)| < T$ are ignored, even noisy data like those in mobile gamma-ray spectrometry contain useful information in the first derivative.

3.4. Reducing false alarms

Modifying the background estimate at the ground level by considering $f'(t)$ values derived from (normalised) AGS data is a way to account for background gradients. We propose a modification based on the moving average (MA) statistic

$$\mathrm{MA}_N = \frac{1}{N} \sum_{k=t-N}^{t-1} C_k \tag{3}$$

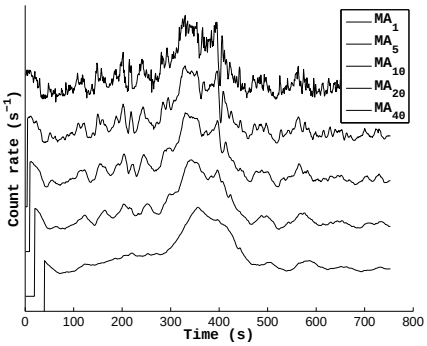

Figure 3: Illustration of the effect of different moving average lengths, N, for $N = 1$ (top) to $N = 40$ (bottom). The graphs are separated by a constant, for readability. Apart from the smoothing effect, note also how the peak position shifts as the averaging length is increased.

where the moving average is formed from the latest N histories and C_t are the counts in the region of interest at time t. The effect on MA_N from different averaging lengths, N, can be seen in Fig. 3.

The proposed alternative, henceforth referred to as MA_N^w, is to weight the CGS background based on the AGS step function, $f'(t)_{\mathrm{AGS}}$, cf. Eq (2). Rewriting Eq. (3) using weights, w_t, the moving average becomes

$$\mathrm{MA}_N^w = \frac{1}{N}\sum_{k=t-N}^{t-1} C_k + w_k \tag{4}$$

The weights, w_t, will be a function of $f'(t)_{\mathrm{AGS}}$, chosen appropriately. In this study the weights were chosen according to

$$w_t = 2\, s_{\mathrm{MA}} \cdot f'_{\mathrm{AGS}} \tag{5}$$

That is, we add a value to C_t which depends on $f'(t)_{\mathrm{AGS}}$ and the standard deviation, s_{MA}, of the N samples that comprise MA_N. The weights, w_t, does not necessary sum to zero for a given path, but should be close to zero when the path starts and ends in areas with similar background radiation levels. No threshold value, T, was used in Eq. (5). Instead we smoothed f'_{AGS} by forming a moving average with $N = 10$. Since the AGS data used in f'_{AGS} are already interpolated, the fluctuations of the step function will be quite moderate.

The field of view of consecutive measurements, $C_{t-N}, \ldots, C_{t-1}$, will overlap, hence the samples cannot be expected to be completely uncorrelated when the background radiation levels change [7]. The samples, C_t, will be autocorrelated leading to an underestimation of the variance, s^2_{MA}. To account for this bias a correction factor, $1/\gamma$, can be applied to s^2_{MA}, where

$$\gamma = 1 - \frac{2}{N-1}\sum_{k=1}^{N-1}\left(1 - \frac{k}{N}\right)\rho(k) \tag{6}$$

$\rho(k)$ is the autocorrelation function (ACF) and N is the sample size [24]. Since the autocorrelation cannot be estimated without introducing an additional source of bias, it has to be analytically known. Here, we simply assume that the ACF follows the geometric model

$$\rho(k) = (1-q)^k \tag{7}$$

where $1 - q$ is the initial value and k the time lag, cf. Eq. (6). Throughout this study q was set to 0.3, modelling a strong correlation for small k ($\rho(1) = 0.7$) which then decreases ($\rho(10) = 0.03$). Even though $\sqrt{1/\gamma}\cdot s_{\mathrm{MA}}$ might not be an unbiased estimate of the standard deviation, much of the bias due to autocorrelation should be removed.

To compare the false positive rates of the different moving averages we calculate an upper 95 % prediction interval endpoint, $U_{1-\alpha}$, for the next sample using the mean, MA_N, and sample standard deviation, s_{MA}, of the N samples in MA_N

$$U_{1-\alpha} = \mathrm{MA}_N + \sqrt{1 + \frac{1}{N}}\, T_{\alpha,N-1} \cdot s_{\mathrm{MA}} \tag{8}$$

where $T_{\alpha,\nu}$ is the 100(1-α)th percentile of the Student's t-distribution with ν degrees of freedom [25]. For this study α was set to 5 % (one-sided). Hence, assuming a normal distribution, 5 % of the times the next sample would be expected to be greater than $U_{0.95}$. To reduce the uncertainty in MA_N, N was set to 40 throughout this study. Thus, since both α and N were fixed, the factor in front of s_{MA} in Eq. (8) was constant: $\sqrt{1 + 1/40} \cdot T_{0.05,39} = 1.706$.

By substituting $\sqrt{1/\gamma} \cdot s_{\mathrm{MA}}$ for s_{MA} in Eq. (8), the reduced-bias standard deviation estimator, cf. Eq. (6), is used instead. Moving averages using this test will have a superscript of γ, e.g. $\mathrm{MA}_N^{w,\gamma}$.

The moving average model presented in this study modifies the background based on eTh data measured by AGS. As described above, and as can be seen in Fig. 1, the variations within the studied area are largest in the thorium component. Even though ^{40}K may still, at least on the average, dominate the background within the area, the eTh variation presents the largest challenge as its variability is greater. Thus, this study focuses on

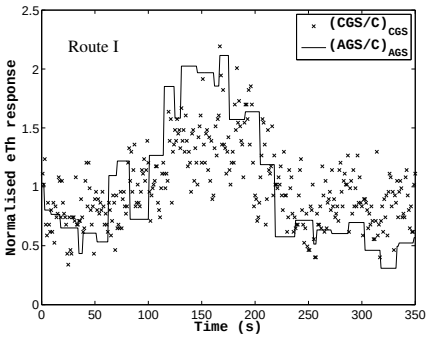

Figure 4: Normalised responses for eTh for AGS and CGS data along route I. CGS time given on the horizontal axis.

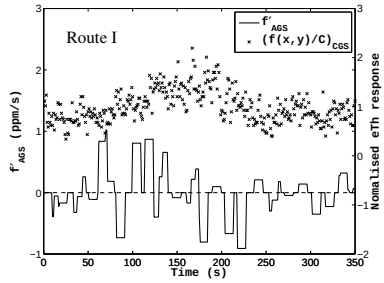

Figure 5: First derivative, f'_{AGS}, (solid line) derived from AGS data along route I after smoothing using $N = 10$, cf. Eq. (3). The normalised CGS eTh counts (dots, right axis) are included for comparison.

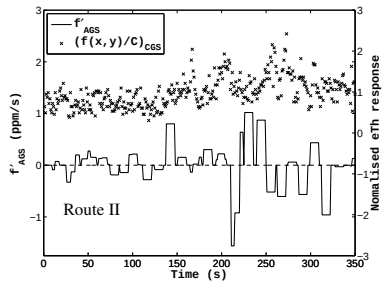

Figure 6: First derivative, f'_{AGS}, (solid line, left axis) derived from AGS data along route II after smoothing using $N = 10$, cf. Eq. (3). The normalised CGS eTh counts (dots, right axis) are included for comparison.

the eTh background estimation. For other areas, depending on the background composition, the methodology used here may instead be used for K or eU estimation.

4. Results and Discussion

4.1. Ground to air comparisons

The normalised ground level eTh response along with the normalised AGS response for route I are shown as a function of CGS time in Fig. 4. The responses of the two data sets are similar (mean $\kappa = 1.002$) within the high-activity area (around $t = 170$ s), with both the positive and the negative gradients accounted for. Some discrepancies exist however, especially in the low-activity areas with no obvious activity gradients. Fig. 4 shows that the AGS data could be used on the ground for the most challenging background area even when confined to roads (CGS).

4.2. Accounting for the systematic component

Figure 5 shows the results of Eq. (2) applied to the AGS data set along route I after smoothing the data using a moving average of length 10, cf. Eq. (3). At first, f'_{AGS} appears noisy as it fluctuates around zero. But when comparing with the normalised CGS response for the same route, which is also given in Fig. 5, some important features become apparent. There are two groups: one with a number of positive derivates around $t = 100$ s and the other with a number of negative derivatives around $t = 200$ s. These two groups hold the information required to account for the strong gradients in connection to the high-activity area around $t = 170$ s.

Figure 6 shows f'_{AGS} along route II. From Figs. 5-6 it is clear that f'_{AGS} does not precisely follow the variation of the CGS data. The steps based on the AGS data appear a bit off in time. Despite the discrepancies, the AGS data still offers a rough prediction both on the magnitudes and, more importantly, on the sign of the expected changes in eTh data.

4.3. Reducing false alarms

From Fig. 7 it is clear that MA^w increases the mean in the positive gradient (~50-170 s) along route I and decreases the mean in the negative gradient (~200-250 s) along the same route. The same reasoning applies to route II as well, as shown in Fig. 8. The modifications on MA may at a first look modest, but when using the unmodified moving average, MA_{40}, more samples than

False Positives (α = 5 %)				
	Route I (N = 312)		Route II (N = 312)	
	NaI(Tl)	$LaBr_3$:Ce	NaI(Tl)	$LaBr_3$:Ce
MA_{40}	6.4 (n = 20)	8.3 (n = 26)	7.1 (n = 22)	7.7 (n = 24)
MA^{γ}_{40}	5.8 (n = 18)	6.4 (n = 20)	5.8 (n = 18)	6.7 (n = 21)
MA^{w}_{40}	6.4 (n = 20)	5.8 (n = 18)	6.1 (n = 19)	5.5 (n = 17)
$MA^{w,\gamma}_{40}$	5.1 (n = 16)	4.5 (n = 14)	4.5 (n = 14)	4.2 (n = 13)

Table 1: Number of false positives, n, given in % along routes I and II for both detectors and using a number of different MA statistics. The expected number of false positives for a prediction interval of 5 % with N = 312 is 15.6.

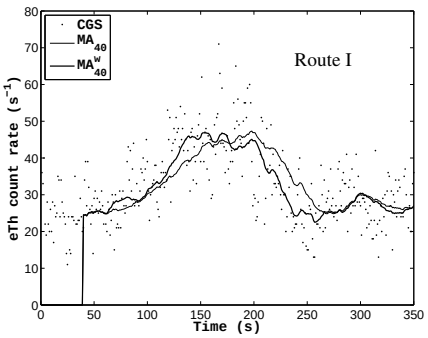

Figure 7: Weighted Moving Average, MA^{w}_{40} (solid, thick line), unmodified moving average, MA_{40} (solid, thin line), and CGS eTh counts (dots), for route I. The use of weights increases the mean in the positive gradient ($60 \leq t \leq 160$ s) and decreases the mean in the negative gradient ($170 \leq t \leq 260$ s).

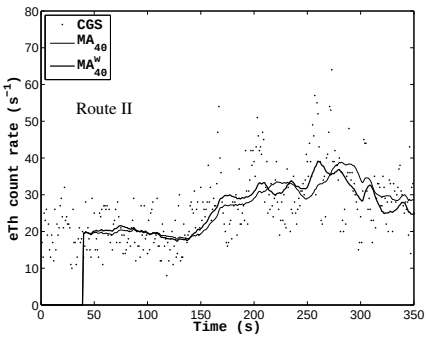

Figure 8: Weighted Moving Average, MA^{w}_{40} (solid, thick line), unmodified moving average, MA_{40} (solid, thin line) and CGS eTh counts (dots), for route II. The use of weights increases the mean in two of the positive gradients ($140 \leq t \leq 210$ and $240 \leq t \leq 270$ s) and decreases the mean in two of the negative gradients ($210 \leq t \leq 230$ and $270 \leq t \leq 350$ s).

expected fall outside the upper prediction interval endpoint, cf. Table 1. This result exemplifies the problem of accurate background estimation while driving in strong positive background gradients.

As can be seen in Table 1, the use of weights in the moving average generally improves the false positive rates. That is, the adjustments of the mean result in false positive rates closer to the expected rates, given by the normal distribution. The shift from a non-normal to a more normal-like distribution can also be seen by studying Fig. 9, where a perfect normal fit would be a straight line.

Since the 7.62 × 7.62 cm^2 $LaBr_3$:Ce detector has low efficiency in comparison to the 8 L NaI(Tl) used throughout this study, Fig. 10 gives MA^{w}_{40} applied to the total count rate instead of eTh primary counts. When comparing the $LaBr_3$:Ce response for route II, shown in Fig. 10, to the NaI(Tl) response for the same route, given in Fig. 8, the results are similar. This result confirms the assumption of this study: that the total gamma background variation within the studied area is well described by the variation of thorium alone. It also shows that MA^{w} can be applied to the total count rate instead of a specific nuclide window. However, to apply weighting to total counts might not be as accurate as using nuclide specific counts.

Although no tests of the power or false negative rates were conducted in the present study, visual inspection of

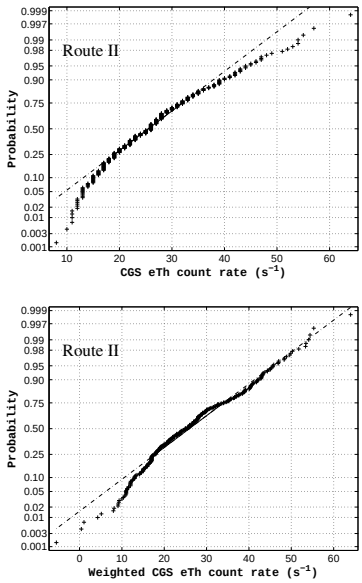

Figure 9: Normal probability plot of raw eTh data (top) and weighted eTh data (bottom) for the CGS 8 L NaI(Tl) system along route II. The raw distribution is skewed, indicating an excess of samples with high count rates and too few samples with low count rate. After applying weights the distribution becomes more normal-like in the upper tail.

Figs. 7-8 reveals that the mean of MA^w_{40} is consistently lower than that of MA_{40} in the negative gradients. The correction factor due to autocorrelation, $\sqrt{1/\gamma}$, was 1.06 using the ACF given in Eq. (7) and should not have a too strong negative impact on the power. Hence, the false negative rate of the weighted moving average should be lower than for the unweighted in negtive gradients.

If AGS data are available it should also be straightforward to extend the weighted moving average method to include other background components (e.g. eU, K or ^{137}Cs) as well. This could be done by introducing one or more additional terms in the weight function, Eq. (5).

5. Conclusions

AGS data can be used to estimate the variations at the ground level, even when the terrestrial survey is confined to roads (CGS). Normalised AGS data can be useful when accounting for strong gradients in the natural radiation background.

This study has shown that using AGS data to weight the moving average can reduce the number of false positives in positive background radiation gradients without introducing additional false negatives in the negative background radiation gradients.

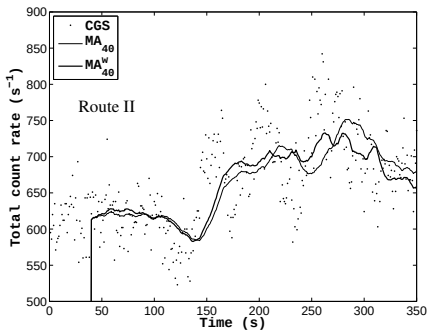

Figure 10: MA^w_{40} (thick, solid line) and MA_{40} (thin, solid line) for $LaBr_3$:Ce total count rate along route II.

Shifting the mean of the moving average by the use of weights derived from AGS data improved the accuracy of the average, while reducing the bias due to autocorrelation improved the precision of the sample standard deviation of the moving average. Combining the two gave the best overall result.

Acknowledgements

The authors wish to thank the Geological Survey of Sweden for sharing their survey data. This work was supported by the Swedish Radiation Safety Authority.

References

[1] H. Aage, U. Korsbech, Search for lost or orphan radioactive sources based on NaI gamma spectrometry, Appl. Radiat. Isotopes 58 (1) (2003) 103–113.

[2] A. Cresswell, D. Sanderson, The use of difference spectra with a filtered rolling average background in mobile gamma spectrometry measurements, Nucl. Instrum. Meth. A 607 (3) (2009) 685–694.

[3] P. Kock, R. Finck, J. Nilsson, K. Östlund, C. Samuelsson, A deviation display method for visualising data in mobile gamma-ray spectrometry, Appl. Radiat. Isotopes 68 (9) (2010) 1832–1838.

[4] IAEA, IAEA-TECDOC-566, The use of gamma ray data to define the natural environment, International Atomic Energy Agency (IAEA), Vienna, Austria (1990).

[5] P. Kock, C. Samuelsson, Comparison of airborne and terrestrial gamma spectrometry measurements-evaluation of three areas in southern Sweden, J. Environ. Radioactiv. 102 (6) (2011) 605–613.

[6] L. Currie, Limits from qualitative detection and quantitative determination, Anal. Chem. 40 (3) (1968) 586–593.
[7] T. Hjerpe, R. Finck, C. Samuelsson, Statistical data evaluation in mobile gamma spectrometry: An optimization of on-line search strategies in the scenario of lost point sources, Health Phys. 80 (6) (2001) 563–570.
[8] D. Strom, J. MacLellan, Evaluation of eight decision rules for low-level radioactivity counting, Health Phys. 81 (1) (2001) 27–34.
[9] T. Hjerpe, C. Samuelsson, A comparison between gross and net count methods when searching for orphan radioactive sources, Health Phys. 84 (2) (2003) 203–211.
[10] L. Méray, Deconvolution of nuclear spectra of low counts, Nucl. Instrum. Meth. A 353 (1-3) (1994) 272–275.
[11] P. Kock, J. Lanke, C. Samuelsson, A real-time statistical alarm method for mobile gamma spectrometry–combining counts of pulses with spectral distribution of pulses, Nucl. Instrum. Meth. A 681 (2012) 55–60.
[12] L. Ramirez, L. Wielopolski, Analysis of potassium spectra with low counting statistics using trapezoidal and library least-squares methods, Appl. Radiat. Isotopes 61 (6) (2004) 1367–1373.
[13] G. Gilmore, Practical gamma-ray spectrometry, 2nd Edition, Wiley-VCH Verlag, Weinheim, 2008.
[14] IAEA, IAEA Technical Report Series 323, Airborne gamma ray spectrometer surveying, International Atomic Energy Agency (IAEA), Vienna, Austria (1991).
[15] ICRU, Gamma-ray spectrometry in the environment, ICRU report 53, International Committee on Radiological Units and Measurements (ICRU), Bethesda, MD, USA (1994).
[16] D. Sanderson, J. Ferguson, The European capability for environmental airborne gamma ray spectrometry, Radiat. Prot. Dosim. 73 (1-4) (1997) 213–218.
[17] Y. Zhang, S. Xiong, T. Chen, Application of airborne gamma-ray spectrometry to geoscience in China, Appl. Radiat. Isotopes 49 (1-2) (1998) 139–146.
[18] R. Grasty, Environmental monitoring by airborne gamma ray spectrometry, experience at the Geological Survey of Canada, in: IAEA-TECDOC-827, Vienna, Austria, 1995, pp. 93–101.
[19] Q. Bristow, Airborne γ-ray spectrometry in uranium exploration. principles and current practice, Int. J. Appl. Radiat. Isot. 34 (1) (1983) 199–229.
[20] P. Martin, S. Timis, A. McGill, B. Ryan, K. Pfitzner, Use of airborne γ-ray spectrometry for environmental assessment of the rehabilitated Nabarlek uranium mine, Australia, Environ. Monit. Assess. 116 (2006) 531–553.
[21] H. Toivonen, Airborne gamma spectrometry - Towards integration of European operational capability, Rad. Prot. Dosim. 109 (1-2, SI) (2004) 137–140.
[22] B. Minty, Fundamentals of airborne gamma-ray spectrometry, AGSO J. Aust. Geol. Geophys. 17 (2) (1997) 39–50.
[23] D. Sanderson, A. Cresswell, D. White, The effect of flight line spacing on radioactivity inventory and spatial feature characteristics of airborne gamma-ray spectrometry data, Int. J. Remote Sens. 29 (1) (2008) 31–46.
[24] R. Shumway, D. Stoffer, Time series analysis and its applications with R examples, Springer, New York, 2011.
[25] R. E. Walpole, R. H. Myers, S. L. Myers, K. Ye, Probability & statistics for engineers & scientists, 7th Edition, Prentice Hall, Upper Saddle River, 2002.

Paper V

INVESTIGATING MICROPHONIC NOISE IN MOBILE GAMMA-SPECTROMETRIC HPGE MEASUREMENTS USING ACCELEROMETERS.

Kock, Peder[1]

[1] Medical Radiation Physics, Lund University, Sweden

Abstract

Microphonic noise caused by vibrations can be a problem in mobile gamma-spectrometric measurements using HPGe detectors. When driving on uneven roads moderate speeds might give raise to a considerable amount of vibrational stress. The resulting distorted spectra can be difficult to interpret, and potentially important spectral information may be lost. However, accelerometers can be used to detect and quantify the vibrations. These measurements can then be used to reduce the vibrational stress on the detector system.

To demonstrate the impact of noise from detector microphonics, vibrational data was gathered along with spectral measurements from an experiment with a car-borne mobile platform. The acquired accelerometer data could then be connected to the spectrum where distortions were observed. Speed and position on the road was also recorded and stored in the same record. This technique makes it possible to evaluate and compare different detector mounting configurations.

As this article shows, a sane mounting configuration will reduce the microphonic noise. This could be crucial for example in an orphan source emergency situation, where measurements must be gathered with speed and accuracy. Using accelerometers can be one way of achieving a reliable car-borne HPGe system by reducing the interference from microphonic noise.

Introduction

Vibrations causing small movements of the components in a Germanium detector's mounting can alter the capacitance between the field effect transistor (FET) gate and the detector bias supply. This may change the noise characteristics of the detector and in turn give raise to an electrical signal. Even a small change (10^{-7} pF) in the capacitance can cause an electrical signal equivalent of a few keV (Gilmore 2008). This mechanically generated noise is referred to as microphonic noise. Its main sources during normal operation conditions are environmental acoustic noise, vibrations of the surrounding equipment and events connected to liquid nitrogen such as turbulence and bubbling in the dewar affecting the cryostat (Morales et. al 1992).

Although this should be a common problem in mobile gamma spectrometry using HPGe detectors, where, by necessity, some vibrations occur, most of the literature found on the topic of microphonic noise deals with low background experiments (Baudis et al. 1998; Morales et al. 1992) or electrically cooled semiconductor systems (Upp et al. 2005). Ways of discriminating microphonic pulses include digital signal processing (Keyser et al. 2008) and statistical rejection techniques (Morales et al. 1992).

Possible explanations for the lack of applied studies are;

- NaI(Tl) detector systems are more frequently used in mobile gamma spectrometry
- The microphonic noise mainly affects low energy region (<100 keV)
- The ambient background is not controlled, hence disturbances might be overlooked

This article shows the importance of a vibration dampening mounting configuration when using a HPGe detector in mobile measurements and how accelerometers can be used to optimize the same configuration. Digital signal processing and statistical rejection techniques are out of the scope of this work since they do not deal with the source of the problem, but rather its consequences.

Material and methods

Spectrometry system

In the experiments a ruggedized, coaxial, P-type High-Purity Germanium (HPGe) detector[1], model no. GEM 100-S, with 123 % relative efficiency from Ortec[2] was mounted in a GMC van at a height of approximately 1 m above ground. The detectors cylinder axis was horizontally orientated with the end-cap facing the rear of the van. A digital, portable, Multi-Channel Analyser (MCA, Ortec Digidart), with the conversion gain set to 2048 channels was used. The MCA communicated with a laptop-PC over the USB (Universal Serial Bus) interface, sending a new pulse height distribution when requested. Measurements in the region below 40 keV using a P-type HPGe detector is normally pointless due to the thick dead-layer. But these noise pulses could potentially have effect on critical things higher up in the spectra, leading to peak-broadening.

A linear 3-axis accelerometer from ST Microelectronics (LIS3LV02DL) was mounted on the detectors aluminium cap to measure vibrations. The sensors can measure accelerations up to ± 6 g in three orthogonal directions, with a specified resolution of about 4 mg at 610 Hz. Acceleration directions are henceforth referred to as X, Y and Z, where -X is an acceleration in the driving direction, +Y to the van's right when driving and +Z down towards the ground.

To scrutinize the influence of the detector mounting configuration, two different sets of dampeners were used. Fist the ‘bare-bone’ configuration, where the detector was mounted directly on the floor of the car. Second the ‘dampener’ configuration, where

1 s/n p41629A

2 Ortec, 801 S. Illinois Ave., Oak Ridge, TN, USA.

the detector was mounted in a plastic tube, isolated with approximately 10 cm of polyester foam.

Experiment

By observing spectra while driving on an uneven road, conclusions about different mounting configurations and their effect on the microphonic noise level can be drawn. In this work, a straight stretch about 400 m long was driven repeatedly while sampling spectral and vibrational data. To estimate the radiation background, 22 stationary 60 s background spectra was first measured at ~ 20 m intervals along the road. The straight stretch was then driven at three different velocities; 10, 20 and 30 km h^{-1} to gradually increase the mechanical stress on the detector. Each speed was driven four times, giving a total of 12 measurement sets. Spectrometer, accelerometer and GPS data were collected at 1 Hz using in-house software written in C#. This procedure was repeated for both mounting configurations.

Statistical analysis

To separate the microphonic noise from the ambient radiation background a region of interest **R** was chosen, ranging from the cut-off energy at 10 keV to 100 keV. The distribution of the number of gross counts per second n_b within **R** will be approximately normal with mean m_0 and standard deviation $\sigma = \sqrt{m_0}$, if measured repeatedly. Thus an observation x, which is significantly greater than m_0, would be an indication that microphonic noise was detected in a spectrum.

Using the null hypothesis, H_0, "no microphonic noise detected" and the research hypothesis, H_1, "microphonic noise detected" the test statistic

$$u = \frac{\bar{x} - m_0}{D} \qquad (1)$$

, where $D = \frac{\sigma}{\sqrt{n}}$ was calculated for each set $x_1, x_2, \ldots, x_n$ of measured spectra. Under H_0, u will be observations from N(0,1). The null hypothesis can thus be rejected on the 1-α level if $u \geq \lambda_\alpha$. The single sided critical regions for u are presented in Table 1.

Table 1. Significance levels for the test statistic *u*.

Significance	*	**	***
α	0.05	0.01	0.001
u	1.64	2.33	3.09

The sample size of the test group, n, was chosen to be 3 spectra to avoid the worst fluctuations and the level of significance, α, was set to 0.001. The limit for rejection of H_0, then becomes

$$u_l = \sqrt{3}\frac{\bar{x} - m_0}{\sigma} \geq 3.09 \qquad (2)$$

Results and Discussion

Figs. 1-2 show the results from the hypothesis tests using the 'bare-bone' and 'dampener' configurations. The results summarized in Table 2 show that the number of rejected samples increases with increasing driving speed, which was expected. At the slowest speed (10 km h^{-1}), the statistical tests showed no evidence of microphonic noise being detected. By increasing the driving speed to 20 km h^{-1} about 19 % of the measurements showed a significant number of microphonic noise pulses in the low energy region, **R**, when using the 'bare-bone' configuration. The number of rejected samples increased to 79 % when driving at the fastest speed (30 km h^{-1}) using the same configuration. By mounting the detector in the 'dampener' configuration, these numbers sank drastically. The rejection fraction, also shown in Table 2, was 2 and 19 % for 20 and 30 km h^{-1} respectively. To summarize, the total rejection fraction, i.e. the total fraction of measurements showing an significant increase of the count rate in **R** due to microphonic noise were 20 and 4 % for the 'bare-bone' and 'dampener' configurations respectively.

Table 2. Summary of hypothesis tests.

Test group	Samples	Rejection of H_0	Rejection of H_0 (%)
bare-bone u_{10}	391	1	0.2
bare-bone u_{20}	213	40	18.8
bare-bone u_{30}	138	109	79.0
dampener u_{10}	392	0	0.0
dampener u_{20}	219	4	1.8
dampener u_{30}	146	28	19.2
bare-bone total	742	150	20.2
dampener total	757	32	4.2

Two samples with extreme test statistic values from each mounting configuration, thus containing significant levels of microphonic noise were analysed in detail. The samples, labelled A, B, C and D are marked in Figs. 1-2. Acceleration data for these four samples are presented in Figs. 3-4 and spectra in Figs. 6-7.

The accelerometer data in Figs. 3-4 reveals both vibrations and more shock-like events. The detector is subject to forces mainly in the Z (up, down) and Y (left, right) directions, while the data show more moderate vibrations along the detector's cylinder axis (X). An offset of about 1 g is present in the Z-direction due to gravity. The frequency of the vibrations seems to be generally higher in the samples A and B (bare-bone) than in C and D (dampener) while the amplitudes show a reversed relationship. This clearly demonstrates the complexity of the microphonic noise problem. By introducing a dampening material much of the microphonic noise disappears. As shown in Table 2, but some measurements with large (several g's), shock-like, accelerations still appear because of the uneven road and high velocities.

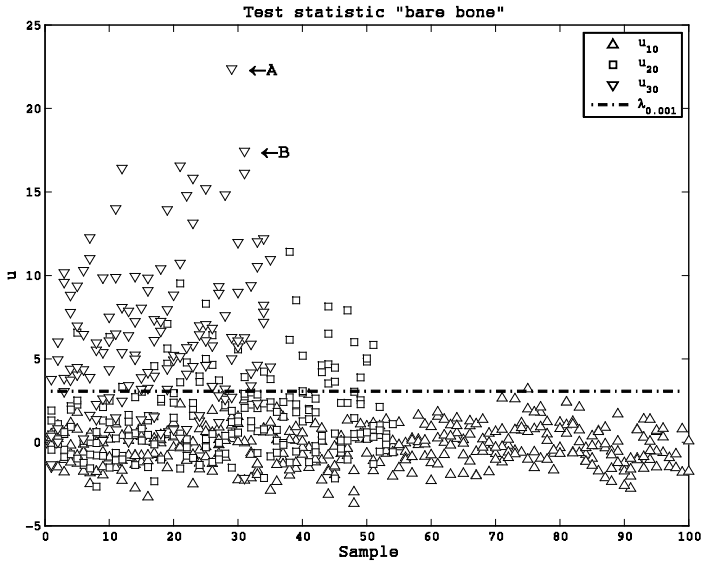

Fig. 1. Test statistic *u* for the 'bare-bone' configuration. The limit for rejection of H_0, λ_α, is marked with a dash-dotted line.

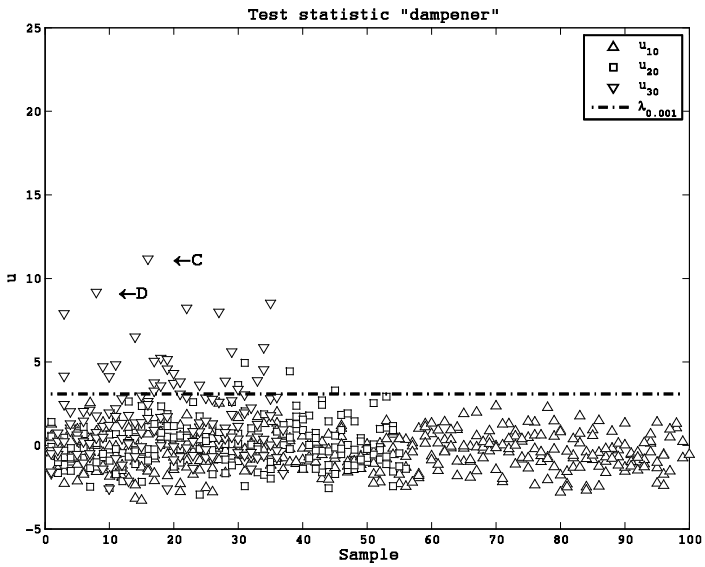

Fig. 2. Test statistic *u* for the 'dampener' configuration. The limit for rejection of H_0, λ_α, is marked with a dash-dotted line.

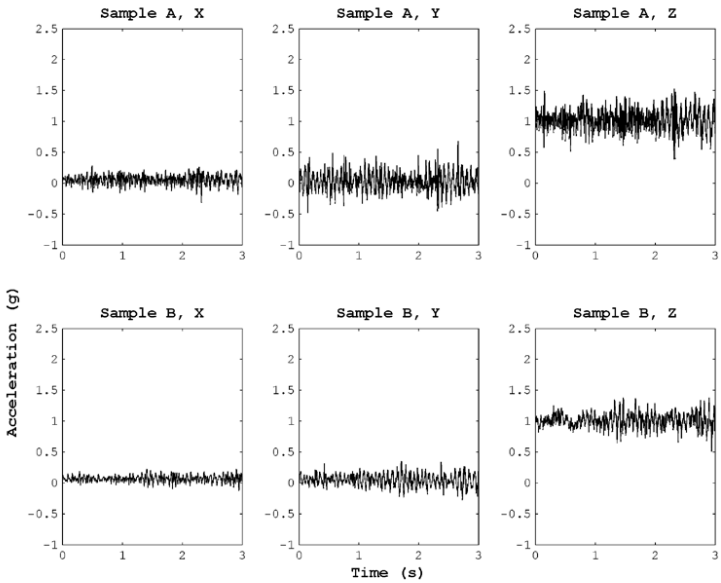

Fig. 3. Accelerometer data for 'bare-bone', samples A and B. No shock-like events are present, rather a steady ripple, especially in the Y and Z-directions.

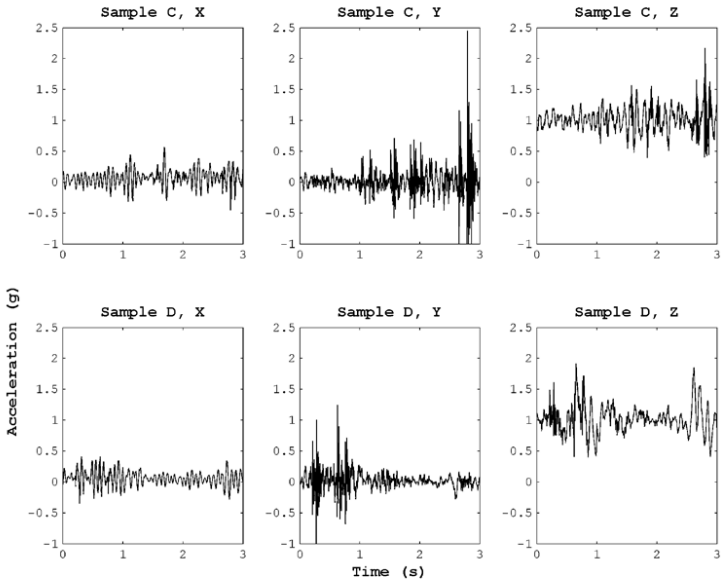

Fig. 4. Accelerometer data for 'dampener', samples C and D. Some shock-like events can be observed in the Y and Z-directions.

That a frequency shift occurs when introducing the dampener is confirmed in Fig. 5, where the single-sided Fast Fourier Transform (FFT) of all Z-direction acceleration measurements at 30 km h^{-1} is presented. All measurements for each of the two configurations were summed to show the different vibration characteristics. While frequencies in the range 10-50 Hz dominated in the 'bare-bone' measurements, the 'dampener' shows a peak below 25 Hz. When introducing the 'dampener' the total mass of the vibrating body also increases. This could be one factor that leads to a shift of vibration frequencies. The most obvious reason is of course the introduction of a soft dampening material - the polyester foam between the van's floor and the detector.

Spectral data for the four samples A-D are presented in Figs. 6-7. The microphonic noise mainly adds pulses in the low energy region below 20-30 keV. As much as 80 extra pulses per second due to microphonic noise were recorded (sample A). The 'bare-bone' samples A and B show more microphonic pulses than the 'dampener' (C and D), which also can be seen in the test-statistic, *u*, when comparing Figs. 1 and 2.

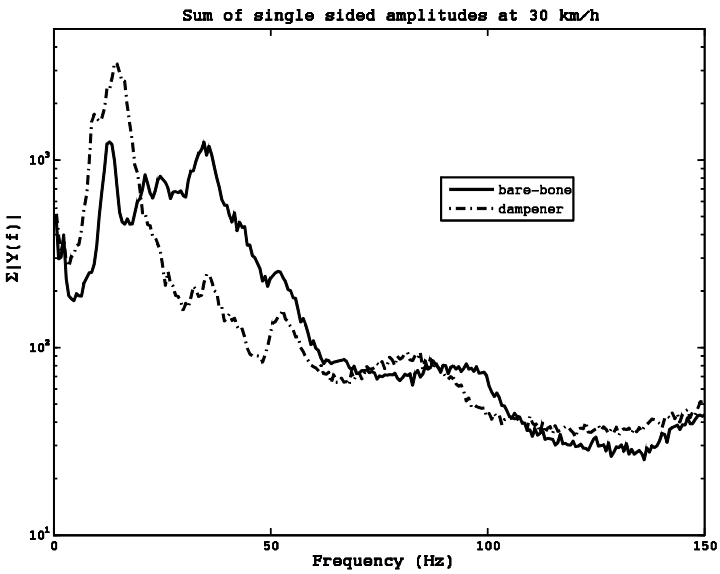

Fig. 5. Summed Single sided Fast Fourier Transform plot for all Z-direction acceleration measurements recorded at 30 km/h. A frequency shift occur when changing from the 'bare-bone' to the 'dampener' configuration.

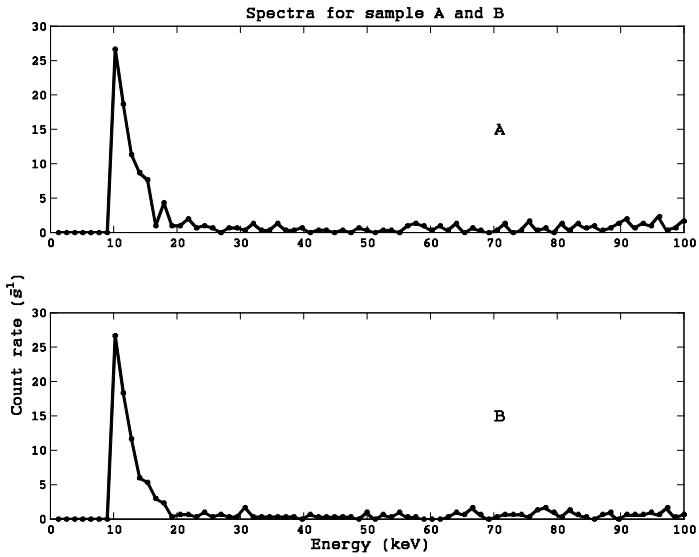

Fig. 6. Spectra for 'bare-bone' samples A and B. The main contribution in the low enery region (below 30 keV) is from microphonic noise.

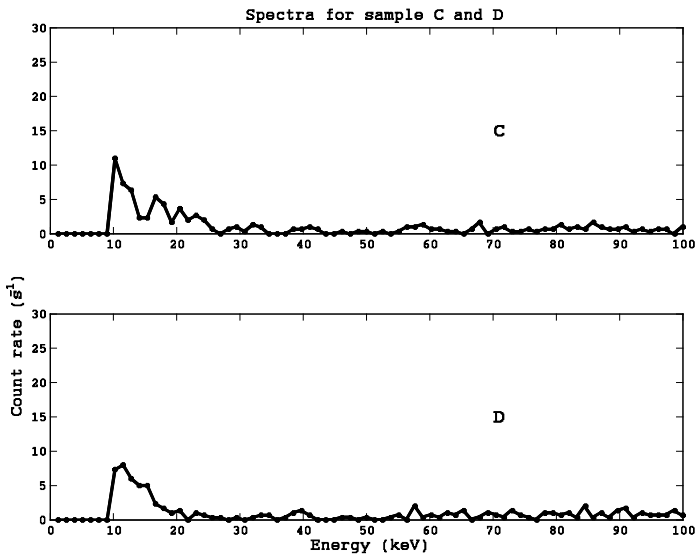

Fig. 7. Spectra for 'dampener' samples C and D. The main contribution in the low enery region (below 30 keV) is from microphonic noise.

Conclusions

As shown in this work microphonic noise occur when driving on uneven roads in moderate speeds. The microphonic noise increases as the speed of the vehicle, and hence the vibrations, increase. However, a few simple measures can reduce the microphonic noise considerably when using a car-borne HPGe detector system. A polyester foam dampener led to a reduction of the microphonic samples from 20 to 4 % of the total number of samples. Using a 3-axes accelerometer this work shows that the reduction was mainly due to a frequency shift in the vibrational forces acting upon the detector.

The results presented in this paper are hard to generalize, since they depend on a specific detector model, possibly even on an individual detector. However, it should be possible to conduct a more general experiment in a controlled laboratory environment using induced vibrations.

Acknowledgements

This work was supported by the Swedish Radiation Protection Agency (SSM). I thank Karl Östlund for his help with the construction of the dampener.

References

Baudis, L., Hellmig, J., Klapdor-Kleingrothaus, H.V., Ramachers, Y., Hammer, J.W., Mayer, A. High-purity germanium detector ionizing pulse shapes of nuclear recoils, γ-interactions and microphonism. Nuclear Instruments and Methods in Physics Research A 1998; 418: 348-354.

Gilmore, G. Practical Gamma-Ray Spectrometry, 2nd Edition. Weinheim:Wiley-VCH Verlag; 2008.

Keyser, R.M., Bingham, R.D., Twomey, T.R. Improved performance in germanium detector gamma-spectrometers based on signal processing. Journal of Radioanalytical and Nuclear Chemistry 2008; 276 (3): 567-575.

Morales, J., Garcia, E., Ortiz de Solorzano, A., Morales, A., Nuñes-Lagos, R., Puimedon, J., Saenz, C., Villar, J.A. Filtering microphonics in dark matter germanium experiments. Nuclear Instruments and Methods in Physics Research A 1992; 321: 410-414.

Upp, D.L., Keyser, R.M., Twoney, T.R. New cooling methods for HPGE detectors and associated electronics. Journal of Radioanalytical and Nuclear Chemistry 2005; 264 (1): 121-126.

LUND
UNIVERSITY

ISBN 978-91-7473-385-3